



Master Thesis

Design by Optimization of a Multi-Element Airfoil for Drag Power Kite

Christoph Drexler
WE-MT-04-10

Author:	Christoph Drexler
Registration number:	03626726
Professor:	Carlo L. Bottasso
Supervisors:	Filippo Campagnolo Florian Bauer (EI - EAL)

Garching bei München, January 2019

STATEMENT OF AUTHORSHIP

I, Christoph Drexler, confirm that the work presented in this thesis has been performed and interpreted solely by myself except where explicitly identified to the contrary. All verbatim extracts have been distinguished by quotation marks, and all sources of information have been specifically acknowledged. I confirm that this work has not been submitted elsewhere in any other form for the fulfillment of any other degree or qualification.

Garching bei München, January 2019

ABSTRACT

To mitigate climate change, more efficient and widespread renewable energy technologies are necessary. Kite power systems are able to provide cheaper and more reliant energy than conventional wind turbines. This work is part of a project at the Technical University of Munich which focus is the development of a high-lift drag-power kite system with biplane structure and multi-element airfoils. A Matlab routine for (multi-element) airfoil optimization incorporating MSES was developed and a posterior CFD analysis was used to verify the results. The Covariance Matrix Adaptation Evolution Strategy was used to generate and evaluate parameter combinations describing geometries of single- and double-element airfoils which were parameterized using splines. Two base airfoils were optimized at four operating points ($Re \in [1.6, 5.7] \cdot 10^5$, $Ma \in [0.04, 0.15]$) with an increasing number of degrees of freedom, using found optima from previous steps as initial configuration for the next optimization. The drag coefficient was minimized for each of the four single- and two double-element configurations above a previously determined minimum threshold for the lift coefficient. The aerodynamic coefficients were verified with ANSYS CFX and XFOIL (single-element airfoils). An increase in geometric degrees of freedom correlated with increased aerodynamic performance in terms of lift. The incorporation of MSES convergence indicators into the cost function led to improved convergence behavior during the optimization. Convergence was achieved much more easily for single- than for multi-element airfoils. However, the values of the lift and drag coefficients from MSES differed significantly from those from ANSYS CFX. The CFD simulations showed that flow separation was present at most airfoils. Turbulence effects in form of vortices which originated from the symmetry boundary planes of the simulated domain in ANSYS CFX could possibly be the cause for these discrepancies.

Keywords: Airborne wind energy, drag power kites, high lift, low Reynolds, low Mach, airfoil optimization, multi-point optimization, evolutionary algorithm, CMA-ES, multi-element airfoils, aerodynamics, ANSYS CFX.

ACRONYMS AND ABBREVIATIONS

Abbreviation	Meaning
AC	alternating current
AOA	angle of attack, α
BL	boundary layer
cf.	confer—compare to
CF	capacity factor
CFD	Computational Fluid Dynamics
CFRP	Carbon Fiber Reinforced Plastic
CMA-ES	Covariance Matrix Adaptation Evolution Strategy
DOF	Degree(s) of freedom
et al.	and others
etc.	et cetera—and similar things
e.g.	exempli grata—for example
i.e.	id est—that is to say
LCOE	Levelized Cost Of Electricity
LE	leading edge
n.d.	not defined
MIT	Massachusetts Institute of Technology
OP	Operation point
ol	outer layer
PC	Personal Computer
PT	Parameterization type
TE	trailing edge
TUM	Technical University of Munich
vsl	viscous sublayer
w.r.t.	with respect to

SYMBOLS

Symbol	Meaning
<i>General nomenclature, operators</i>	
∇	Gradient
x, y	Placeholder variable
\mathbf{x}	Bold math face; Vector notation
Δ	Delta operator
$x \cdot y$	Dot product
$\frac{d}{dt}$	Derivative w.r.t. x
$\frac{\partial}{\partial x}$	Partial derivative w.r.t. x
\dot{x}	Partial derivative of x w.r.t. the time
\hat{x}	Maximum value of x
\tilde{x}	Variable variation
\int_x	Integral over x
P	Point
i	Counting variable
$\sum_{i=1}^N$	Sum over i from 1 to N
<i>Latin symbols</i>	
A	Area [m ²]
\mathbf{a}	Expectation, mean
a	Glide angle, distance to trailing edge
\mathbf{B}	Parameter covariance matrix
b	Buffer value
C	Aerodynamic coefficient, e.g. C_L —lift coefficient
c	camber
CH_4	Methane
CO_2	Carbon dioxide
E	Aerodynamic efficiency
e	Mass-specific energy [J/kg]
F	Force [N]
f	Function
g, \mathbf{g}	Gravity [m/s ²]
h	Height [m]
l	length
k	Turbulence kinetic energy
Ma	Mach Number
N	Number, amount
\mathbf{n}	Normal vector of surface
N_2O	Nitrous oxide
P	Power [W]
p	Pressure [kPa], parameter value (if with index)
Re	Reynolds Number
S	Stagnation point

Symbol	Meaning
T	Temperature [$^{\circ}\text{C}$]
t	thickness [m]
v, \mathbf{v}	Velocity [m/s]
W	Work [J]
X	Group of points describing the desired airfoil shape, for which fitting parameters have to be found
x, y, z	Cartesian coordinates
y^+	Dimensionless wall distance
<i>Greek symbols</i>	
α	Angle of Attack, AOA
Γ	Surface
δ	Boundary layer thickness [m]
ζ	Scaling factor
κ	Curvature [m^{-1}]
μ	Viscosity [Pa s]
ν	Kinematic viscosity [Ns/m^2]
φ	Angle between chord lines of two adjacent airfoil elements
ϕ	Relative humidity
Ψ	Points described by the airfoil parameters
ψ	Individual point in Psi
ρ	Density [kg/m^3]
σ	Standard deviation
τ	Shear stress [Pa]
θ	Angle between two profile lines
χ	Individual point in X
Ω	Volume
ω	Turbulence frequency
<i>Super-/subscripts</i>	
$x^{(2)}$	Iteration; here 2
a	apparent
best	best
b	bottom
c	chord, crosswind
conv	Converged
cost	Cost
crit	Critical
D	Drag
d	Twisting distance
eval	Evaluations
in	Intersection
inner	Within the same element
inter	Between different elements
k	Kite
L	Lift
LE	Leading edge
max	Maximum
min	Minimum
n	nominal
Newton	W.r.t. Newton iterations
opt	Optimum

Symbol	Meaning
P	Pressure
param	Parameter
R	Cost region, e.g. R1 for cost region 1
ref.	reference
rel.	relative
rot.	rotatory
S	Symmetry
surf	Surface
st	Sharp turn
stag	Stagnation
stat	Static
T	Tether
t	top
threshold	Threshold
tp	Thin profile
TE	Trailing edge
vol	Volume
w	Wind, wall
∞	Ambient

LIST OF FIGURES

1.1	Effect of greenhouse gas emissions the atmosphere of the earth.	1
1.2	Overview of steps of the presented thesis.	3
2.1	Drag-power kite scheme.	5
2.2	Velocities and forces acting on a drag-power kite.	7
2.3	Basic airfoil nomenclature.	8
2.4	Boundary layer development.	11
2.5	Airfoil stall: Velocity gradients and streamlines.	12
2.6	Covariance Matrix Adaptation Evolution Strategy.	16
4.1	Parameterization types and anchor points for spline interpolation.	22
4.2	Apparent airspeeds of the operating points.	23
4.3	Structure of the optimization strategy.	24
4.4	Computational framework in Matlab.	27
4.5	Cost value mapping in region 2.	30
5.1	Cost development of the viscosity sensitivity analysis.	35
5.2	Airfoil shapes and cost-to-AOA relation of the viscosity sensitivity analysis. . . .	36
5.3	Sub-regions of cost region 2 of the maximum newton iterations sensitivity analysis.	37
5.4	Cost development of the maximum Newton iterations sensitivity analysis.	38
6.1	Optimized lift coefficients of the evaluation runs for the single- and double element configurations.	40
6.2	Development of airfoil shape, lift coefficients and cost for the determination run for PT ₄ of base geometry 1223.	41
6.3	Cost development for the double-element configuration of the 15th base geometry, PT ₁ and PT ₂	41
6.4	Jagged shape of polars for single-element configuration 15th, PT ₁	43
6.5	Jagged shape of polars remains after increasing the element side-points to 500 for single-element configuration 15th, PT ₁	43
6.6	Slope of the lift coefficient for the double-element airfoil 15th, PT ₁ . The optimum result from the evaluation run is located just left of the maximum of the lift coefficient slope. The shift of the optimum towards lower values of α is due to the reduction of the lift-induced drag by lowering the airfoil pitch.	44
6.7	Cost region share comparison of all runs.	45
7.1	Dimensions of the simulated domain in ANSYS CFX.	48
7.2	Node displacement error in ICEM CFD.	49
7.3	Single-element, 15th: Comparison of lift and drag coefficients from MSES/MSIS, ANSYS, XFOIL.	50
7.4	Single-element, 1223: Comparison of lift and drag coefficients from MSES/MSIS, ANSYS, XFOIL.	51
7.5	Double-element: Comparison of lift and drag coefficients from MSES/MSIS, ANSYS, XFOIL.	51

7.6	Streamlines of single-element configuration 15th, PT_4 at OP_3	52
A.1	Gantt chart of the initially planned schedule for the master's thesis (part 1/2).	55
A.1	Gantt chart of the planned schedule for the master's thesis (part 2/2).	56
B.1	15th base geometry, PT_1 . Normalized coordinates.	57
B.2	1223 base geometry, PT_1 . Normalized coordinates.	57
B.3	Polar for 15th base geometry, PT_1	59
B.4	Polar for 1223 base geometry, PT_1	60
C.1	Polar for 15th base geometry, PT_1	62
C.2	Polar for 15th base geometry, PT_2	63
C.3	Polar for 15th base geometry, PT_3	64
C.4	Polar for 15th base geometry, PT_4	65
C.5	Polar for 1223 base geometry, PT_1	67
C.6	Polar for 1223 base geometry, PT_2	68
C.7	Polar for 1223 base geometry, PT_3	69
C.8	Polar for 1223 base geometry, PT_4	70
C.9	Polar for 15th base geometry, PT_1 , double-element.	72
C.10	Polar for 15th base geometry, PT_2 , double-element.	73
C.11	Polar for 1223 base geometry, PT_1 , double-element.	75
C.12	Polar for 1223 base geometry, PT_2 , double-element.	76

LIST OF TABLES

1.1	System specifications of the personal computers (PCs) used in this work.	3
4.1	Types of airfoil parameterizations.	22
4.2	Values of the kinematic viscosity and Reynolds numbers of the operating points.	24
5.1	Reynolds numbers of the viscosity sensitivity analysis.	33
5.2	Cost region shares of the viscosity sensitivity analysis.	34
5.3	Cost region Shares of the maximum Newton iterations sensitivity analysis.	36
6.1	Threshold lift coefficients of all determination runs.	39
6.2	Number of runs for each cost function configuration in region 2.	46

CONTENTS

Acronyms and Abbreviations	v
Symbols	vii
List of Figures	xii
List of Tables	xiii
1 Introduction	1
1.1 Motivation	1
1.2 Procedure and Methodology	2
1.3 Work Plan and Necessary Resources	3
2 Fundamentals	5
2.1 Drag Power Kites	5
2.2 Power Generation	6
2.3 High Lift Airfoil Geometry	8
2.3.1 Airfoil Nomenclature	8
2.3.2 Take-Off and Landing Devices	8
2.3.3 Multi-Element Airfoils	9
2.4 Fluid Dynamics	9
2.4.1 Conservation Laws	9
2.4.2 Incompressibility Assumption	10
2.4.3 Inviscid Flow	10
2.4.4 Boundary Layer Theory	10
2.4.5 Flow around Airfoils	12
2.5 Optimization	15
2.5.1 Evolutionary Algorithms	15
2.5.2 Covariance Matrix Adaptation Evolution Strategy	15
3 Research and Technology	17
3.1 State of the Art	17
3.2 Previous Work	19
4 Airfoil Optimization	21
4.1 Airfoil Parameterization	21
4.2 Optimization Strategy	23
4.2.1 Operating Points	23
4.2.2 Base Airfoils	24
4.2.3 Structure	24
4.3 Computational Framework	26
4.4 Meshing and Flow Solution	28
4.5 Cost Function	28

4.5.1	Region 1: Solution Convergence	28
4.5.2	Region 2: Divergence	29
4.5.3	Region 3: Invalid Airfoil Geometry	30
4.5.4	Region 4: Boundary Violation	32
5	Prior Sensitivity Analyses	33
5.1	Viscosity	33
5.1.1	Setup	33
5.1.2	Analysis	33
5.2	Maximum Newton Iterations	36
5.2.1	Setup	36
5.2.2	Analysis	37
6	Optimization Strategy Evaluation	39
6.1	Development of Lift Coefficients	39
6.2	Pitch Robustness	42
6.2.1	Convergence	42
6.2.2	Repeatability	42
6.2.3	Curvature Shape	43
6.2.4	Positions of Optima	44
6.3	Cost Function Region Shares	44
7	Computational Fluid Dynamic Verification	47
7.1	Setup	47
7.1.1	Workflow	47
7.1.2	Turbulence Model	47
7.1.3	Mesh	48
7.2	Results	49
7.2.1	Convergence Criteria	49
7.2.2	Evaluation of Aerodynamic Coefficients	49
7.2.3	Flow Separation	52
8	Conclusion and Outlook	53
A	Work Plan	55
B	Base Airfoils	57
B.1	Base Geometries	57
B.2	Polars	59
C	Polar Data	61
C.1	Single-Element Airfoils	62
C.1.1	15th-Series	62
C.1.2	1223-Series	67
C.2	Double-Element Airfoils	72
C.2.1	15th-Series	72
C.2.2	1223-Series	75
D	Computational Fluid Dynamics Analysis	77
D.1	Mesh Characteristics Single-Element Airfoils	77
D.2	Mesh Characteristics Double-Element Airfoils	78
D.3	Simulation Results	79
D.3.1	15th-Series, Single-Element	79

D.3.2	1223-Series, Single-Element	80
D.3.3	15th-Series, Double-Element	81
D.3.4	1223-Series, Double-Element	81

Introduction

1.1 Motivation

With the advent of the industrial revolution around the year 1800 humans entered the *Anthropocene*. The term describes an era in which humans have become the dominant force on earth, shaping the environment and altering earth's climate [9]. The impact is so severe, that within 0.000 004 % of the planet's existence the average surface temperature rose by 0.9 °C and the globally averaged sea level increased by more than 0.2 m [10, p. 3].

It is assumed that the the increase in greenhouse gases in the atmosphere, such as CO₂, CH₄, and N₂O, are extremely likely the main cause of such effects [10, p. 3]. The correlation is shown in fig. 1.1. Policy makers around the world have agreed on climate protocols such as the *Paris Agreement* and proposed various laws and regulations to limit a further increase of these substances and help decelerate climate change [11, 12].

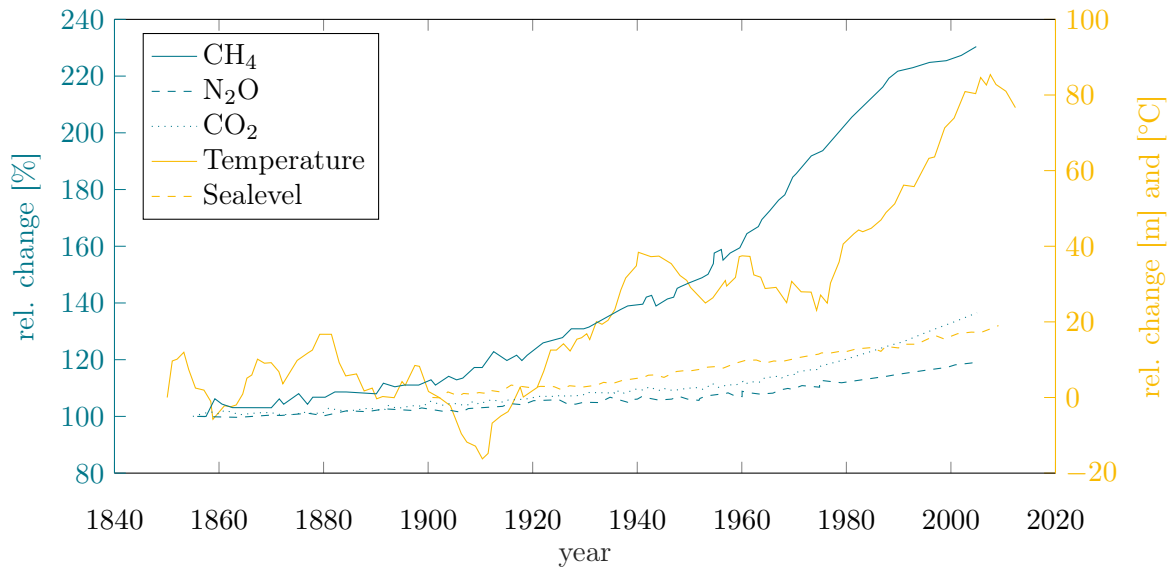


Figure 1.1: Correlation of greenhouse gas emissions to the increase in earth's globally averaged surface temperature and sea level. Relative changes w.r.t. values from 1850. Data adapted from [10, p. 3].

In Germany, the transformation of the energy sector into a completely emission-free industry has been a long goal as it is responsible for around 35 % of all CO₂ emissions [13]. New, more efficient technologies have paved the way to do so. Already about 36 % of the electricity used in Germany is provided by renewable energy systems [14]. The biggest share thereof—about 26 %—is contributed by wind energy systems [15].

The electrical energy produced by conventional wind turbines still has a carbon dioxide footprint of up to 68 g/kWh. Around 90 % of these emissions arise from the construction of the

plant and the materials used [16, 17]. Kite systems only require a fraction of these construction materials and can therefore further reduce the impact on the climate [1].

Compared to conventional systems, kite power plants have several more advantages. Because of higher operating heights they are able to reach regions with stronger and more reliable winds which results in generally higher capacity factors (CFs) and lower Levelised Costs of Electricity (LCOE) [18]. This is crucial to be competitive. Additionally, operating sites which are not suitable for conventional wind turbines are made accessible with this technology.

Motivated by these circumstances, multiple research institutes and companies around the world have engaged in the development of kite power technologies [19, p. xi]. This work is part of the research conducted at the *Chair of Electrical Drive Systems and Power Electronics* of the Technical University of Munich (TUM), which focuses on a high-lift drag power kite system [2, 20]. Compared to ground-based systems, one of the advantages of on-board power generation is that the electrical machines and propellers can also be used for take-off and landing procedures [19, p. 7]. Moreover, a higher theoretical power output can be generated [1, p. 107,108].

The presented work is based on the proven hypothesis that improved high lift capabilities lead to electricity at lower costs. The high-lift design is realized through two features: a biplane setup and a multi-element airfoil geometry [20]. The work presented in this paper focuses on (i) the setup of an optimization process and (ii) the design of advanced high-lift airfoils for the operating conditions of the drag power kite system.

Not only will the optimized single and multi-element airfoils contribute to an enhanced system performance. The developed optimization routine also represents the basis of a further extension to the multi-disciplinary system engineering model presented in [21]. By incorporating multiple detailed sub-models, a holistic design process is envisioned in which the design of each component of the drag power kite system is coupled w.r.t. various factors besides the parameters specific to each sub-problem.

1.2 Procedure and Methodology

The presented work is divided into two stages, depicted in fig. 1.2. A third stage was initially planned, but could not be completed due to an underestimated temporal demand of the first two steps and is only listed here for the sake of completeness¹.

The first stage is subdivided into multiple organizational and engineering steps. First, the work environment is established consisting of a tower PC and a laptop. The two machines are equipped with different software, both licensed and freeware. Next, the optimization strategy is defined along with a selection of two airfoil geometries which are then altered in the optimization process. Based on existing code, the strategy is then implemented within Matlab. The code comprises calls to MSES, an airfoil design and analysis software, which solves the flow equations and estimates the aerodynamic parameters which are to be improved.

In the second stage, a Computational Fluid Dynamic (CFD) workflow is established using ANSYS ICEM CFD and ANSYS CFX. This is done based on insight gained from preceding investigations [8, 20]. On the basis of existing Matlab code, replay files for ANSYS ICEM CFD, and journaling as well as post-processing state files for ANSYS CFX, a posterior analysis of the optimized designs from the first step is performed. The setup provided a semi-automated workflow for the assessment of (multi-element) airfoils.

The third stage was intended to provide experimental validation of the previously numerically estimated aerodynamic parameters. Such a validation is an industry standard (see sec. 3.1). Before application, airfoil designs have to be reviewed to evade unexpected numerical inaccuracies. During the course of this thesis it had to be acknowledged that the optimization process consumed more time than initially estimated. Therefore, the last stage could not be conducted.

¹A comprehensive airfoil optimization should include experimental validation of the numerical results and iteratively model adjustment.

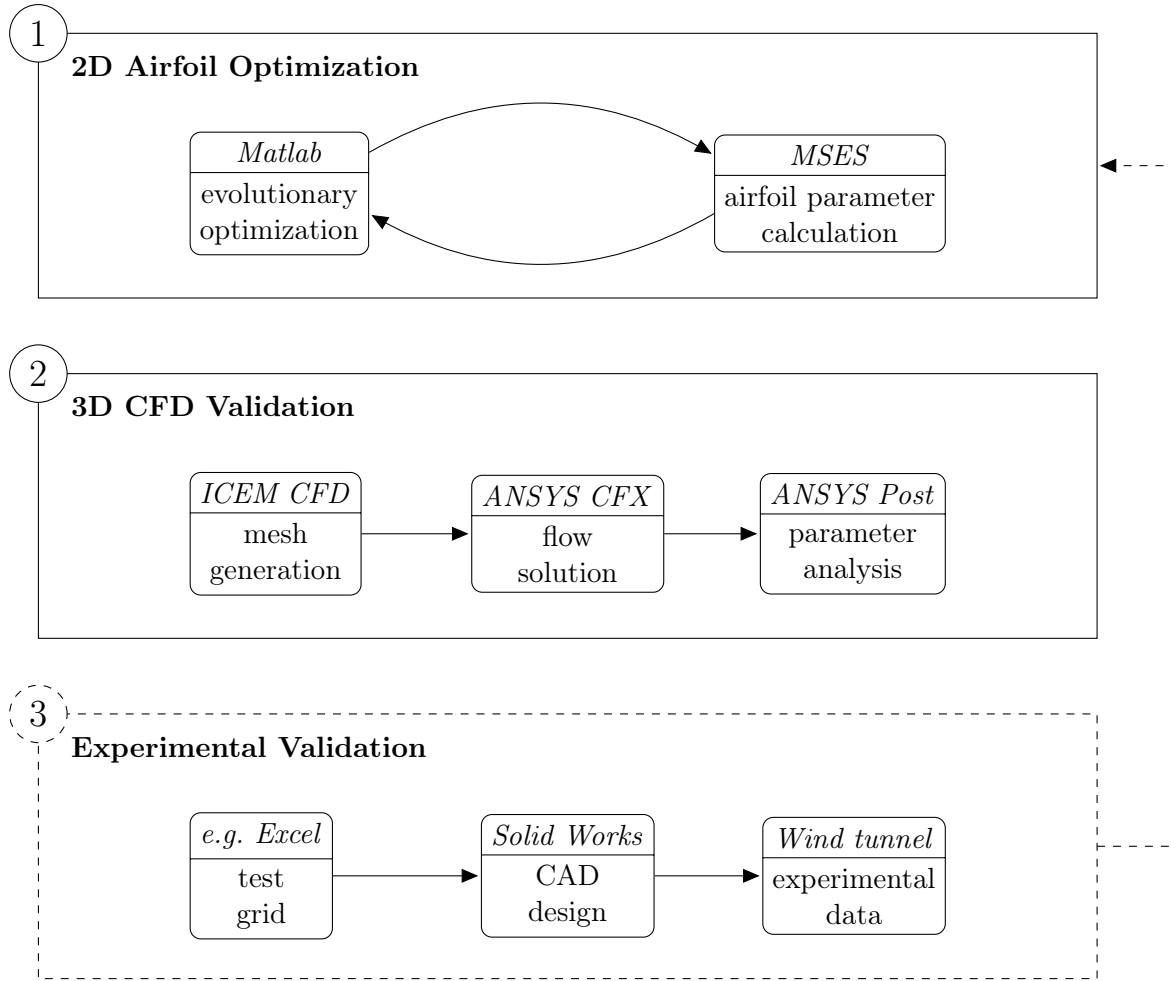


Figure 1.2: Step 1 and 2 were conducted in this work. The third step and the iterative execution could not be conducted (indicated by dashed outlines) during the available time, but are listed here to emphasize the importance of experimental validation.

This is very unfortunate, because (i) the completeness of optimization, simulation, and experimental validation is ruptured and (ii) the experimental data could not be used to iteratively increase the accuracy of the design process.

1.3 Work Plan and Necessary Resources

The system information of both computers which were utilized in this work is listed in table 1.1. The Fujitsu PC was used for both, the optimization process and the CFD analysis. The laptop was only used for the former.

Table 1.1: System specifications of the PCs used in this work.

Computer model	OS	Processor	Clock Rate	Cores	RAM
Fujitsu Esprimo P756	Ubuntu 18.04 Windows 10	i5-6400	2.7 GHz	4	16 GB
HP EliteBook 8560p	Ubuntu 18.04	i7-2760QM	2.4 GHz	4	12 GB

Matlab R2018a and MSES 3.05 were installed on both machines. The console program MSES was originally written for 32-bit operating systems. However, the availability of commonly used software is limited on those systems. Hence, the software was compiled for the 64-bit systems without any necessary adaptations. The installation was conducted following the instructions from [22].

For the CFD analysis the ANSYS software bundle was installed on the Windows operating system. The programs were obtained under the ANSYS Academic License. Compared to regular licenses, the maximum number of nodes is limited to 512k [23].

Before commencing with the optimization process, a schedule was created which structured the different stages from fig. 1.2. The initial schedule is given in the appendix A.1.

Fundamentals

There are different variants of kite power systems which are currently being developed or have at least been conceptualized. The following chapter presents the fundamentals of crosswind kite power systems on the basis of the *drag-power* variant, which is the research focus of the project at the TUM. Interested readers are referred to literature for information on other kite technologies (e.g. [19, 24, 18]).

First, the technology is introduced and the physics of wind power extraction are explained. Aerodynamic principles and design aspects for (high-) lift generation are introduced. Phenomena which are used to describe fluid motion are introduced, turbulence modeling explained. The chapter is completed with information about evolutionary optimization by giving an overview of the algorithm used in the presented work: The Covariance Matrix Adaptation Evolution Strategy (CMA-ES).

2.1 Drag Power Kites

Drag-power kite systems—as well as all system variations—consist of three main system components: A ground station, the airborne kite itself, and a tether connecting the two, as shown in fig 2.1. During operation the kite is flown in circles or in figure eights [18].

One function of the ground station is being an anchor point for the flying kite's tether. Only this fixation makes it possible to harvest the kinetic energy of the wind by decelerating its movement relative to the ground [19, p. 3]. The ground station also houses the power electronics which convert the energy generated by the kite to alternating current (AC) at power grid voltage [25]. The third major function is to offer a mount for the kite to land on when it is not in operation or when maintenance is due [19, ch. 1].

The airborne component of the system is a hard wing made out of materials such as carbon

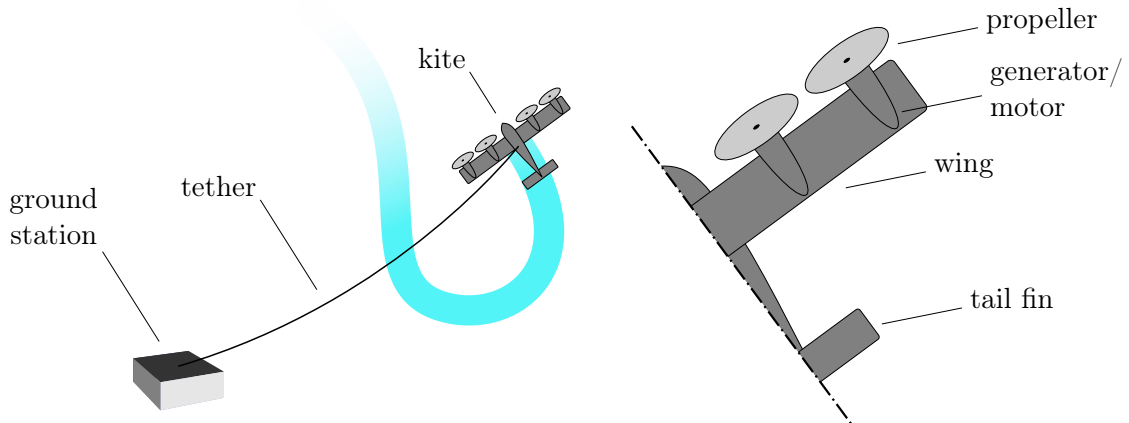


Figure 2.1: Schematic of a drag-power kite system showing the components ground station, tether and kite, as well as on-board components of the kite.

fiber reinforced plastic (CFRP) [18, p. 3135]. Fig. 2.1 shows its resemblance to a small airplane due to on-board electrical machines. These machines are equipped with propellers and can be used as motors during take-off and landing or as generators during operation. This setup eliminates the prominent difficulties that systems with ground based generators have to initialize flight and dispatch the kite into operating heights [19, p. 7]. The kite's airfoils have to have certain aerodynamic properties to enable highest energy outputs. These characteristics are further elaborated in section 2.3.

The mechanic-electrical tether attaches the kite to the ground station, enables communication by transmitting control signals between the ground station and the kite and is—of course—used to conduct electrical power. The transmission of the electricity is bi-directional [25, sec. 2.4]. During operation, i.e. whilst transforming kinetic energy of the wind into electric energy, the on-board generated power is transferred from the kite to the ground station. During take-off and landing the kite is drawing electricity from the grid to operate the electrical machines as motors [19, p. 7].

The small-scale system which is developed at the TUM has a nominal power of ~ 20 kW, generated by eight on-board propellers. With a tether length of just above 110 m it operates at an altitude of 80 m. It is designed for the operation in island-grids with high LCOEs of 0.30 €/kWh. To achieve this level of costs a nominal apparent airspeed at operating heights of $v_{a,n} = 38.89$ m/s is necessary¹. Lift is generated by a bi-plane structure made up of high-lift multi-element airfoils with a wingspan of 2.4 m.

2.2 Power Generation

The basic equation for lift power generation was developed by Loyd in 1980 [1]:

$$P = \frac{1}{2} \rho v_w^3 A C_L P_{L,rel} \quad (2.1)$$

It depends on the density of the fluid ρ , the cubed wind velocity v_w , and the projected wing area of the kite A . It shows the strong influence which stronger winds have on the power generation.

The lift coefficient C_L is an aerodynamic parameter of the kite (or wing), which relates the generated lift force F_L perpendicular to the oncoming wind to the density of the fluid and its velocity. The same relation can be given for the drag force F_D and the drag coefficient C_D [3, sec. 1.5]. Both forces are linearly proportional to the projected surface of the wing A . Lift and drag coefficients are heavily investigated in aeronautics and are important parameters for the definition of cost functions for airfoil optimization (cf. sec. 4.5).

$$F_L = \frac{1}{2} \rho v_a^2 A C_L \quad (2.2)$$

$$F_D = \frac{1}{2} \rho v_a^2 A C_D \quad (2.3)$$

The last factor of eq. 2.1 is the relative lift power $P_{L,rel}$. Depending on whether the power is generated in lift mode or drag mode, this parameter is defined differently. For drag-power kites it is given to [1, p. 108]

$$P = F_{D,rot} v_a \quad (2.4)$$

Fig. 2.2 shows the forces and velocities acting on a kite in crosswind motion. The projected force and velocity triangles are congruent:

$$\triangle F_T F_L F_D \cong \triangle v_a v_c v_w \quad (2.5)$$

¹Equal to wind speeds v_w from 11.50–19.25 m/s.

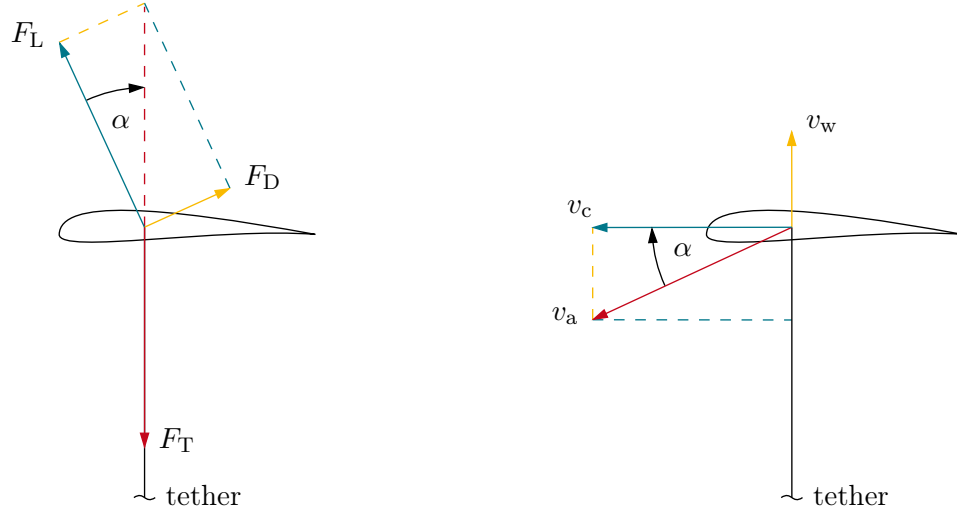


Figure 2.2: Velocities and forces acting on a drag-power kite. Adapted from [1, p. 108] and [2, p. 4].

Using the small-angle approximation² the apparent wind speed v_a can be approximated

$$v_a = \frac{v_w F_L}{F_{D,k} + F_{D,rot}} \quad (2.6)$$

By combining eq. 2.1, 2.3, and 2.6 the relative lift power can be determined.

$$P_{L,rel} = \left(\frac{F_L}{F_D} \right)^2 \frac{\frac{F_{D,rot}}{F_{D,k}}}{\left(1 + \frac{F_{D,rot}}{F_{D,k}} \right)^3} \quad (2.7)$$

Eq. 2.7 becomes maximum at $F_k/F_{D,rot} = C_k/C_{D,rot} = 2$. This drag ratio is an important design aspect of drag-power systems.

$$P_{L,rel} = \frac{4}{27} \left(\frac{F_L}{F_{D,k}} \right)^2 \quad (2.8)$$

The maximum power P for drag power kites can be given:

$$\hat{P}_{L,rel} = \frac{2}{27} \rho v_w A \frac{C_L^3}{C_D^2} \quad (2.9)$$

It is important to note, that this is a purely theoretical value which states an upper limit of what is achievable. Energy losses which are not considered here include, but are not limited to

- Mechanical losses in the shafts and gear [2, p. 12]
- Losses in the electrical components (e.g. tether, power electronics, transformers) [2, p. 12]
- Weight effects of the tether and the airborne kite itself [19, p. 14, 15]
- Aerodynamic losses (e.g. due to sideslip) [2, p. 5]

²For flow conditions at low Reynolds Numbers the ratio of the lift to the drag force F_L/F_D for common high lift airfoils is ~ 45 . The corresponding glide angle then follows to $a = \tan^{-1}(1/45) = 1.27^\circ$ for which the small-angle approximation is valid.

These deductions allowed Loyd the prediction of significantly high power outputs for crosswind kites. Fagiano et al. quantified the superiority of crosswind power over lift power by a factor of 50 for semi-rigid wings. Even higher values can be achieved with fully rigid wings. [18, p. 3136]

In literature (e.g. [18]) the expression $(F_L/F_D)^2$ in eq. 2.9 is often substituted by the aerodynamic efficiency E . However, the maximum extracted power in eq. 2.9 is proportional to C_L^3/C_D . It is therefore important to focus on the optimization of the lift C_L and not on the aerodynamic efficiency E [21].

The effect of the azimuth and elevation angle can be taken into consideration with the concept of the glide angle a (cf. [20, p. 3–5]). It was not included in this simplified analysis, because it is not necessary to show the correlation of the extracted power to lift and drag coefficients. The following aerodynamic considerations therefore always refer to the angle of attack (AOA) (α).

2.3 High Lift Airfoil Geometry

2.3.1 Airfoil Nomenclature

The basic shape of an airfoil is illustrated in fig. 2.3. The chord line connects the leading edge (LE) to the trailing edge (TE) and defines the reference points for the length of the airfoil l_c . The camber line represents all the points with equal distance to upper and lower airfoil surface. For each airfoil, the maximum vertical distance between the chord line and the mean camber line is called *camber*. [3, sec. 4.2]

If an airfoil is pitched, the AOA describes the angle between the chord line and a horizontal reference line. The projected length of the chord line onto the horizontal line is then called reference chord length $l_{c,ref}$. This parameter is an important length for the determination of the *Reynolds Number* introduced in sec. 2.4.

2.3.2 Take-Off and Landing Devices

Slats and flaps have long been of interest for commercial airplanes. Their use enables adaptation to varying operating conditions during take-off and landing. These classical adaptations of wings in forms of flaps and slats can be seen as a step towards multi-element wings with increased lift. [6, p. 494]

Flaps are small wing sections which are positioned downstream of the TE, usually with adjustable deflection. Their rotation can be interpreted as an increase in effective camber and results in higher lift and drag coefficients. Higher C_L values are beneficial in terms of airport

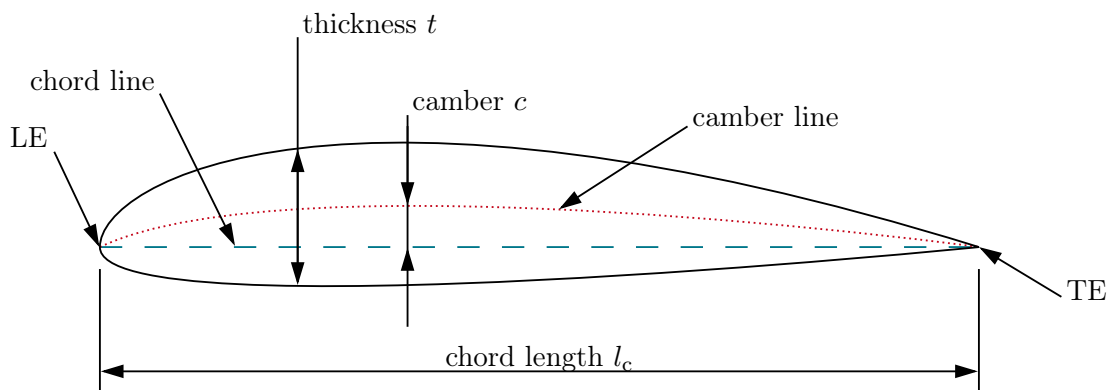


Figure 2.3: Basic airfoil nomenclature. Adapted from [3, p. 280].

design where shorter take-off and landing strips can be planned. A higher drag coefficient, however, is not beneficial for long-distance flights. Fuel has to be saved and therefore the flaps are rotated back in alignment with the main wing. [6, ch. 8]

Similarly to flaps, slats are extendable surfaces at the LE of wings which are used to increase the maximum lift of an airfoil. They do not change the camber of an airfoil significantly and are thus not increasing the overall lift. Higher maximum lifts can be reached because stall occurs at larger AOA. [6, p. 494, 498]

2.3.3 Multi-Element Airfoils

The *Drag Power Kite with Very High Lift Coefficient* developed at the TUM incorporates two features to fulfill what is implicated by its name: A biplane setup and a multi-element high lift airfoil [20]. The biplane structure doubles the total surface area of the kite's wing and increases the overall stability of the airfoils by means of a truss-like structure. This arrangement allows to counteract any possible deformations of the high lift multi-element airfoils due to high loads. The benefits outweigh any aerodynamic interactions between the two planes. [21]

The positive effects of dividing an airfoil into multiple elements were discovered at the beginning of the 19th century [26]. Handley Page presented an empirical proof of higher overall lift, higher maximum lift, and greater stall angles [27, sec. 14.3.2]. The underlying aerodynamic effects of devices like flaps, slats, and those of multi-element arrangements are explained in more detail in section 2.4.5.

2.4 Fluid Dynamics

2.4.1 Conservation Laws

The conservation laws describe fluid motion within a confined volume. Compared to the *Boltzmann Equation*, which describes fluid motion based on the interaction of fluid particles, these laws describe flow within a continuum. Three equations prescribe the net flow of mass, momentum, and energy within, into, and out of a defined control volume and conclusions regarding the flow field can be drawn. [4, ch. 5]

The conservation of mass states that any change of mass over time within a volume Ω is equal to the flows over its surface Γ [4, p. 189].

$$\frac{\partial}{\partial t} \int_{\Omega} \rho d\Omega = - \int_{\Gamma} \rho \mathbf{v} \cdot \mathbf{n} d\Gamma \quad (2.10)$$

The dot product on the right hand side quantifies how much of the fluid with velocity \mathbf{v} is traversing the volume surface defined by the normal vector \mathbf{n} . The density ρ of incompressible fluids is constant over time and the left hand side nullifies. As a consequence, the net flows over the volume surface Γ have to balance out to zero as well.

Newton's second law, describes the conservation of momentum. It states that time rate change of the system momentum is equal to all external forces. The system momentum is divided into the change of momentum of the control volume and the amount of momentum which passes through the volume's surface Γ . [4, p. 201]

$$\frac{\partial}{\partial t} \int_{\Omega} \mathbf{v} \rho d\Omega + \int_{\Gamma} \mathbf{v} \rho \mathbf{v} \cdot \mathbf{n} d\Gamma = \sum_{\Omega} F_{\text{vol}} + \sum_{\Gamma} F_{\text{surf}} \quad (2.11)$$

The third law of conservation is the conservation of energy, which states that energy cannot be created or destroyed. The sum of the energy within the volume and crossing over its surface is equal to all heat or work transferred into the system. [4, p. 224]

$$\frac{\partial}{\partial t} \int_{\Omega} e \rho d\Omega + \int_{\Gamma} e \rho \mathbf{v} \cdot \mathbf{n} d\Gamma = \dot{Q}_{\Omega} + \dot{W}_{\Omega} \quad (2.12)$$

The first term on the left describes the temporal change of the mass-specific energy e and the density ρ . For incompressible flows this term simplifies to $\int_{\Omega} \dot{e} \rho d\Omega$. If neither external heat \dot{Q}_{Ω} , nor external work \dot{W}_{Ω} is transferred into or out of the system, the change of the internal energy \dot{e} within the volume compensates the energy transfer due to mass transport across its surface. [4, p. 224, 225]

2.4.2 Incompressibility Assumption

The pressure field within a flow volume is dependent on the flow velocity. The pressure difference from the static pressure p_{static} to the stagnation pressure p_{stag} can be calculated with the density ρ and the flow velocity v . Elevation effects are accounted for by the elevation height h and the potential g . [4, sec. 3.5, 11.3]

$$\Delta p = p_{\text{stag}} - p_{\text{static}} = \frac{\rho v^2}{2} + gh \quad (2.13)$$

A change in density (i.e. compression) leads to a change in pressure difference. This correlation is amplified by the squared velocity of the fluid. At low velocities the influence of the density on the pressure field is not significant, but at higher velocities it becomes distinct.

The Mach number Ma can be used to classify flows by whether a change in density has a significant influence on the pressure field based on the fluid speed. The Mach number relates the flow velocity v to the speed of sound c . If it is below a value of 0.3 the described influence is considered negligible and the flow can be considered incompressible because no significant error arises from the assumption of a constant density. [4, p. 591]

$$\forall Ma < 0.3 : \quad \frac{\partial}{\partial t} \rho = 0 \quad (2.14)$$

2.4.3 Inviscid Flow

The *Navier-Stokes-Equations* are a system of partial differential equations which describe the motion of Newtonian fluids (cf. sec. 2.4.4). For incompressible flows they can be formulated by combining the conservation of momentum (eq. 2.11) and the continuity equation (eq. 2.10). The spatial system of four equations can then be solved for the four unknown parameters \mathbf{v} and p . To do so, boundary and initial flow conditions have to be declared. For compressible flows a fifth parameter is unknown: The density of the fluid ρ . In that case, the system of equations is extended by the conservation of energy (eq. 2.12). [28, ch. 2]

The Navier-Stokes-Equations can further be simplified by introducing the assumption of inviscid flow, which leads to the *Euler Equations of Motion*. [28, ch. 4]

$$\rho \mathbf{g} - \nabla p = \rho \left[\frac{\partial \mathbf{v}}{\partial t} + (\mathbf{v} \cdot \nabla) \mathbf{v} \right] \quad (2.15)$$

The spatial equation relates the fluid velocity \mathbf{v} , density ρ , and the pressure p within a control volume under the influence of body forces, e.g. gravitational forces expressed by \mathbf{g} . For stationary flows along a streamline, the equation can further be simplified to the *Bernoulli Equation*. [4, sec. 6.4]

$$\frac{p}{\rho} + \frac{v^2}{2g} = -gh \quad (2.16)$$

2.4.4 Boundary Layer Theory

Boundary layers are used to describe the behavior of fluids in the vicinity of surfaces (i.e. airfoils) where the viscosity of the fluid dominates the flow behavior. The concept completes the inviscid

formulations of the Euler Equations, which are sufficient to describe free-stream flows and allows the investigation of fluid-object interaction. [5, sec. 1.7]

The viscosity μ is a physical property of the fluid and relates the wall shear stress τ_w of the fluid to the gradient of the velocity u parallel to the surface. This correlation is called *Newton's law of friction*. [5, sec. 1.2]

$$\tau_w = \mu \frac{du}{dy} \quad (2.17)$$

For all gases and most technical fluids the relation between the shear stress and the velocity gradient is linear. Such substances are called *Newtonian Fluids*. [5, p. 5]

Depending on the characteristics of the flow, inertial forces are often present additionally to viscous effects. The *Reynolds number* is a dimensionless number which relates these inertial forces to friction forces. It is used to make different flow problems comparable. Similar Reynolds numbers resemble the prevalence of similar forces. [5, p. 7]

$$Re = \frac{vL}{\eta} = \frac{\rho vl}{\mu} \quad (2.18)$$

The kinematic viscosity η combines the density ρ and the viscosity μ of the fluid. The characteristic length L is problem-specific. For flows over airfoils the characteristic length is set to the reference chord length $l_{c,ref}$ (cf. sec. 2.3.1).

For given Re and Ma values, flow can be categorized as either *laminar* or *turbulent*. Laminar flow is fluid motion structured in planes with different velocities. No significant exchange perpendicular to the direction of flow between the different planes is present. Turbulent flow indicates chaotic fluid movement. Strong interaction overlays the general flow in form of irregular energetic exchange between what used to be distinct planes. [5, p. 13]

As stated above, the boundary layer (BL) defines the flow region adjacent to an object's surface. Close to the LE it is laminar, as shown in fig. 2.4. As its thickness δ increases with increasing distance to the LE, the transition point S is approached. S marks the point at which the laminar BL becomes turbulent. It can be identified by an increase in thickness and in wall shear stress. At this point, the Reynolds number³ reaches its critical value Re_{crit} . This value is influenced by the grade of disturbance in the outer flow. More turbulent outer regions lead to earlier BL transition. [5, sec. 2.3]

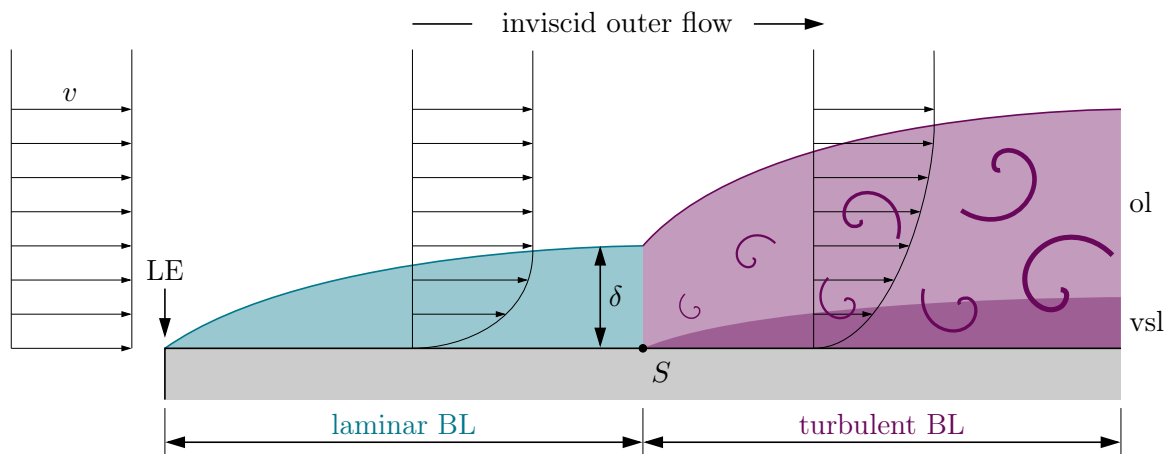


Figure 2.4: The boundary layer increases steadily along the surface. At first it is **laminar**, but after reaching the transition point it turns **turbulent**. This point is marked by the critical Reynolds number Re_{crit} . Adapted from [4, p. 471].

³For the determination of the transition point of airfoils, the Reynolds number of a specific point is calculated by setting the characteristic length in eq. 2.18 to its distance from the LE.

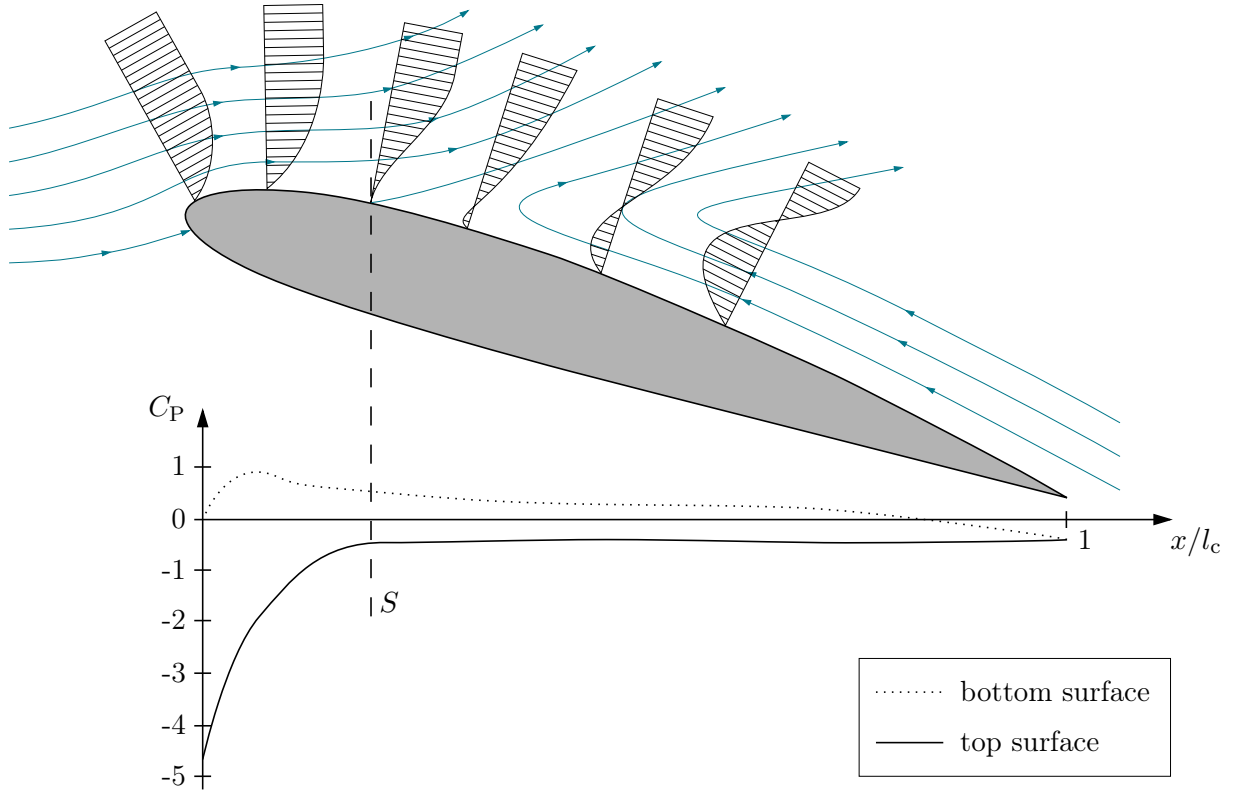


Figure 2.5: Stall occurs at $Re = 2.7 \cdot 10^6$ and an angle of attack of 17.9° . An adverse pressure gradient leads to the inversion of the velocity gradient parallel to the surface of the NACA 2412 airfoil. At the separation point S , the velocity gradient vanishes ($du/dy = 0$) which results in a shear wall stress τ equal to zero (eq. 2.17). Velocity gradients adapted from [5, p. 41], pressure coefficient from [6, p. 29].

The turbulent BL is subdivided into two regions: the outer layer (ol) and the viscous sublayer (vsl) (see fig. 2.4). Only within the latter viscous forces prevail. It is thin compared to the vsl which is dominated by turbulent, fluctuating motion. [5, sec. 2.3]

2.4.5 Flow around Airfoils

The pressure within the BL of an airfoil is mainly imposed by the outer flow conditions. The pressure gradient perpendicular to the surface is very small, because the effects of the curvature and the centrifugal forces are small. Therefore, the pressure in the BL only changes with respect to the flow direction [5, p. 38]. The pressure coefficient C_P relates the pressure p at a certain position along the airfoil to local airspeed v .

$$C_P = \frac{\Delta p}{\frac{1}{2}\rho v^2} = \frac{p - p_\infty}{\frac{1}{2}\rho v^2} \quad (2.19)$$

A sudden decrease in airfoil thickness towards the TE, a blunt TE, or high α -values (stall) can lead to an increase in pressure at the surface of the airfoil, which in turn can lead to BL separation. BL separation is an effect which arises from the energy loss of near-wall fluid particles. The kinetic energy of fluid particles decreases while flowing over the airfoil. This is visualized by the diminishing velocity gradient of streamlines close to the airfoil surface in fig. 2.5. If too much energy is lost, the increased pressure towards the TE cannot be overcome. As a result, the near-wall particles are halted (indicated by the separation point S) and pushed back into the bulk flow, away from the airfoil's surface. [5, sec. 2.6]

To explore the influence of boundary layer separation on the lift or drag of an airfoil, a closer look has to be taken on the principles behind these forces. The oncoming flow is divided into upper and lower flow at the stagnation point $P_{\text{stag,LE}}$ near the LE (fig. 2.5). The flow passing below the airfoil is slowed down, which—according to the Bernoulli equation—results in higher pressures. Whereas the air passing above the airfoil is accelerated by converting pressure energy into kinetic energy. This pressure difference results in a net force: the lift. Consequently, inviscid flow calculations can approximate the lift force quite accurately. [6, sec. 2.2]

At very small Reynolds numbers the oncoming flow separates close to the LE. The laminar separation is caused by a sharp increase in pressure on the suction (upper) side of the airfoil. In this region, the maximum lift coefficient is independent of the Reynolds number. Only with increasing values does this behavior change. [6, sec. 2.5.1]

At higher Re numbers, the following flow characteristic establishes: Laminar flow separates close to the LE, transitions to turbulent flow, and finally reattaches to the airfoil further downstream. The enclosed area is called *laminar separation bubble*. Laminar separation bubbles are separated areas of circulating air which do not interchange with the surrounding flow. This causes a disruption in the velocity and pressure distribution leading to changes in lift and drag. An increase in Reynolds number causes the reattachment point to move further upstream, closer to the LE. The separation bubble is minimized and the maximum lift increases. [6, sec. 2.5.1]

At regions of very high Reynolds numbers, the transition from laminar to turbulent BL occurs before the separation from the profile. This leads to an overall increase in BL thickness and might result in slightly lower lift coefficients, but prevents the separation of flow from the profile in the first place, which would have more severe effects on the lift. [6, sec. 2.5.1]

Contrary to the lift, the drag force cannot be explained solely by inviscid theory. It consists of the friction-related profile drag and the induced drag. Induced drag is proportional to the square of lift coefficient. It quantifies flow processes at the wing tips and can be explained with inviscid theory [29, sec. 7.4]. At high lifts, the profile drag increases significantly due to local separation. In regions of lower lifts this effect diminishes and the profile drag is dominated by surface friction effects. It is dependent on the shear stress on the airfoils surface and thus, correlated to the turbulent fraction of the BL. At higher Reynolds numbers the pressure drag decreases [6, sec. 2.5.5].

Maximum lift design of airfoils aims at either ensuring turbulent flow from the beginning, so no laminar separation occurs or at maintaining laminar flow for as long as possible [6, p. 95]. The following design measures are common approaches to achieve the desired airfoil properties⁴:

1. Design the upper side of an airfoil in such a way, that the resulting pressure gradient shifts flow separation as far away from the LE as possible. As a result, a larger section of the BL stays laminar. [27, p. 531]
2. Use turbulators to evoke early transition. Turbulators are mechanical adaptations or pneumatic devices which introduce turbulence at a specific distance from the LE. An earlier transition—and therefore no formation of a laminar separation bubble—improves lift at low flight velocities. The downside is that higher drag prevails at higher airspeeds. [30]
3. Use a connected flap to deflect the air stream downwards. The emerging hinge moment can be minimized by a control surface or a shift of the rotational axis. [6, p. 481]
4. Add a small, separated flap behind the main element. A vortex forms in the high pressure area of the flap. As a result, the boundary layer close to the TE becomes thinner and is less likely to separate. Similar to the connected flap, the flow from the airfoil is directed downwards. Drag usually increases, but sometimes reduces [27, p. 536]. A slotted flap also

⁴*Remark:* This work focuses on the maximization of lift. Similar considerations can be made considering the minimization of drag, which can be found in literature (e.g. [27]).

increases the load on prior elements which leads to higher lifts due to increased upper-surface velocities of the up-stream element [6, sec. 8.2.1] [31, sec. 5.5]

5. Install slats. The induced vortex behind the slat acts in the opposite direction of the vortices which might establish on the downstream element. The positive effect on airfoil lift due to slats is secondary. The main effect are reduced pressure peaks, resulting in later stall. [31, p. 518]

While the first point can be taken as an advice for the general airfoils, points 3–5 are especially interesting for the design of multi-element airfoils, as they can be seen as an arrangement of multiple slats/flaps. If designed in a sophisticated manner, the following aerodynamic mechanisms can be taken advantage of [31, ch. 5]:

Vortex effect The formation of vortices behind upstream elements and before downstream elements has advantageous effects on the flow field of the adjacent element, as described above.

Dumping effect Boundary layers are forced to separate by the arising pressure gradient towards the TE. Regions of lower pressure coincide with higher airspeeds. Downstream elements have exactly that effect on preceding TEs: air flow on the upper side of the element is accelerated, mitigating the adverse pressure gradient on the upstream element.

Fresh-boundary-layer effect For a given airfoil configuration the total chord length can be split up into multiple, shorter airfoils with shorter boundary layers. Shorter (and therefore thinner) boundary layers can better withstand adverse pressure gradients.

Off-the-surface deceleration While passing over the airfoil, the BL is slowed down, might not be able to overcome the pressure gradient and separates into the bulk flow. If the BL flows off the surface with high velocities in form of a wake, it can decelerate within the freestream. Such a detached separation is more efficient.

2.5 Optimization

2.5.1 Evolutionary Algorithms

Evolutionary algorithms are meta-heuristic approaches with the ability to evolve and learn from the problem. They are based on biological evolution through selection, and mimic the steady improvement of organisms to their environment. Much alike, through evolution, evaluation, and selection, evolutionary algorithms are optimization methods which find global optima by sampling and adapting to the problem topology. Exactly that is their advantage over conventional approaches: The theoretical capability of finding the global optimum. However, to do so, increased computational resources are necessary. Evolutionary algorithms are based on three main principles [7, sec. 1.2]:

1. **Population:** During each iteration, a set of multiple parameter combinations, referred to as the population, is evaluated. Each individual is examined in order to generate learning based on which the next population is generated.
2. **Fitness:** During evaluation, each individual is assigned a fitness value (by definition of a cost function, in classical terms). It quantifies the suitability of each solution with its specific set of parameters for the problem.
3. **Variation:** Following the evaluation with the fitness function, a new population is generated based on the superior candidates. The genes (parameter combinations) of the selected individuals are combined and mutated (cf. [7, sec. 3.2.1, 3.3.4]). This way, new solutions are generated which are similar, yet slightly different from their predecessors.

Base on those principles, the algorithm moves across the problem domain. A region is sampled, the best solutions are selected and altered, and then, the search is continued in the direction of the most promising candidates. Compared to gradient-based methods, the design of the fitness (cost) function is the less-demanding: No differentiability has to be guaranteed because the search is not guided by gradients, but by multiple sampling points (individuals of the population). [7, sec. 1.2]

2.5.2 Covariance Matrix Adaptation Evolution Strategy

Classified as an adaptive control method, the main difference of Covariance Matrix Adaptation Evolution Strategy (CMA-ES) compared to deterministic algorithms is that the strategy parameters of the optimization are not solely based on heuristic rules depending on the fitness of the generation, but also rely on feedback from the previous population [7, p. 83]. Search efficiency is improved by simultaneously reacting to non-separable variables. Search directions are enhanced and less search steps required, as shown in fig. 2.6a. [7, p. 95]

First, N individuals, defined by parameter vectors \mathbf{x} , are generated⁵ by the definition of a normal distribution with expectation (mean) $\mathbf{a}^{(0)}$ and parameter covariance matrix $\mathbf{B}^{(0)}$.

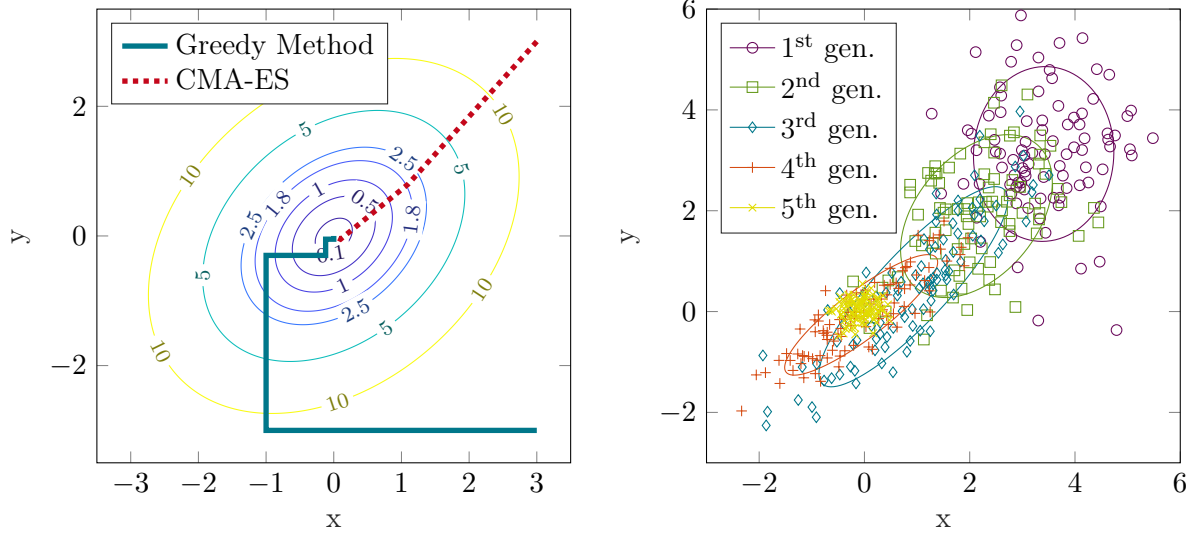
After selecting the N_{best} best individuals, a new covariance matrix can be calculated.

$$\mathbf{B}^{(g)} = \frac{1}{N_{\text{best}}} \sum_{i=1}^{N_{\text{best}}} \left(\mathbf{x}_i^{(g)} - \mathbf{a}^{(g-1)} \right) \left(\mathbf{x}_i^{(g)} - \mathbf{a}^{(g-1)} \right)^T \quad (2.20)$$

Based on the new covariance matrix the expectation for the distribution of the new generation can be determined.

$$\mathbf{a}^{(g)} = \frac{1}{N_{\text{best}}} \sum_{i=1}^{N_{\text{best}}} \mathbf{x}_i^{(g)} \quad (2.21)$$

⁵Superscripts in parenthesis indicate the generation.



(a) Search on non-separable variables: CMA-ES (b) Population of each generation with ellipsoid around all individuals within $1 \cdot \sigma$.

Figure 2.6: Advantages and workings of the CMA-ES algorithm. Adapted from [7, p. 46, 94, 95].

What was previously stated is now clear: The new generation is not generated based on the fitness of the prior population, but based on the correlation between the parameters. The density function, which is responsible for the distribution of the new generation, is dynamically adapted to guide the algorithm in the most promising search direction. In fig. 2.6b, the evolution of different generations stretching towards the optimum is depicted. [7, p. 94, 95]

Research and Technology

The following chapter gives an overview of the field of airfoil optimization. Different optimization strategies are presented and the general shift from analytical approaches towards the numerical methods used nowadays is outlined. The chapter is completed by an introduction of previous work which builds the foundation of the presented thesis.

3.1 State of the Art

For a long time, airfoil optimization has been a focus of research in the aeronautic community. Early investigations and developments have been driven by the aspiration of military superiority (cf. [31]) or the need to build fuel-efficient transport and commercial aircrafts (cf. [26], [32]). The constant improvement in computational capacities and their common availability has always resembled an important limitation factor. For that reason, early investigations have relied on simplified analyses. A main challenge was the lean design of the optimization process itself. Even though computing capacities¹ have increased by a factor of around 10^{10} since the 1960s [33], exactly that challenge still remains today (e.g. [34], [35], [31]).

A common approach for airfoil optimization is the inverse airfoil design method found in multiple papers (e.g. [31], [36], [37], [37]). In [36], the desired distribution of the velocity distribution has been defined along the surface of the airfoil. The outer (inviscid) flow has been solved in combination with the BL equations. The velocity distribution of the initial airfoil shape has been used to determine the differences to the desired distribution. This information has then been used to deform specific points on the surface of the airfoil. The prescription of such a distribution, however, has been found to be very complicated—if not impossible. Smith has stated, that *“every shape has a corresponding pressure distribution, but not every pressure distribution has its shape”* [31, p. 524].

A different optimization approach along with the software for its execution has been presented by Drela [38, 39]. It includes a meshing program, a flow solver and an optimization tool called LINDOP. In [38] this tool has been used in to analyze the suitability of the developed method for airfoil optimization. Drag-minimization has been conducted for the low Reynolds number airfoil DAE-11.

The suitability of optimization in the process of airfoil design has been judged by multiple assessments [38]. The definition of an objective function and additional constraints have been found important for a proper description of the optimization problem [38, p. 17]. Drela has pointed out the importance of the definition of constraints to limit the design space in which the optimization is conducted. Such definitions have helped to avoid too thin airfoils or excessive pitching moments [38, p. 3, 4].

The same paper has also concluded that an elaborate parameterization of the airfoil geometry could prevent over-fitting to aerodynamic effects. The parameterization of the airfoil shape with sinusoidal functions along the circumference of the 2D cross section has been used. During optimization, this led to the formation of bumps which filled the space of any occurring laminar

¹Calculations per second per 1 000\$.

separation bubble(s) on the suction side of the airfoil [38, p. 5–10]. As another countermeasure, the optimization at multiple operating points (OPs) has been proposed. The operating points should be designed to cover not only the span of later operation of the airfoil, but airspeeds beyond that [38, p. 16, 17].

To improve accuracy, instead of using programs which incorporate different solvers for the viscous and inviscid areas with interactive coupling, research has greatly benefited from CFD simulations solving the Navier-Stokes Equations over the past few years. Multiple publications have achieved great accordance with experimental results (e.g. [40], [41], [42], [43], [44]). However, accuracy comes at a price. The authors of [35] have found that the completion of one optimization loop which coupled the flow solutions of a Reynolds Averaged Navier-Stokes (RANS) solver to a genetic algorithm² took 4–5 days. The optimization has consisted of a first approximation with a medium resolution mesh with 22.5k cells and subsequent refinement with a mesh of 98k cells.

Benini et al. have presented a widely accepted and used method for the optimization process of airfoils which harnesses the precision of CFD analysis and combines it with the swiftness of low-fidelity solvers [45]. By using the coupled solver MSES during the optimization process and the CFD solver ANSYS Fluent only for the posterior validation of the found optima, the computational costs have been reduced drastically. The paper has investigated the take-off and landing conditions of the NHLP 2-D L1T2 high-lift airfoil. A multi-objective genetic algorithm has been used to calculate the flow solution while respecting a pitching moment constraint. The optimization of the three-element airfoil has been conducted at a Mach number of 0.197 and a Reynolds number of 3.52×10^6 . The numerical results have been compared to experimental wind-tunnel data and have shown good accordance as long as no separation has been present. It has been emphasized that an appropriate parameterization of the airfoil ought to guarantee smoothness and tangential continuity.

Another suggestions for structuring the optimization process found in literature is the subdivision of the optimization problem (e.g. [42], [35], [34]). The process has been split up into multiple, iteratively conducted steps, each focusing either only on element positioning or shape adaptation. It has been found that such a subdivision can help accelerate the design process, because it limits the design space in which the optimization solver has to navigate. However, in [34] it has been pointed out that such a subdivision/minimization of the design space requires prior knowledge of the problem to formulate the engineering-based and physical criteria to do so.

The importance of applying evolutionary algorithms is emphasized by many authors (e.g. [42], [34], [35], [41]). Even though such algorithms require more computational resources, their capability of exploring the whole design space, i.e. finding the global optimum is highly appreciated.

Lastly, it shall be noted that the publications presented up to this point consider general aviation applications due to a lack of information on kite system specific aerodynamics. A lot of research in the field of kite technology considers the control (e.g. [46, 47, 48, 49, 50, 51]), as well as the design of the electric system (e.g. [52, 53, 18]). Fewer research considering the kite design seems to be available, and even less about the design of (multi-element) airfoils specifically for kite applications. The only work known to the author has been presented by Gohl et al. who have designed a framework for the simulation of tethered wings which includes the investigation of aerodynamic efficiency of two different airfoil shapes, but no optimization [19, ch. 18].

Lind has patented multiple design proposals considering kite power systems, two of which bear reference to multi-element airfoil designs. One of them concerns a general kite configuration and flight strategy proposition [54]. Lind has briefly mentioned the use of actuated multi-element airfoils to confine the wing loads in high wind conditions. A second patent has been issued with more information about the airfoil shape and possible *modi operandi* [55]. Along with a sketch of the geometry, a non-quantified C_p slope over a two-element airfoil is given. The patent includes

²Multi-objective genetic algorithm for multi-element airfoils based on the CIRA low solver.

information about the rotational axis of the adjustable downstream element (flap). However, the information available in the patents have not contained any information on the design process of the airfoil geometry.

3.2 Previous Work

The presented work is integrated into a project which has established around the work presented in [21]. Bauer has developed a multi-disciplinary steady-state model for drag-power kites, taking into account various domains such as economics, electrical components, and control theory. The aerodynamics have been modeled using circulation theory based on the *Kutta-Joukowski Theorem*. The overall model predicts the maximum allowable costs for a given configuration by adapting the design parameters. The system of mostly explicit equations is optimized using the genetic CMA-ES (sec. 2.5).

It has been found that the aerodynamic parameters have a high influence on the kite system economics³. Therefore, part of the project has been focused on the design of a high-lift, multi-element airfoil. A biplane structure has been used for the drag-power kite which assures reliable aerodynamic performance even at excessive forces which could otherwise lead to deformation of the wings.

The groundwork of this work has been laid by two⁴ student papers are introduced in the following paragraphs. The first one has addressed the prerequisites necessary for the optimization part of this work in terms of software setup and feasibility of the optimization process. The MSES software bundle has been set up and first optimizations have been conducted using the previously mentioned CMA-ES. [22]

The paper has confirmed what others (e.g. [38], [56]) have found as well: the formulation of the cost function should be done thoroughly. Pruenster has suggested that neither only the lift coefficient C_L , nor the drag coefficient C_D alone should be used to calculate the cost, but a combination of both. The optimization should then be performed over multiple flow conditions which cover the whole operating range using the CMA-ES to find a global optimum. This optimum could then be refined using LINDOP, which is only able to improve a local solution. It has also been noted, that the specific length of the flow problem should reach from the LE of the first to the TE of the last, not only cover the main element. Using an airfoil parameterization different from Drela's has been recommended to speed up the optimization process and prevent the formation of noisy airfoil surfaces [38]. It has also been noted that effort should also be spent on improving the computational performance of the process.

The second paper has investigated the challenges of a CFD analysis and its performance compared to experimental results [8]. An airfoil with four identical elements (cf. [21]) has been used to review which numerical discretization methods and turbulence models are suited for the analysis. A y^+ convergence study has been conducted to judge the mesh requirements. A subsequent wind tunnel experiment has been used to generate measurement data for the validation of the numerical results.

The design of the wind tunnel tester has been found suitable for the experimental investigations. Sufficient surface roughness and precise gap sizing have been found to play an important role. The former has had significant impact on the laminar-turbulent transition at the investigated range of Reynolds numbers from 8×10^4 to 5×10^5 . This way, laminar separation has been avoided and a (mostly) turbulent BL has been guaranteed. For future parametrical investigation, the use of an unstructured mesh was recommended. Even though results have not been as good

³The economic performance is the main criterion for the development of any (wind) energy system. Low LCOE are crucial for the success and spread of such systems. Plant operators (e.g. energy companies, wind farm operators) will always choose the cheapest form of electricity production available. More expensive technologies are steadily being pushed out of the energy mix due to the *Merit-Order* (Germany).

⁴A third one is composed parallel to this work. It investigates the possibilities of using LINDOP for the optimization process.

as those achieved with a structured mesh, the overall faster generation has been emphasized. A y^+ value below five has been recommended for future investigation, which was necessary to resolve the viscous boundary layer. The use of ANSYS CFX was recommended for its overall acceptance in scientific investigations, good correlation to experimental results, applicability for parametric investigations, and a robust convergence behavior. The $k - \omega$ turbulence model was found to be suited for parametric research due to its fast convergence. 3D simulations have been necessary to reproduce the turbulence wake appropriately within a simulated control volume with a width of at least $1l_c$, which represents the turbulence length of the problem.

Airfoil Optimization

This chapter focuses on the airfoil optimization scheme which was implemented in MATLAB. At first, the parameterization method is introduced. The OPs at which the airfoils were evaluated, as well as the base geometries are defined. Finally, the optimization strategy is presented with focus on the implemented cost function and its different regions.

4.1 Airfoil Parameterization

Prior to the optimization an existing airfoil parameterization method was adapted. The set of parameters had to sufficiently describe airfoil geometries similar to common high-lift, low Reynolds number airfoil geometries (e.g. S1223, SOMERS S102) while employing a comparatively low number of parameters. The parameterization was designed to guarantee smoothness along the airfoil surface which inhibited the formation of bumps (cf. [38] or sec. 3.1). Similar to the shape definition through Bézier curves in [45], the airfoil geometry was defined by cubic spline interpolation through multiple points. The number of points varied depending on the parameterization type (PT).

The geometry of any element (be it single- or multi-element airfoils) was defined in a Cartesian coordinate system, normalized along the x-dimension.

$$x \in [0, 1] \tag{4.1}$$

$$y \in [-\infty, \infty] \tag{4.2}$$

The start and end points for the spline interpolation were positioned at the coordinates $(1, 1/2 t_{TE})$ and $(1, -1/2 t_{TE})$, respectively. This way, also blunt TEs could be modeled. The chord line was defined as the connection between the LE at $(0, 0)$ and the TE point with negative y -value at $(1, -1/2 t_{TE})$. The LE was positioned at the coordinates $(0, 0)$, resembling the intermediate point for the spline fitting, as shown in fig. 4.1.

Depending on the PT, additional points were defined for the spline interpolation. The parameterization with the least degrees of freedom (DOF)—PT₁—defined two additional points, P_t and P_b (“top” and “bottom”), which were positioned symmetric to a point P_s on the camber line, as shown in fig. 4.1. The distance from P_s to the LE was defined by parameter a . The second airfoil parameter for camber offset c describes the vertical distance from the x -axis to P_s . The distance between P_t and P_b is defined by the airfoil thickness parameter t .

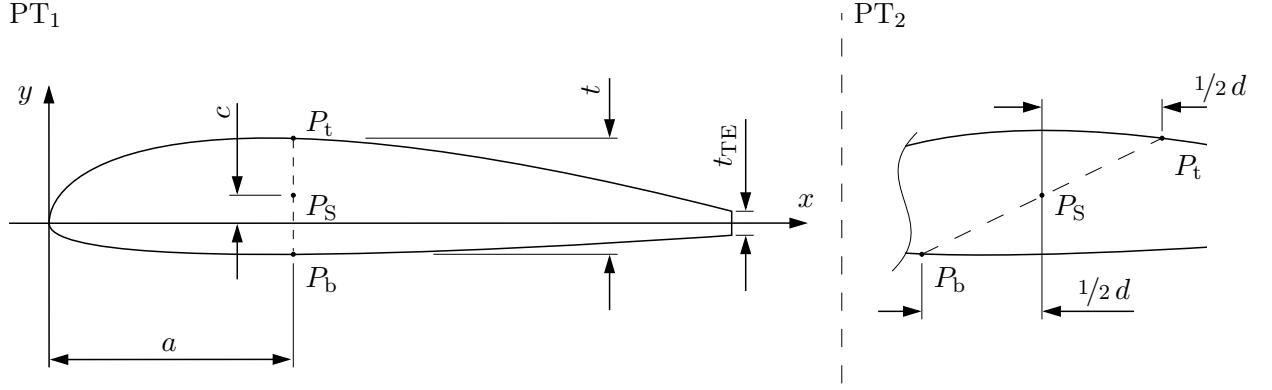


Figure 4.1: The position of the symmetry point P_S is defined by the distance to LE, a , and the camber offset c . The airfoil thickness t defines the vertical distance between two points P_t and P_b , which are positioned above and below P_S . The trailing edge thickness is defined by parameter t_{TE} . PT₂ (right side) extends these parameters by a twisting distance d , which shifts both points P_t and P_b parallel to the y -axis.

PT₂ adds one DOF by enabling point-symmetric twisting of the points P_t and P_b . The twisting distance d quantifies the shift parallel to the y -axis and represents a negative rotation¹ of the two points around their point of symmetry P_S , as displayed on the right side in fig. 4.1.

Both, PT₃ and PT₄ add one additional point each. For each added point, the total number of DOF is increased by four: x , c , t , and d . The anchor points listed in tab. 4.1 were then used for the cubic spline interpolation. The interpolation with 100 segments was implemented using Matlab's `spline` function. Consequently, C^2 continuity² is inherent in the airfoil geometry.

Table 4.1: Types of airfoil parameterizations.

PT	Spline Anchor Points	Shape Parameters	Total DOF
1	5	a, c, t, t_{TE}	4
2	5	a, c, t, t_{TE}, d	5
3	7	a, c, t, t_{TE}, d	10
4	9	a, c, t, t_{TE}, d	15

Besides shape parameters for each element, additional positioning parameters were required as well. The positioning parameters for the first element were defined as the absolute chord length l_c and the AOA. The former was used to describe the total length of the airfoil. Both parameters are referred to the LE of the first and the TE of the last element.

For each subsequent element the vector of relative positioning parameters varied from the one for the first element, as shown in fig. 4.3. The four parameters consisted of two translational and one rotational positioning parameter as well as a scaling factor. The scaling factor ζ allowed the definition of airfoil ensembles with a different chord length for each element. The horizontal and vertical distances from the TE of the upstream element to the LE of the downstream element were defined by Δx and Δy , respectively. The angle between the chord line of the first and each downstream element is referred to as φ .

Summarizing, each airfoil ensemble consists of a collection of shape and positioning parameters. For each element, one vector for the shape and one vector for the positioning parameters

¹In mathematical sense.

²Continuity in value, gradient, and curvature.

was defined. The latter differs for the first element.

$$\begin{array}{ccc}
 \text{shape parameters} & & \text{positioning parameters} \\
 \left[\begin{array}{c} a \\ c \\ t \\ t_{\text{TE}} \\ d \end{array} \right] & & \left[\begin{array}{c} l_c \\ \alpha \end{array} \right] \quad \left[\begin{array}{c} \zeta \\ \Delta x \\ \Delta y \\ \varphi \end{array} \right] \\
 \text{every element} & 1^{\text{st}} \text{ element} & \text{other elements}
 \end{array} \quad (4.3)$$

4.2 Optimization Strategy

The goal of the presented optimization strategy was to find high-lift airfoils of different numbers of elements for the small-scale kite system from [20, sec. 5.2.5]. Starting with the simplest case of a single-element airfoil, the number of DOF were steadily increased. The approach was aimed at finding out whether an increase in DOF always resulted in improved aerodynamic performance. In the end, optimized designs of single- and double-element airfoils with respect to manufacturing constraints and aerodynamic conditions at four OPs were determined.

4.2.1 Operating Points

Following recommendations from [38], the optimization was conducted at four airspeeds within a range slightly extending the system's operational range, as visualized in fig. 4.2. The apparent airspeed ranged from $v_a = 15 \text{ m/s}$ to 52.8 m/s , which covers velocities 10 m/s below and above the estimated minimum apparent airspeed required for a realistic airborne mass $v_{a,\min}$ and the nominal apparent airspeed $v_{a,n}$ of the small-scale system developed in [2, p. 71, 72]. By choosing multiple operating points (tab. 4.2), over-fitting to a single flow condition was prevented.

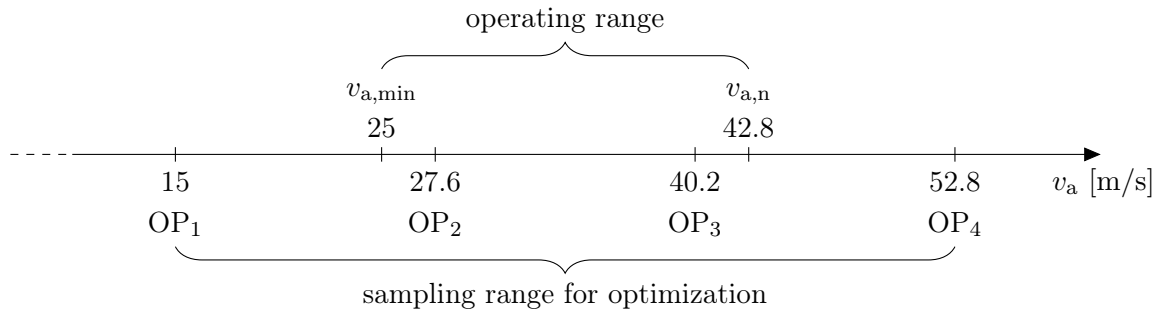


Figure 4.2: The operating range of the small-scale kite system from [2] is limited by $v_{a,\min}$ and $v_{a,n}$. The four operating points which were considered in the optimization are linearly distributed from 15 m/s to 52.8 m/s , extending the system range by $\pm 10 \text{ m/s}$.

The chord length was set to a constant length of 0.167 m during the whole optimization process. The value was determined using equation 2.2 and information about the small-scale system from [21, p. 157]. Following equation 2.18, the Reynolds numbers of the four OPs were determined. All OPs were defined at standard conditions of $T = 25^\circ\text{C}$ and $p = 101.325 \text{ kPa}$. The kinematic viscosity was determined at a relative humidity³ $\phi = 0.7$.

³Mean value for Munich, Germany [57].

Table 4.2: OPs for the optimization process. At all OPs, standard conditions for temperature and pressure apply. The Reynolds numbers were calculated with a chord length $l_c = 0.167$ m.

OP	v_a [m/s]	T [°C]	p [kPa]	ν [m ² /2]	Re
1	15	25	101.325	$1.5486 \cdot 10^{-5}$	$1.6176 \cdot 10^5$
2	27.6	25	101.325	$1.5486 \cdot 10^{-5}$	$2.9764 \cdot 10^5$
3	40.2	25	101.325	$1.5486 \cdot 10^{-5}$	$4.3351 \cdot 10^5$
4	52.8	25	101.325	$1.5486 \cdot 10^{-5}$	$5.6939 \cdot 10^5$

4.2.2 Base Airfoils

Two airfoil base shapes were selected for the investigation. The first one is the Selig 1223 high lift, low Reynolds number airfoil. The airfoil reaches lift and drag coefficients values of around 2.1 and 0.04, respectively, within the range of Reynolds numbers of this work. This airfoil shape is referred to as “1223” in the following. [58]

The second airfoil shape which was used in this work originated from earlier investigations. The airfoil is referred to as “15th”, short for “15 thick”. The name originated due to a thickness t of $0.15l_c$ at P_S . For both base airfoils, geometry and polar plots are provided in the appendix B.

4.2.3 Structure

An overview of the optimization structure is given in fig. 4.3. Each iteration consisted of three steps: The parameterization, the determination, and the evaluation run. At first a base configuration was defined by selecting one of the two base airfoil shapes and the number of elements of the airfoil ensemble.

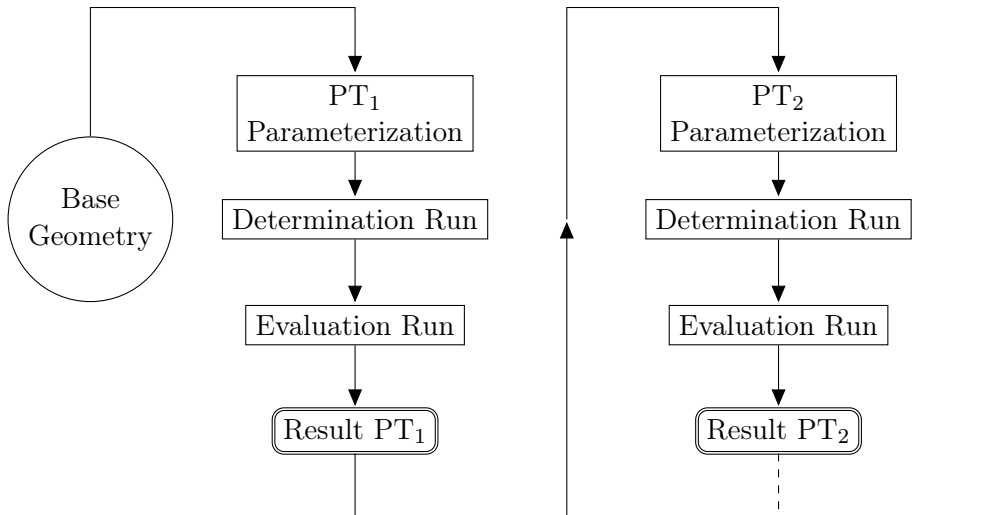


Figure 4.3: Each iteration of the optimization process is structured into three steps. After each iteration the number of geometric parameters used for the description of the airfoil shape is increased.

Parameterization

In the first step, the airfoil ensemble was parameterized using the geometric DOF of PT₁. Shape and positioning parameters for each element were determined based on x - y -data points from

airfoil dat-files. Initial values were defined manually, which were then optimized to describe the shape from the dat-file.

Both, the initial values of those parameters and the coordinates from the dat-file were then fitted with splines and divided into 100 equidistant segments⁴. This step was necessary to achieve point-wise uniform mapping, because (i) the number of data points in the dat-files varies, (ii) the density of data-points along the data-curve usually is not consistent. Otherwise, sections with higher point densities (namely LE and TE) would have been prioritized.

A cost function was defined which calculated the norm of the distance between each point $\chi_i \in X$, describing the desired shape and each point $\psi_i \in \Psi$ defined by the current airfoil parameters. The same CMA-ES algorithm which was used during the airfoil optimization process was used to minimize the sum of the norms for each element.

$$\min_{\psi} \sum_{i=1}^N \|(\chi_i - \psi_i)\|_2 \quad (4.4)$$

Determination Run

The first run for each configuration was conducted to evaluate the upper limit the lift coefficient C_L . During this determination run, the cost function⁵ was set to the negative sum of the lift coefficients at all four OPs.

$$f_{\text{cost}} = - \sum_{i=1}^4 C_{L,OPi} \quad (4.5)$$

Evaluation Run

The same airfoil configuration and PT was then used in a second run, the evaluation run. This time, the sum of the drag coefficients at all OPs were minimized above a threshold value for the lift coefficient $C_{L,\text{threshold}}$.

$$f_{\text{cost}} = \begin{cases} - \sum_{i=1}^4 C_{L,OPi} & \text{if } C_{L,OPi} < C_{L,\text{threshold}} \forall i \in [1, 2, 3, 4] \\ \sum_{i=1}^4 C_{D,OPi} & \text{if } C_{L,OPi} > C_{L,\text{threshold}} \forall i \in [1, 2, 3, 4] \end{cases} \quad (4.6)$$

The same threshold value $C_{L,\text{max}}$ was used for all OPs. It was determined by subtracting a buffer value b from the lowest⁶ of the maximum lift coefficients which were achieved during the determination run. Depending on how noisy the slope of the lift coefficients was, b ranged from 0.1–0.3.

$$C_{L,\text{threshold}} = \min_{i=1\dots4} (C_{L,\text{max},OPi}) - b \quad (4.7)$$

Increase in Degrees of Freedom

After the evaluation run the results were used as starting point for the next determination run. Before the run, the optimized shape was re-parameterized with an increased number of DOF.

⁴Function `interparc` from Matlab's file exchange (<https://de.mathworks.com/matlabcentral/fileexchange/34874-interparc>).

⁵The cost functions introduced in equations 4.5 and 4.6 are not the actual equations which were implemented in Matlab, but presented here with the intent to highlight the principles of the determination and evaluation run. The detailed equations are introduced in section 4.5.

⁶W.r.t OPs.

This way, each optimization with more DOF benefited from the optimum shape found in the preceding step with less parameters.

A total number of eight single- and four double-element airfoil shapes were determined. For each base geometry, single-element airfoils with PT₁ to PT₄, and double-element configurations with PT₁ & PT₂ were optimized.

4.3 Computational Framework

The optimization routine was implemented in Matlab. Multiple functions were used to setup a folder structure for the data files necessary for and created by the MSES programs, define computational options and initial parameter values, determine the cost of an airfoil parameter set, and evaluate it by using the evolutionary algorithm CMA-ES. The main functions of this process shall be introduced here, all of the functions which were used in the process and a list containing possible points of improvement can be found on the enclosed data disk.

Fig. 4.4 shows an overview of the Matlab framework. `runOptimization`⁷ is the superordinated initialization script which sets up a folder structure for the run data, loads the initial airfoil parameters as well as the user-defined boundaries, and sets the options for the `cmaes` optimization function [59]. The evolutionary algorithm then iteratively generates different parameter variations based on the CMA-ES theory introduced in sec. 2.5 and evaluates them based on the return value from the objective function `costFunctionForOptimization`.

The cost function is divided into four regions, evaluating the conformity to boundary values, the airfoil geometry which is generated based on the airfoil parameters, and the return values from the MSES/MSIS calls for either non-converged or converged calculations. As shown in fig. 4.4, the boundary values are checked first, before calling `evaluateWithMses`, into which the airfoil verification is embedded.

`evaluateWithMses` can be seen as the main script of the routine. After creating and verifying the airfoil, system calls are sent to the Linux operating system, as shown in fig. 4.4. If the geometry could not be verified, the cost is calculated according to Cost Region 3 and `evaluateWithMses` terminated early.

At first, MSET is called to initialize the grid and the flow-field around the airfoil based on previously defined grid generation parameters. At first, only the generated mesh is stored in an `mdat`-file which is then accessed by the flow solver and updated with the latest flow solution.

Next, the flow solver is called. A first, an inviscid solution is calculated to increase the chances of convergence. The flow solution is calculated either by MSES or MSIS. In MSIS the stream-wise entropy is conserved, which results in a faster and more robust calculation. It is used for inviscid cases with Ma Numbers below 0.02 and for viscous cases with Ma Numbers below 0.1, which was the case for OP₁ and OP₂. [60, p. 11, 26]

The flow solution is calculated in parallel by using Matlab's `parfor`-loop. For each of the for OPs a separate system call is sent to the system for the simultaneous execution of MSES/MSIS. The solution for each OP is therefore calculated on one processor core (see sec. 1.2), significantly improving the computational performance of the optimization process.

Also in parallel, MPLOT is called next. The program is used to read out the calculation results. For each converged OP the parameter values for C_L , C_D are determined and returned to the cost function.

Based on the values of success indicators for e.g. a non-verified airfoil geometry and the return values from the flow solver, the cost function calculates the cost of the airfoil configuration. All cost regions and their underlying functions are explained in detail in sec. 4.5.

⁷Names in typewriter font are Matlab functions or scripts (m-files).

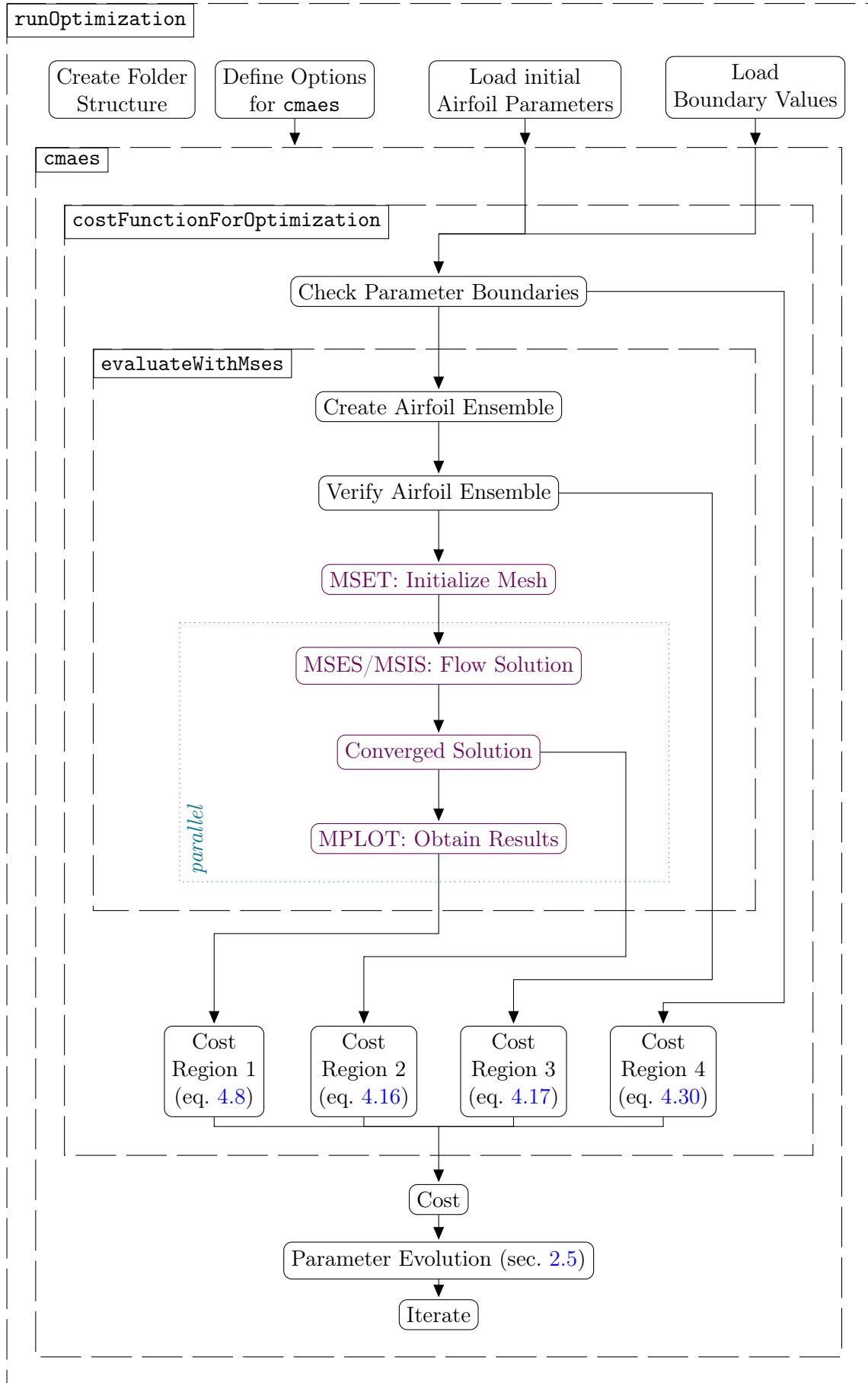


Figure 4.4: Overview of the Matlab function framework. System calls to Linux and commands executed in parallel are marked in color.

4.4 Meshing and Flow Solution

MSET generates the mesh around airfoil geometry based on an initial panel solution. Below and above each element, the stagnation streamlines are calculated. In combination with the upper and lower far-field streamlines the specified domain for the flow analysis is then divided into coarse blocks, based on which the grid is refined. The distance between nodes on the top and bottom surface of the airfoil is indirect proportional to the curvature of the surface. The resulting grid is structured along the stagnation streamlines and grid-lines perpendicular to the airfoil surface. [61, p. 21, 22]

Next, MSES was used to calculate the inviscid flow in the outer region by solving the steady Euler Equations. A strong coupling between the inviscid solution to the boundary layer and wake solution determined by the lag-dissipation method allows the handling of moderate flow separation and reattachment, which is common on multi-element airfoils. The onset of separation is estimated by the envelope method, which is based on the e^N -method. The coupling between the viscous and inviscid flow is implemented in form of the displacement thickness method. Flow separation cannot be fully captured, but (manually) detected due to the internal mesh adaptation capability of MSES which leads to increased streamline distances. [45, p. 684]

Various flow, grid, and computation options need to be defined prior to calling any of the programs. In this work, a semi-automated process was developed for the analysis of multiple airfoil geometries. To do so, compromises were made w.r.t. the tuning of these parameters. Surely, each individual case benefits from adjusted parameter setting, however, this results in increased setup and configuration time. Therefore, after finding initial values which expressed good convergence, these parameters were kept for the following investigations. The parameter settings of each run can be found on the data CD. A comprehensive list and explanations can be found in the MSES User Guide [60].

4.5 Cost Function

The cost function which was implemented for the optimization was not only used to assess the converged flow solutions in terms of lift and drag coefficients. During the optimization, various airfoil shapes were generated by the CMA-ES which (i) could not be converged by the flow solver, (ii) were outside the defined boundaries, or (iii) described invalid airfoil geometries. The cost function was designed in order to distinguish between these different regions and guide the algorithm towards convergence. The following subsections introduce each region, the way in which the corresponding cost was determined, and the means that were necessary to avoid overlapping of the cost values of the different regions.

4.5.1 Region 1: Solution Convergence

If the flow solver was able to converge, the cost was determined based on the value of the lift and drag coefficients. As long as not all of the lift coefficients $C_{L,OPi}$ were above the threshold value $C_{L,threshold}$ the cost was determined based on the sum of all lift coefficients. During the evaluation runs, the cost was determined based on the drag coefficients once the lift coefficient had reached the threshold value at every OP.

$$f_{\text{cost},R1} = \begin{cases} f_{\text{cost},R1a} = -\sum_{i=1}^4 C_{L,OPi} & \forall C_{L,OPi} < C_{L,threshold}, i \in [1, 2, 3, 4] \\ f_{\text{cost},R1b} = -100 + 100 \cdot \sum_{i=1}^4 C_{D,OPi} & \forall C_{L,OPi} > C_{L,threshold}, i \in [1, 2, 3, 4] \end{cases} \quad (4.8)$$

To guarantee that the costs $f_{\text{cost,R1a}}$ and $f_{\text{cost,R1b}}$ do not overlap, a value of 100 was subtracted from the latter. The sum of the drag coefficients was multiplied for more convenient post-processing and had no influence on the convergence behavior. The cost within Region 1 was therefor always within the following limits:

$$f_{\text{cost,R1}} \in]-100, 0[\quad (4.9)$$

4.5.2 Region 2: Divergence

If one or more OPs could not be converged by the flow solver, the cost value was determined according to the equations in this section. During the first optimization runs a quite simple function was used which returned the number of the unconverged OPs.

$$f_{\text{cost,R2}} = N_{\text{OP,diverged}} + p_{\text{rand}} \quad (4.10)$$

To avoid a totally flat topology a random number $p_{\text{rand}} \in [0, 1]$ was added. Even though that random number was added, the optimizer frequently stopped the process due to stagnation (e.g. during the viscosity analysis, sec. 5.1). Consequently, the cost function of Region 2 was further improved.

For each call to MSES/MSIS which does not lead to a converged flow solution, a number of convergence indicators are returned [61, p. 25, 26].

$p_1 = \text{d}R$	(density change)
$p_2 = \text{d}A$	(n.d.)
$p_3 = \text{d}V$	(viscous variables)
$p_4 = \text{d}sLE$	(n.d.)
$p_5 = \text{d}Gamma$	(circulation)
$p_6 = \text{d}C_{D,v}$	(viscous drag coefficient)
$p_7 = \text{d}Doubx$	(n.d.)
$p_8 = \text{d}Douby$	(n.d.)
$p_9 = \text{d}Scre$	(n.d.)
$p_{10} = \text{d}f_1$	(n.d.)
$p_{11} = \text{d}f_2$	(n.d.)
$p_{12} = \text{d}Alpha$	(angle of attack)

According to the MSES user guide, ‘convergence to plotting accuracy occurs when the changes drop to about 0.1×10^{-3} or so. If no separation is present, convergence to machine accuracy is achieved when the changes refuse to go down further with each iteration (about 0.1×10^{-5}). If significant separation is present, the final change magnitudes will be somewhat larger — about 0.1×10^{-4} or even 0.1×10^{-3} .’ [61, p. 26].

Of the available parameters, only the first nine were found to be practical with the setup used in this work. All others did not express any difference from converging to non-converging cases. The cost was determined by adding the absolute values of these nine parameters. The sign is of no importance for judging the convergence. By using the absolute value, cancellation of negative and positive values could be avoided.

$$f_{\text{cost,R2}} = \sum_{i=1}^9 |p_i| \quad (4.11)$$

For all cases which were examined during the setup of the cost function, the convergence indicators ranged within the following limits.

$$0 < |p_i| < |p_{i,\text{max}}| = 1 \cdot 10^{30} \quad (4.12)$$

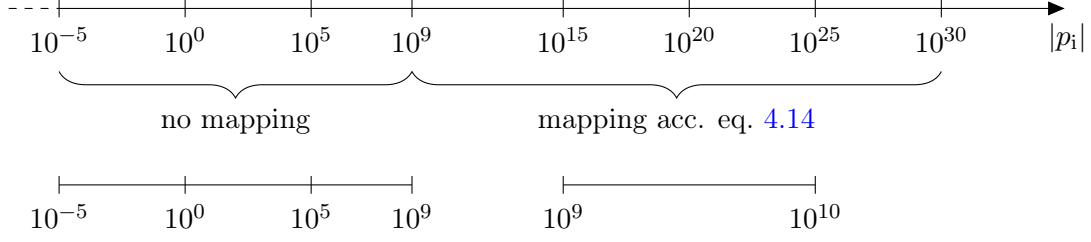


Figure 4.5: Mapping used for the cost function in region 2 which allows to have sufficient resolution of values close to the convergence threshold $\sim 1 \cdot 10^{-5}$ in combination with values around the upper limit of the convergence indicators $|p_{i,\max}|$.

However, the standard number format in Matlab are double precision floating point numbers with a precision of 16 digits [62]. This means, in order to represent changes just above the convergence threshold $\sim 1 \cdot 10^{-5}$ and have Matlab still recognize them, the exponent of any given number can have a maximum value of 10:

$$1 \cdot 10^{10} + 1 \cdot 10^{-5} = \underbrace{1.0000000000000001}_{16 \text{ digits}} \cdot 10^{10} \quad (4.13)$$

Consequently, the mapping shown in fig. 4.5 was incorporated within the cost function. It combined a logarithmic conversion, linear scaling, and a linear shift.

$$\tilde{p}_i = \begin{cases} |p_i| & \forall |p_i| < 10^9 \\ 1 \cdot 10^9 + \underbrace{\frac{9 \cdot 10^8}{30} \cdot \underbrace{\log_{10}(|p_i|)}_{\leq 30}}_{\leq 9 \cdot 10^8} & \forall |p_i| \geq 10^9 \end{cases} \quad (4.14)$$

Considering these implication, eq. 4.11 can be adjusted. The cost values within Region 2 can then be stated.

$$f_{\text{cost,R2}} = \sum_{i=1}^9 \tilde{p}_i \quad (4.15)$$

$$f_{\text{cost,R2,max}} = 9 \cdot 10^{10} \quad (4.16)$$

4.5.3 Region 3: Invalid Airfoil Geometry

Even though the generation of new airfoil parameters by the optimization algorithm was constrained by user-defined upper and lower limits, invalid airfoil geometries occurred. “Invalid” hereby describes three phenomena:

- Sharp turns (st): Bumps at the airfoil surface
- Intersections (in): Loops in the curve which cause the curve crossing itself
- Thin profile (tp): Violation of a thickness constraint around the TE

A cost function was defined for each phenomenon which contributed to the total cost in this region. The summand 10^{10} was added to avoid overlap with cost region 2. As explained in section 4.5.2, in this order, Matlab can still detect changes in the range of 10^{-5} which was more than sufficient for the detection of an invalid airfoil geometry as described in the following subsections.

$$f_{\text{cost,R3}} = f_{\text{cost,R2,max}} + f_{\text{cost,R3,st}} + f_{\text{cost,R3,in}} + f_{\text{cost,R3,tp}} \quad (4.17)$$

Sharp turns

Bumps on airfoil surfaces are generally not desirable. Drela found that only in cases with a single OP such sharp turns might be beneficial. However, drag power kites are operated within a continuous range of wind conditions [38], so no bumps are desired.

To detect sharp turns, the airfoil geometry was divided into 100 segments. For each node i in between two segments the curvature κ_i was calculated by fitting a circle with radius r_i through the node itself and its two neighboring nodes⁸.

$$\kappa_i = \frac{1}{r_i} \quad (4.18)$$

If the curvature κ_i fell below a critical value κ_{crit} , the difference to that value was registered. The sum of all registered deltas was defined as the cost due to sharp turns.

$$f_{\text{cost,R3,st}} = \sum_i \Delta\kappa_i = \sum_i \kappa_{\text{crit}} - \kappa_i \quad \forall i : \kappa_i < \kappa_{\text{crit}} \quad (4.19)$$

Through the examination of various, randomly generated invalid airfoil geometries the critical value was set to $\kappa_{\text{crit}} = 180$ (This value does not have the expected unit m^{-1} because it was defined in normalized coordinates). An upper limit for $f_{\text{cost,R3,st}}$ was estimated with (i) a maximum number of 10 sharp turns per element, (ii) a maximum number of four elements, and (iii) a maximum value of $\Delta\kappa_{i,\text{max}} = 1000$.

$$f_{\text{cost,3,st,max}} = 4 \cdot 10 \cdot 1000 = 40\,000 \quad (4.20)$$

Intersections

If an airfoil geometry cut itself, the meshing process will most likely not succeed and if it does, the flow solver is unlikely to converge. To avoid the computational overhead which would emerge during such attempts, the evaluation of the effected geometries is aborted beforehand. Two different kinds of intersections were differentiated: inner- and inter-elementary intersections. The latter occurs if an element intersects the slope of another element.

Each kind of intersection was quantified by an angle $\vartheta \in]0^\circ, 90^\circ[$. The cost $f_{\text{cost,R3,in}}$ was defined as the sum of all intersection angles found within an airfoil ensemble. Inner-elementary intersections were multiplied by a weighting factor of ten before adding the inter-elementary intersection angles. This scaling is based on the assumption that an airfoil which cuts itself is described by worse parameters than an element which cuts another element. Inter-elementary intersection can simply be resolved by shifting one of the elements, while the shape of the elements themselves are functional.

$$f_{\text{cost,R3,in}} = 10 \cdot \sum_{i=1}^{N_{i,\text{inner}}} \vartheta_{i,\text{inner}} + \sum_{i=1}^{N_{i,\text{inter}}} \vartheta_{i,\text{inter}} \quad (4.21)$$

The maximum value of the cost due to intersections was estimated by assuming a maximum number of ten inner-elementary intersections within each of the four elements. Inter-elementary intersections were assumed to only occur among neighboring elements⁹.

$$f_{\text{cost,R3,in,max}} = 10 \cdot 40 \cdot 90 + 30 \cdot 90 = 38\,700 \quad (4.22)$$

⁸Using function `fit_circle_through_3_points` from Matlab's file exchange (<https://de.mathworks.com/matlabcentral/fileexchange/57668-fit-circle-through-3-points>.)

⁹The unit $^\circ$ is neglected.

Thin profile

Many low Reynolds number airfoils have a thin profile towards the TE (e.g. S1210, CH10). For high lift applications with resulting high loads on the airfoil, like drag power kites, a minimal thickness is required to maintain shape during operation. Additionally, the airfoil design was constrained by the accuracy of the production method envisioned for the airfoils.

The upper and lower bounds for the TE-thickness t_{TE} were set to the same values for every airfoil configuration. The lower bound originated from the afore mentioned production method and was set to 1 mm. The upper limit was defined to 3 % of the chord length, following the recommendation from the MSES user manual [60, p. 4].

To minimize the computational resources necessary for the confirmation of a correct airfoil thickness, only the rear 40 % of each element were evaluated. The top and bottom surface within that span of any element were both discretized by 101 equidistant points. Each point on the top section was then checked against each point on the bottom section to determine whether their distance was smaller than the TE-thickness. This way a total of $N_{tp} = 101 \cdot 101 = 10\,201$ distances were checked for each element.

The amount by which the minimal value was undercut in meters Δt was then summed up and multiplied by 100 to determine the cost due to thickness violations¹⁰. The factor was generously chosen—violations in the order of 10^{-2} mm could still be detected with floating point precision.

$$f_{\text{cost,R3,tp}} = 100 \cdot \sum_{i=1}^{N_{tp}} \Delta t_i \quad \forall i : \Delta t_i < t_{TE} \quad (4.23)$$

The upper limit of eq. 4.23 for a four-element airfoil follows to:

$$f_{\text{cost,R3,tp,max}} = 100 \cdot 4 \cdot N_{tp} \cdot t_{TE,\text{max}} \quad (4.24)$$

$$= 400 \cdot 10\,201 \cdot 0.03 \cdot 0.167 \quad (4.25)$$

$$= 20\,442.8 \quad (4.26)$$

The introduced multiplication factors lead to the following upper cost limit in region 3.

$$f_{\text{cost,R3,max}} = f_{\text{cost,R2,max}} + f_{\text{cost,R3,st,max}} + f_{\text{cost,R3,in,max}} + f_{\text{cost,R3,tp,max}} \quad (4.27)$$

$$= 9 \cdot 10^{10} + 40\,000 + 38\,700 + 20\,442.8 \quad (4.28)$$

$$= 9.00000991428 \cdot 10^{10} \quad (4.29)$$

4.5.4 Region 4: Boundary Violation

Finally, the cost in region four can be defined. In this region at least one of the airfoil parameters x_i exceeded the predefined boundaries by Δx_i .

$$f_{\text{cost,R4}} = f_{\text{cost,R3,max}} + \sum_{i=1}^{N_{\text{param}}} \Delta x_i \quad (4.30)$$

Each boundary violation was measured relatively to the respective boundary value span from $x_{i,\text{min}}$ to $x_{i,\text{max}}$. By not using the 2-norm of the boundary violation itself but rather a percentage, all parameters—of various magnitudes—were accounted for in equal terms.

$$\forall x_i > x_{\text{max}} \quad \Delta x_i = \frac{x_i - x_{\text{max}}}{x_{\text{max}}} \quad (4.31)$$

$$\forall x_i < x_{\text{min}} \quad \Delta x_i = \frac{x_{\text{min}} - x_i}{x_{\text{min}}} \quad (4.32)$$

During configuration it was observed that sometimes infinity was returned. To avoid this, the cost was then set to a high random number $1 \cdot 10^{11} + p_{\text{rand}}$. This way, optimization abortion due to stagnation could be avoided.

¹⁰The unit m^{-1} is neglected.

Prior Sensitivity Analyses

Before the optimization process, two sensitivity analyses were conducted to find out whether the convergence probability was effected by different values for the kinematic viscosity and maximum number of Newton iterations during the call to MSES/MSIS. The sensitivity investigations in this chapter were conducted at the beginning of the work, with the 1st cost function definition for Region 2, given in eq. 4.10.

5.1 Viscosity

5.1.1 Setup

To analyze the sensitivity of the optimization process with CMAES and MSES due to viscosity changes, the same single-element airfoil (S1223, PT₁) was optimized at four different viscosity values which correspond to temperatures ranging from -20°C to 50°C (operating range of the kite system). These points—referred to as v_1 to v_4 —and the corresponding Reynolds numbers for each OP are listed in tab. 5.1. The optimizations were set to a maximum number of 4000 CMA-ES iterations and the cost function was adjusted to only optimize the lift coefficients of the airfoils.

The different viscosities were determined based on empiric findings from literature. For temperature values above 0°C , the empiric model from [63] was implemented. The viscosity at temperatures below 0°C was determined by linear interpolation of experimental data from [64]. To possibly include the viscosity calculations in the model from [21] several functions were written, provided on the data CD.

5.1.2 Analysis

The aerodynamic results of the viscosity runs are listed in tab. 5.2. Run v_1 was canceled by the optimizer due to stagnation, whereas the other three runs either finished because the maximum

Table 5.1: Values for the kinematic viscosity at the specific temperatures used in the viscosity sensitivity analysis. The temperature values are spread linearly over the operational range of the small-scale system. The Reynolds number for each OP was calculated with a chord length of $l_c = 0.167\text{ m}$. All values are at ambient pressure 101.325 kPa .

Configuration	T	ν	Re			
	[$^{\circ}\text{C}$]	[$10^{-4}\text{m}^2/\text{s}$]	OP ₁	OP ₂	OP ₃	OP ₄
initial	25	0.1549	$1.6176 \cdot 10^5$	$2.9764 \cdot 10^5$	$4.3351 \cdot 10^5$	$5.6939 \cdot 10^5$
v_1	-20	0.1173	$2.1355 \cdot 10^5$	$3.9294 \cdot 10^5$	$5.7233 \cdot 10^5$	$7.5171 \cdot 10^5$
v_2	3.33	0.1360	$1.8420 \cdot 10^5$	$3.3893 \cdot 10^5$	$4.9365 \cdot 10^5$	$6.4838 \cdot 10^5$
v_3	26.67	0.1563	$1.6026 \cdot 10^5$	$2.9488 \cdot 10^5$	$4.2950 \cdot 10^5$	$5.6411 \cdot 10^5$
v_4	50	0.1764	$1.4199 \cdot 10^5$	$2.6126 \cdot 10^5$	$3.8053 \cdot 10^5$	$4.9981 \cdot 10^5$

number of iterations was used or the changes in cost value fell below the threshold value. The total number of cost function evaluations of run v_1 was 1 756. All other runs were consequently trimmed to that length in the post-processing to assure that no advantages due to longer run-times influenced the results.

Table 5.2: Lift coefficients of the optimized airfoils from the viscosity runs. The cost was determined by $f_{\text{cost,R1a}}$ from eq. 4.8. The shares of all the different cost regions throughout the optimization show how effective the optimum was determined. The results only vary slightly in terms of cost value (i.e. lift coefficients).

	C_L				f_{cost}	Cost Region Share [%]				N_{conv}
	OP_1	OP_2	OP_3	OP_4		1	2	3	4	
v_1	2.196	2.097	2.081	2.090	-8.47	35.02	56.15	3.82	5.01	603
v_2	2.142	2.214	2.143	2.107	-8.61	43.85	45.10	8.54	2.51	770
v_3	2.088	2.130	2.095	2.066	-8.38	39.98	50.23	5.07	4.73	702
v_4	2.071	2.052	2.018	2.004	-8.14	37.19	55.41	3.13	4.27	646
σ	0.057	0.068	0.052	0.045	0.1975	3.81	5.14	2.41	1.12	72

For all four runs, the cost region shares (tab. 5.2) as well as the progression through the different cost regions (fig. 5.1) were very similar. In the beginning of each optimization, more parameter combinations which violated the boundaries or described invalid airfoil geometries were evaluated. Especially run v_1 expressed good convergence towards the end, where most of the parameter configurations converged. The relative evaluation position of the optimum of every run except run v_4 were between 85 % and 99 %. The early convergence of the last run has to be considered a “lucky guess”, as detailed examination of the run did not expose any inconsistencies.

No clear correlation between the number of converged calls to MSES N_{conv} and the cost value f_{cost} was apparent. The run with the most evaluations, v_2 , achieved the lowest cost value. However, no such direct proportionality between the lift coefficients and N_{conv} for the other runs is present.

Fig. 5.2 shows the airfoil geometries and the corresponding AOAs related to the cost values. Compared to the standard deviations of the lift coefficients, the differences in airfoil geometries seem to be more distinct which indicates a flat cost function topology. Runs v_4 and v_2 achieved improved aerodynamic properties with increased camber in combination with decreased AOAs. Higher AOAs could be linked to earlier separation, resulting in lower lift. That trend is contradicted by v_1 and v_3 , even though both runs resulted in very similar airfoil geometries and cost values.

Overall, the lift coefficients of all four runs did not differ greatly. The standard deviation of the lift coefficients for each OP has a maximum value of 0.068 at OP_2 . The lowest standard deviation occurred at OP_4 . The overall best solution was found for the range of Reynolds numbers at a temperature of 3.33 °C. Within this range, the most runs resulted in convergence.

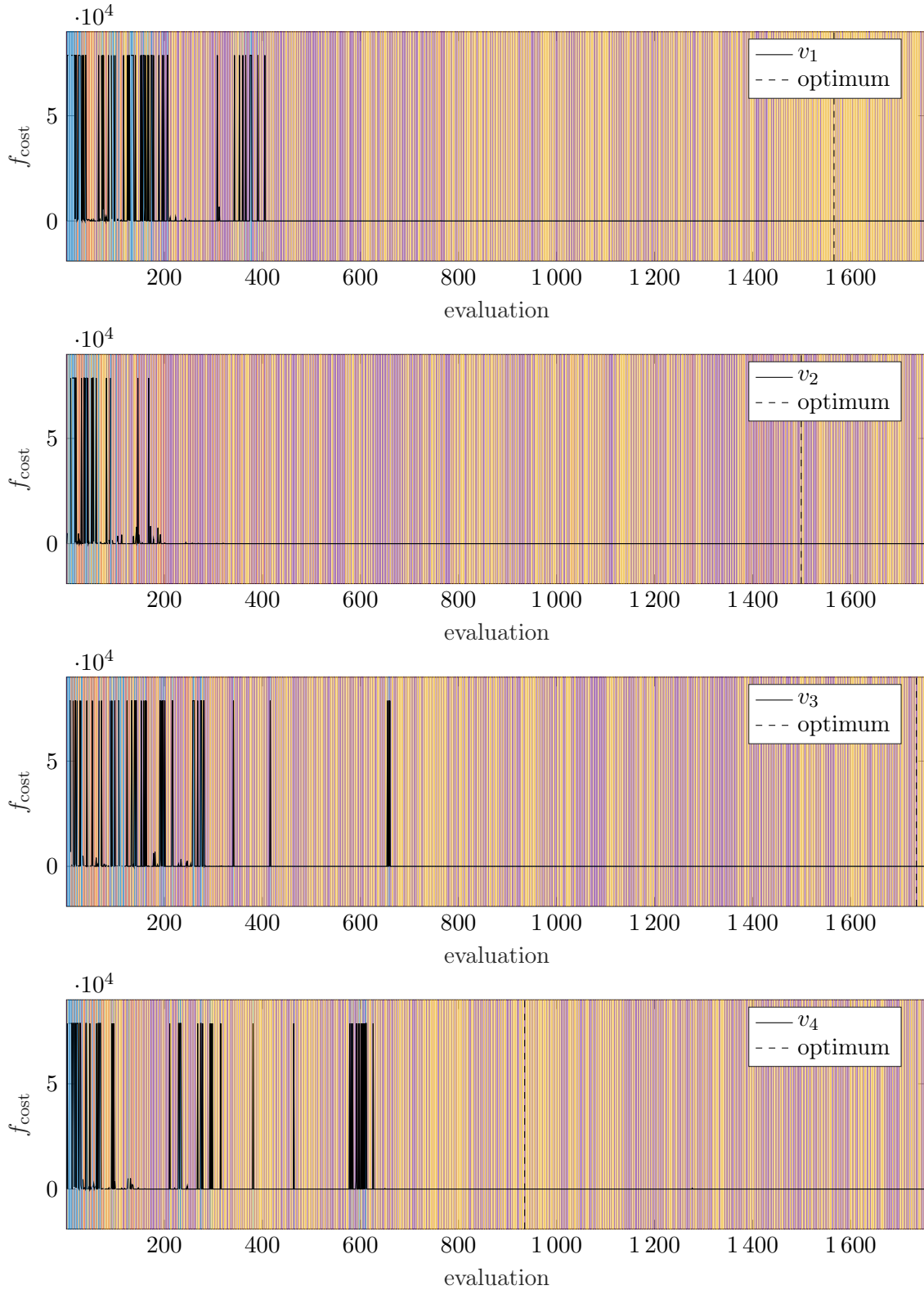


Figure 5.1: Development of the cost (—) and position of the optimum (----) of the viscosity runs v_1 to v_4 . The coloring of the background visualizes which region of the cost function was used to calculate the cost: Bounds exceeded ■, Invalid Geometry ■, Divergence ■, and Convergence ■. In the beginning, all runs exceeded the parameter boundaries or evaluated invalid airfoil geometries. Towards the end, the parameter combinations were only in cost regions one and two.

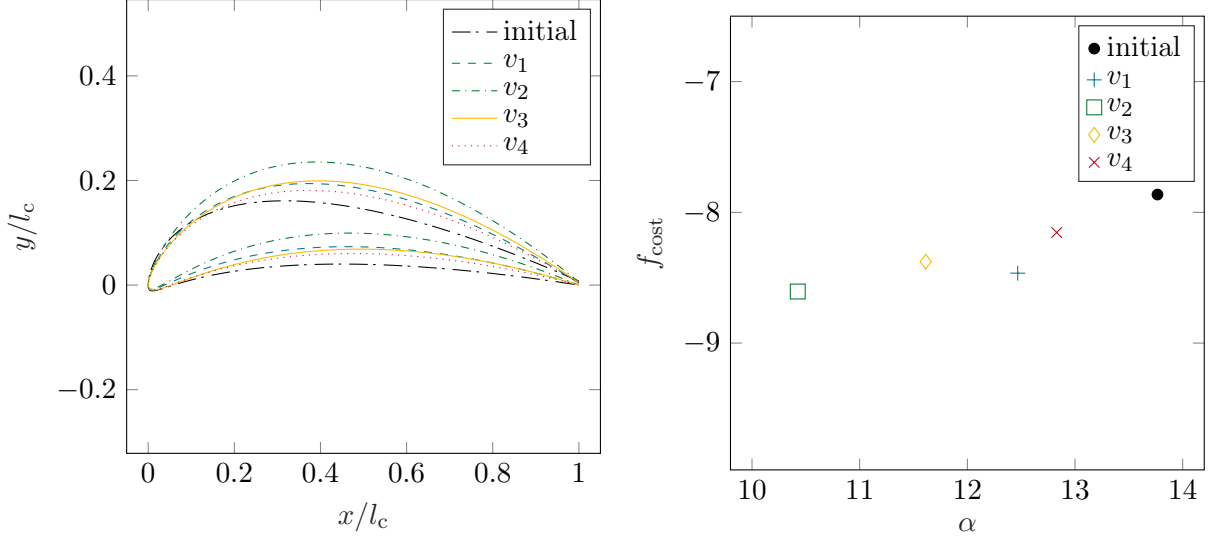


Figure 5.2: Optimized results from the viscosity sensitivity analysis. Higher camber values in the airfoil geometry (left) and smaller values for α correlate with lower cost values (i.e. higher lift coefficients). This might be due to the inability of MSES to properly predict separation.

5.2 Maximum Newton Iterations

5.2.1 Setup

In order to find a sufficient setting for the number of Newton iterations of the MSES flow solver, a similar investigation was conducted. Each time MSES is called, a maximum number of Newton iterations \hat{N}_{Newton} is prescribed. Then, three outcome scenarios are possible: (i) MSES converges within the allowed number of iterations, (ii) MSES does not converge before reaching \hat{N}_{Newton} , and (iii) the MSES call takes too long and is killed. For scenario (ii), two possibilities exist. First, the flow solution might converge with more iterations. In this case, increasing the number of Newton iterations would lead to higher convergence rates. Or second, that a certain number of iterations is sufficient to determine whether a flow case can be converged or not. This would mean that an increase in maximum Newton iterations does not lead to a higher convergence rates.

Similar to the viscosity sensitivity analysis, the basis for this investigation was a single-element airfoil (S1223, PT₁). Four different maximum iteration numbers \hat{N}_{Newton} were investigated, listed in table 5.3. For each run the CMA-ES optimization algorithm was limited to a maximum number of function evaluations N_{eval} of 1000.

Table 5.3: Overview of the iteration sensitivity analysis runs at four different values for \hat{N}_{Newton} . The cost was determined using $f_{\text{cost}, \text{R1a}}$ from eq. 4.8.

	\hat{N}_{Newton}	C_L				f_{cost}	Cost Region Share [%]				N_{conv}
		OP ₁	OP ₂	OP ₃	OP ₄		1	2	3	4	
i_1	250	1.953	1.937	1.903	1.892	-7.68	31.14	54.29	5.49	9.08	312
i_2	350	2.089	2.092	2.052	2.04	-8.27	38.42	49.70	5.89	5.99	382
i_3	450	1.989	2.01	1.973	1.958	-7.93	33.93	49.10	6.79	10.18	340
i_4	550	2.051	2.075	2.041	2.031	-8.20	47.70	40.12	6.69	5.49	478
σ		0.061	0.070	0.069	0.069	0.270	7.25	5.93	0.63	2.30	73

5.2.2 Analysis

The cost values of all four runs i_1 to i_4 were quite similar (tab. 5.3), the standard deviations of the lift coefficients small. The smallest standard deviation was found at OP_2 with a value of 0.070.

Increased values for \hat{N}_{Newton} resulted in lower unsuccessful rates: A maximum number of 250 in run i_1 led to a share of cost region 2 of around 52 %, whereas in run i_4 only around 40 % of MSES calls were unsuccessful. The share of successful MSES evaluations (Region 1) increased from i_1 to run i_2 and from run i_3 to run i_4 , respectively. Compared to run i_2 , the share of Region 1 of run i_3 was smaller. This is correlated to an increase in parameter evaluations which violated the boundaries (Region 4), indicated by the coloring around evaluations 500, 700, and 800 in fig. 5.4. Compared to the other three runs, the share of Region 4 of run i_3 was rather big with 10.18 %.

Fig. 5.3 shows the composition of all cost Region 2 shares. As mentioned above, a call to MSES can be unsuccessful either because no flow solution was found, or because the maximum number of Newton iterations was reached. The amount of MSES calls which were aborted due to reaching the maximum number of Newton iterations dropped by 21.80 % after increasing \hat{N}_{Newton} from 250 to 350. A further increase in maximum Newton iterations did not have such a significant effect. Based on these observations, the maximum number of Newton iteration for single-element airfoils was set to 350 for all subsequent optimizations.

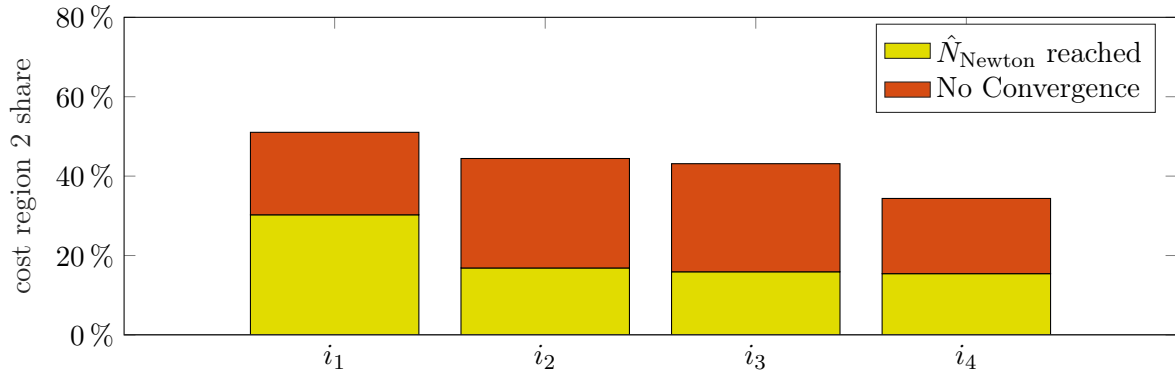


Figure 5.3: The amount of MSES calls which were aborted due to reaching the maximum Newton iteration decreases significantly from run i_1 to run i_2 . After that, no significant decrease is noticeable.

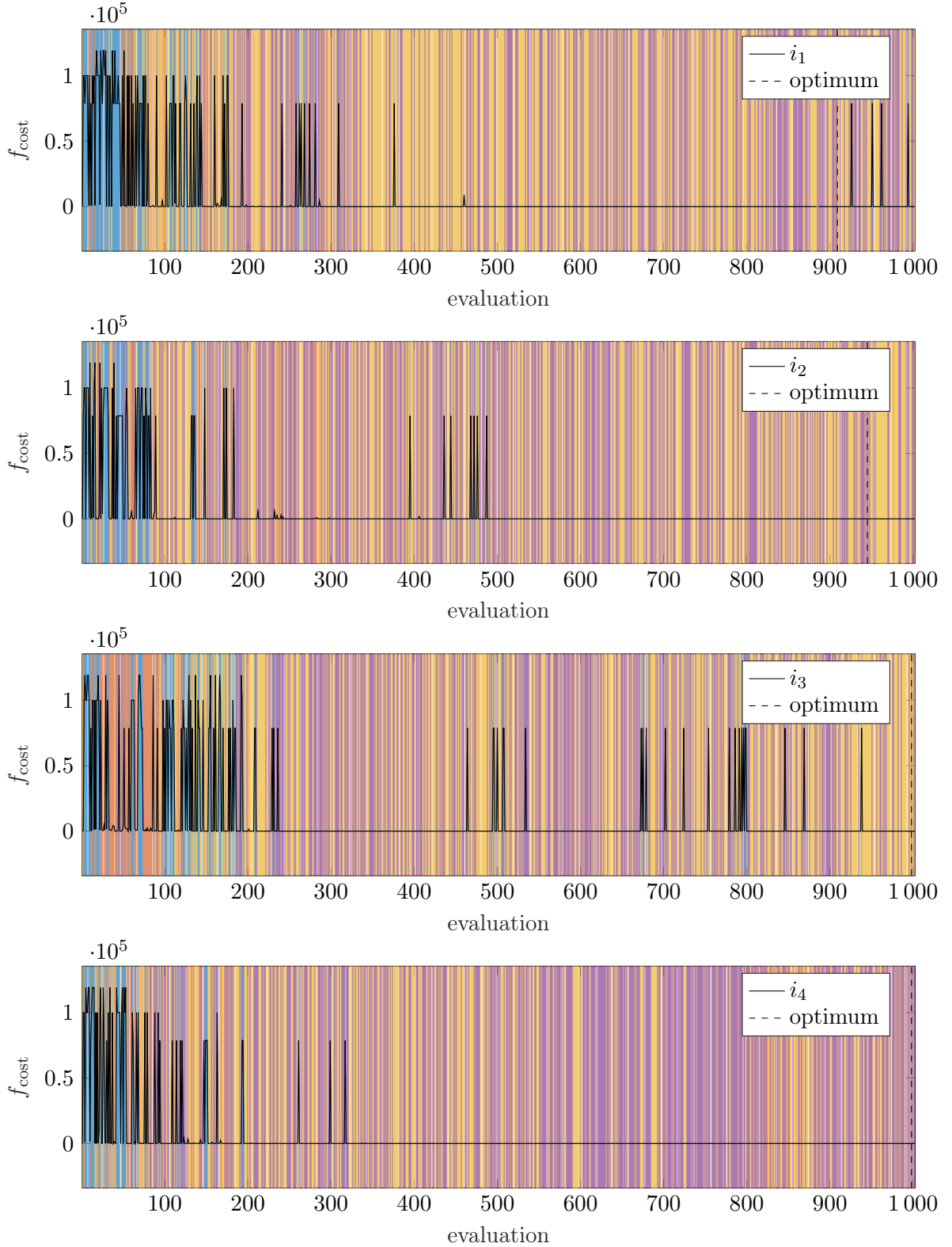


Figure 5.4: Cost (—) and position of optimum (---) of runs i_1 to i_4 . The coloring of the background visualizes which region of the cost function was used to calculate the cost: ■ Bounds exceeded, ■ Invalid Geometry, ■ Divergence, and ■ Convergence. The increased share of boundary violations for run i_3 is indicated by blue background ■ around evaluations 500, 700, and 800.

Optimization Strategy Evaluation

This chapter presents the results from the optimization and reviews the success of the optimization strategy. Lift and drag coefficients of different PT are compared against each other, exemplary effects of the cost development are given. The robustness of the different optimized airfoil design is analyzed by means of polar plots. Lastly, the functionality of the cost function is evaluated.

6.1 Development of Lift Coefficients

Fig. 6.1 shows the parameter values for the lift coefficients determined by MSES/MSIS. It can be seen from figs. 6.1a and 6.1b that an increase in geometric DOF from PT₁ to PT₄ did not always result in improved aerodynamic performance. This is due to the fact, that the determination runs for PT₄ of base geometry 1223, and for PT₂ and PT₄ of base geometry 15th did not result in higher lift values than the preceding evaluation runs. All C_L threshold values are given in tab. 6.1.

Table 6.1: List of all C_L threshold values which were determined during the determination runs. Some of the values are below the values which were reached by the preceding run with less DOF.

Base Geometry	Elements	PT ₁	PT ₂	PT ₃	PT ₄
1223	1	1.8	2.0	2.1	1.9
	2	2.4	3.2	-	-
15th	1	1.9	1.9	2.1	2.0
	2	3.1	3.0	-	-

Different causes were identified for this observation. Fig. 6.2a compares the initial configuration and the first converged airfoil for the determination run of PT₄ of the 1223 series. While the initial shape looks like a common airfoil, the first converged geometry is shaped in a rather unusual way. Over the course of the run, the concave feature at the bottom side of the airfoil shifted towards the back. The final shape seems to be an artifact of the shape found in the beginning of the run which was not detected by the airfoil verification function.

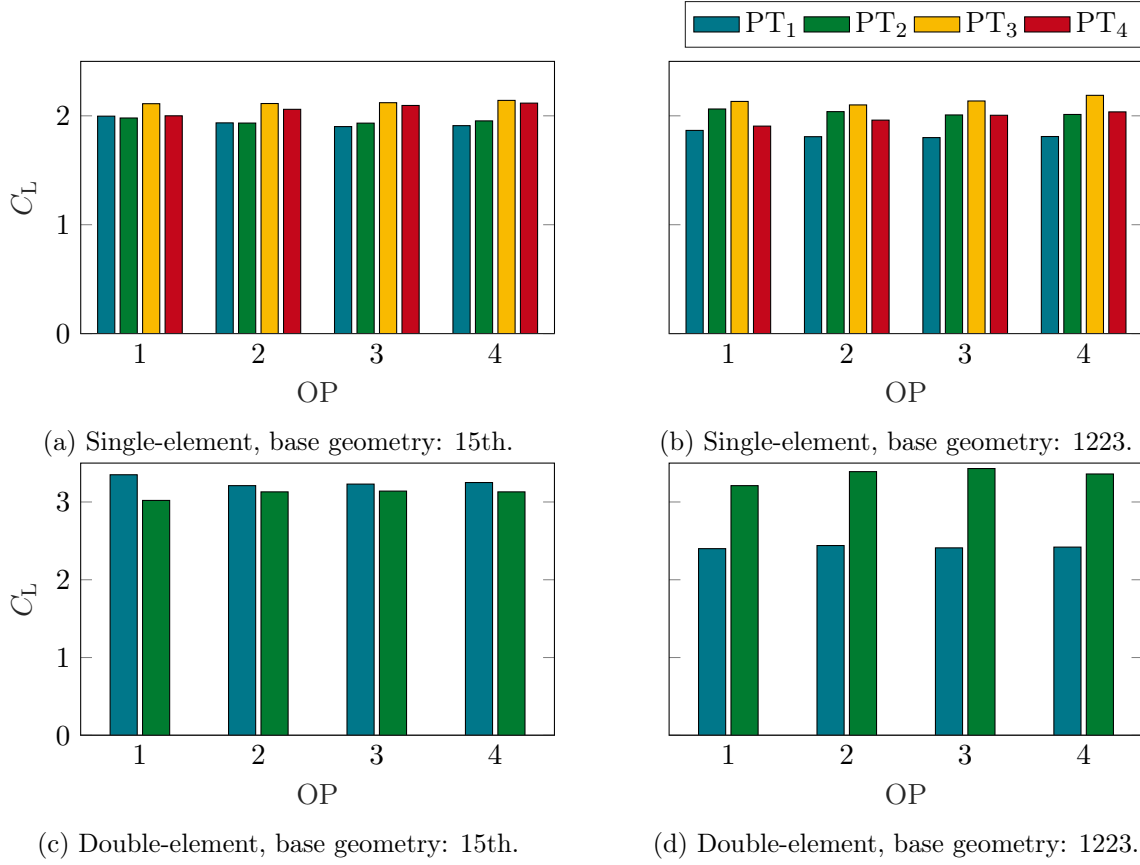


Figure 6.1: Optimized lift coefficients of the evaluation runs for the single- and double element configurations.

Fig. 6.2b shows a section of the lift coefficient slopes for the determination run. The value of C_L for OP₁ is unstable, varying between 1.6 and 2.1. This is most likely linked to the onset of separation at which MSES/MSIS was not able to converge anymore. This observation is consistent with the activated cost regions shown in fig. 6.2c: The airfoil parameters generated by CMA-ES were either evaluated within Region 1 or 2. Because parameter changes led to higher costs in Region 2, the solver got stuck on the airfoil shape shown in fig. 6.2a. The same behavior was present for the determination run for PT₄ of the 15th series.

The determination run of PT₂ expressed a different behavior: The increase in lift coefficients stagnated at values just above 1.9. The reason cannot be found in the detection of many invalid airfoil geometries. Only seven invalid geometries were detected compared to 5795 valid airfoil shapes. Apparently, all surrounding parameter combinations within the CMA-ES initialization region led to higher cost values due to evaluation within cost Region 2.

The threshold value of the lift coefficient for the evaluation run of the double-element 15th, PT₂ configuration was also lower compared to the previous value for PT₁ (tab. 6.1). The cost development of the converged airfoils for this configuration is shown for PT₁ and PT₂ in fig. 6.3. The run with PT₂ does not show an asymptotic approach towards a tableau as distinct as the run with PT₁ due to a shorter run-time. The run was aborted early by CMA-ES due to stagnation.

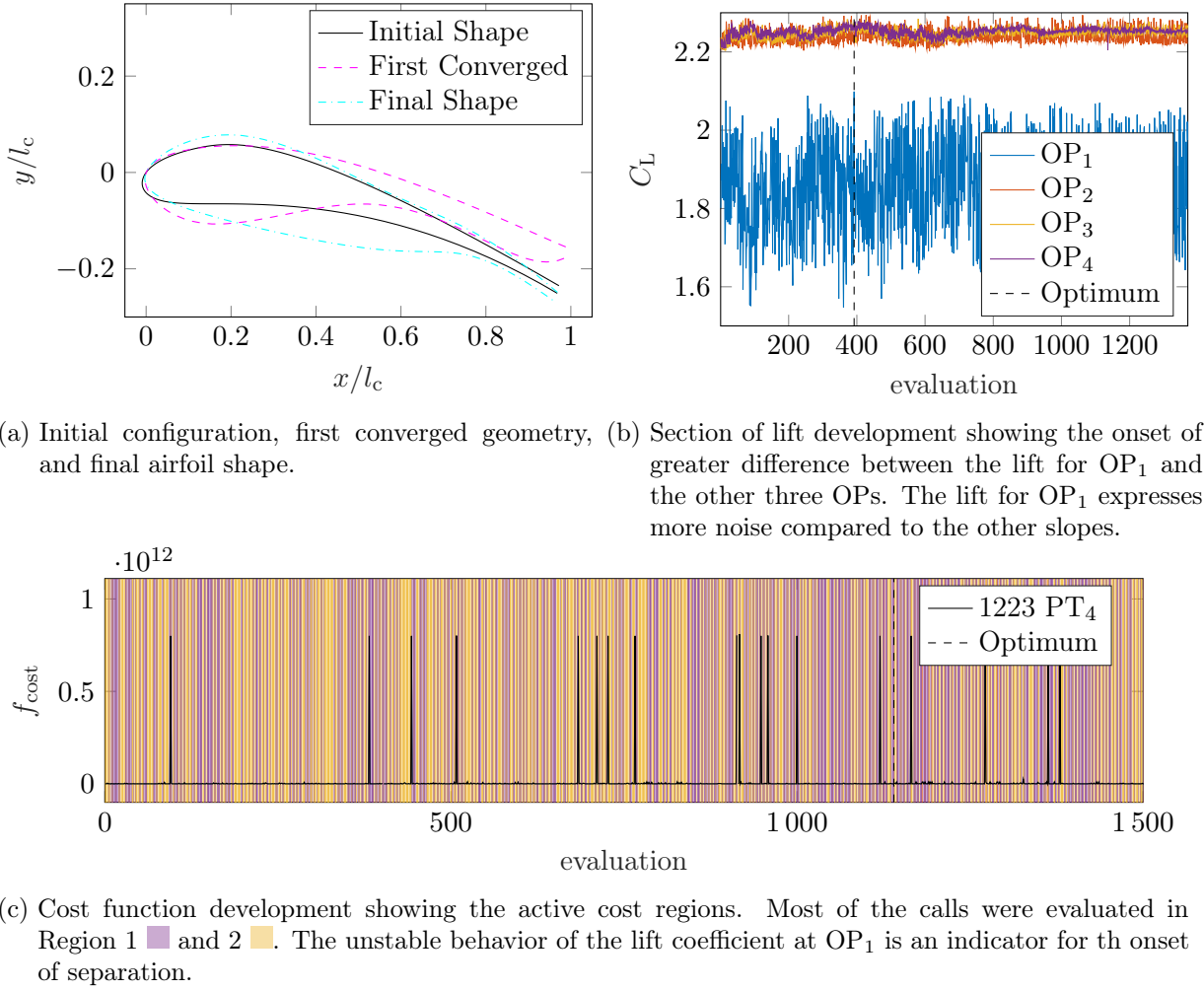


Figure 6.2: Development of airfoil shape, lift coefficients and cost for the determination run for PT_4 of base geometry 1223.

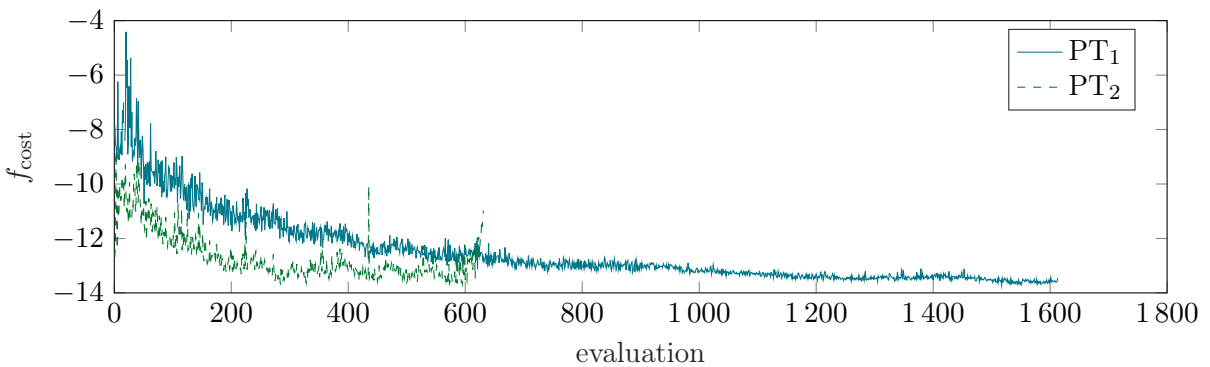


Figure 6.3: Comparison of the cost development for the double-element configuration of the 15th base geometry. Within just over 1600 evaluations, the the cost of PT_1 stabilized around -13.4. The optimization with PT_2 did not run long enough to form such a plateau of stabilized cost values. This is due to a shorter overall run-time compared to the run with PT_1 .

6.2 Pitch Robustness

After the optimizations were completed, a pitch robustness analysis was conducted for all optimized airfoils. The AOA of each configuration was altered within a range of $\pm 5^\circ$ around the found optimum. The analysis was done by using MPOLAR and MPOLIS to generate polars for OP₃ and OP₄, and OP₁ and OP₂, respectively. An exemplary explanation of the significant characteristics is presented in this section, the complete set of all polars can be found in the appendix C.

6.2.1 Convergence

The polar data was generated by calculating the flow at the optimum value of the AOA α_{opt} and then by gradually decreasing α by 5° . Once the lower bound was reached, the AOA was gradually increased again until reaching 5° . For each step, the previously converged solution was used as an initiator for the flow calculation.

During the process, the angular step size was varied between 0.001 and 0.5 to achieve convergence. Sometimes, a refined step size was helpful in generating the polars. Smaller differences in α lead to less differences between the flow solutions of the different steps. Previous solutions can thus be better used as starting points for the next convergence. Other times, an increased step size led to convergence. In such cases, the flow solver had difficulties to calculate the flow at a specific pitch. By changing the AOA by a relatively large increment, these problematic areas were stepped over, resulting in convergence again at the next configuration. These observations stand in contrast to the directive given in [60, p. 27], which recommends the usage of small increments for a more robust sweep.

However, in some cases, not even the airfoils which were determined during the optimization process converged:

- Single-element 15th, PT₄ at OP₁ $\forall \alpha \in]\alpha_{\text{opt}}, \alpha_{\text{opt}} + 5^\circ]$
- Single-element 1223, PT₂ at OP₁ $\forall \alpha \in]\alpha_{\text{opt}} - 5^\circ, \alpha_{\text{opt}} + 5^\circ]$
- Double-element 15th, PT₁ at OP₄ $\forall \alpha \in]\alpha_{\text{opt}} - 5^\circ, \alpha_{\text{opt}}]$

6.2.2 Repeatability

The lift coefficients which were determined during the optimization process (fig. 6.1) often do not coincide with the values which were estimated during the calculation of the polars. The following significant deviations were registered, which are probably linked to the observations described in sec. 6.2.3.

- Single-element 1223, PT₁ & PT₂: Polar values below values from optimization
- Single-element 1223, PT₃: Polar values at OP₄ above values from optimization
- Double-element 15th, PT₁: Polar values below values from optimization, especially at OPs with lower apparent airspeed
- Double-element 1223, PT₁: Polar values below values from optimization, especially at OPs with higher apparent airspeeds
- Double-element 1223, PT₂: Polar values above values from optimization for OPs with higher apparent airspeeds

6.2.3 Curvature Shape

In most C_L - α polars a curved or jagged slope was generated, as shown in fig. 6.5a. The effect is more severe at lower apparent airspeeds, but is present at all OPs. The effect can also be seen in fig. 6.5b. With increasing AOA, the drag coefficient rises in steps of varying size. This effect is also most significant for lower apparent airspeeds. Both effects were present in other polars as well, all of which are given in the appendix C.

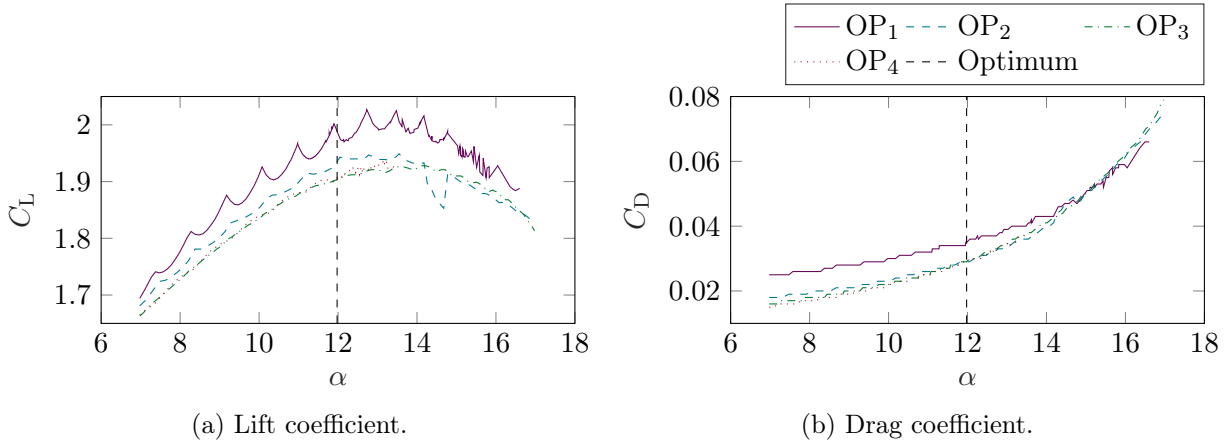


Figure 6.4: Values of the lift and drag coefficient at different AOA for the single-element configuration 15th, PT₁. The slope of the lift coefficient expressed a curvy slope, the drag coefficient a slope similar to stairs. Both features can also be seen in the dependent plots, e.g. the glide ratio.

According to the MSES user manual [60, p. 44], such appearance is linked to insufficient resolution of laminar separation bubbles. For most configurations, the default mesh resolution in stream-wise direction with 80 nodes on the airfoil surface is sufficient. For airfoil configurations which are prone to laminar separation, an increase is suggested. This is the case especially for configurations at low Re numbers and separation close to the LE. All optimization runs (sec. 6.1), as well as all polars (app. C) were initialized with the default number of side points. The automatic mesh refinement embedded in MSES then increased the number to 181 during the calculation process. However, the problem still remained even after increasing the number of airfoil side-points to 500, as shown in fig. 6.5.

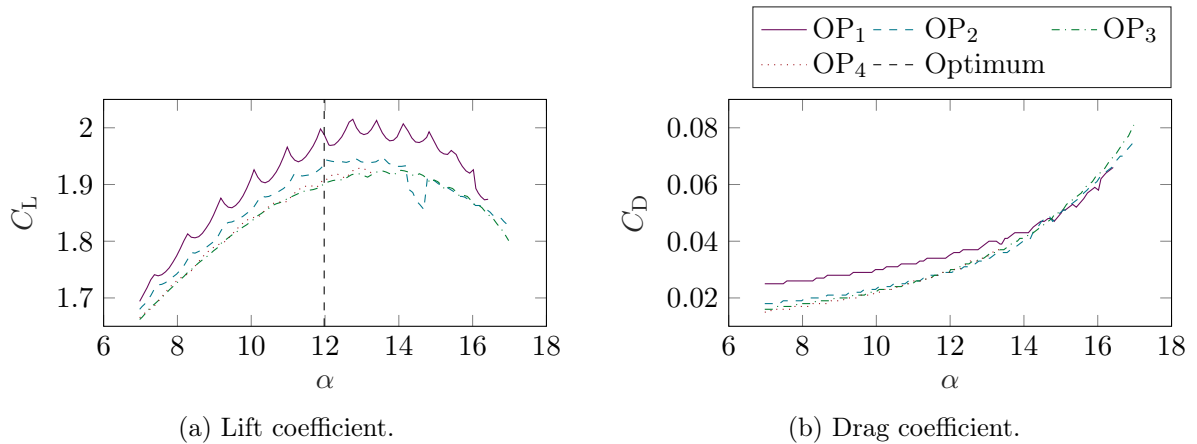


Figure 6.5: Even after increasing the number of airfoil side points during the meshing process in MSET to 500, the ragged shape remains.

6.2.4 Positions of Optima

Finally, by keeping in mind the bespoke problems of convergence, repeatability, and curvature shapes, the optimized AOA α_{opt} can be assessed in terms of lift coefficient development. During the determination run of each configuration, an optimum value for the lift coefficients at all OPs was found. This point is the maximum of the lift slopes in fig. 6.6a, which is located at about 20° .

During the next run, the evaluation run, the lift was only maximized until reaching the determined threshold value $C_{L,\text{threshold}}$. Once the threshold value was reached the drag was minimized, shifting the position of the optimum solution (---- in fig. 6.6b) to lower AOA. Both, the slopes of drag and lift coefficient, lead to the hypothesis that mostly the lift-induced drag was minimized by reducing the AOA.

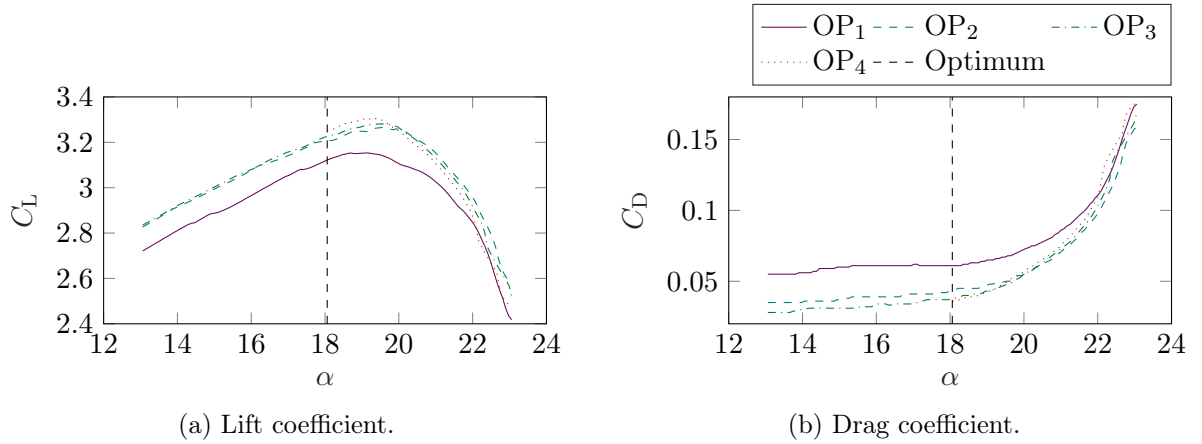


Figure 6.6: Slope of the lift coefficient for the double-element airfoil 15th, PT₁. The optimum result from the evaluation run is located just left of the maximum of the lift coefficient slope. The shift of the optimum towards lower values of α is due to the reduction of the lift-induced drag by lowering the airfoil pitch.

Due to the shift of the optimum to lower values of α during the drag minimization, a negative change in pitch resulted in greater C_L decrease compared to a positive change. If the pitch is increased, the lift coefficients increase at first, until the maximum of the lift coefficient slope is reached, after which they decrease again.

6.3 Cost Function Region Shares

To investigate whether the refinement of the cost function in Region 2 had beneficial effects on the convergence behavior, all runs which were calculated with the configuration from eq. 4.10 were compared with all runs which were optimized by using the refined function of eq. 4.16. In the following, the former is referred to as first configuration, the latter as second cost function configuration.

At first, the different PTs were compared against each other for single- and for double-element airfoils. Tab. 6.2 lists the number of runs which were analyzed. Fig. 6.7 shows the mean values of the cost region shares for the declared configurations. The error bars above and below each point indicate the highest and lowest value in that region, respectively.

The single airfoil configurations of PT₁, PT₂, and PT₃ which were calculated with the first cost function configuration are shown in fig. 6.7a. The parameterization with the least DOF, PT₁, had the highest convergence rate and the second highest (or lowest) divergence rate. Neither is a correlation between the amount of geometric DOF and the tendency of converge visible in figs. 6.7b, 6.7c, or 6.7d. This conclusion is assumed true in the following.

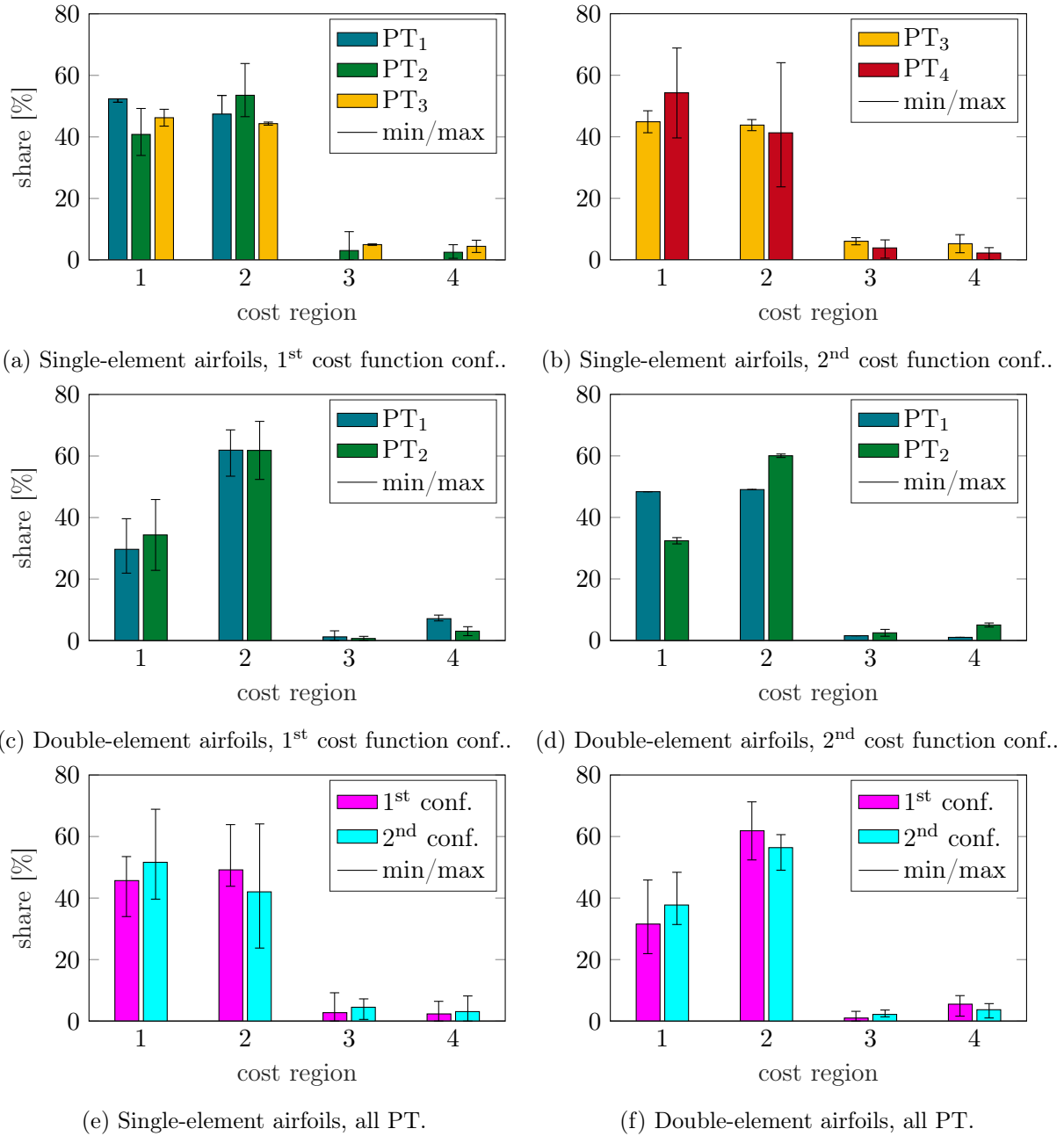


Figure 6.7: Mean cost region shares are indicated by colored bars, the minimum and maximum values for each configuration run in black error bars. If no error bars are plotted, the bar shows data of only one run. Figs. (a)–(d) compare the different parameterization types against each other: PT_1 , PT_2 , PT_3 , and PT_4 . No correlation between the cost region shares and the parameterization type is present. Figs. (e) & (f) restructure the same data for comparison of the 1st and 2nd cost function configuration for Region 2. A clear shift of shares from Region 2 to Region 1 is visible: The 2nd cost function configuration leads to higher convergence and lower divergence rates in MSES/MSIS.

Table 6.2: For the different airfoil configurations, different number of runs were available for comparison. Double-element airfoils with PT₃ and PT₄ were not optimized in this work.

Cost Function Configuration	Single-Element				Double-Element			
	PT ₁	PT ₂	PT ₃	PT ₄	PT ₁	PT ₂	PT ₃	PT ₄
1 st	2	3	2	0	3	2	0	0
2 nd	0	0	2	5	1	2	0	0

Figs. 6.7e and 6.7f compare the new cost function configuration against the old one. Each figure includes all runs—no matter the parameterization type—of the single- and double-element airfoils, respectively. The updated cost function for Region 2 shows a clear improvement compared to the first configuration: For both, single- and double-element airfoils, more calls to MSES/MSIS resulted in convergence (increase in share of Region 1) and less calls in divergence (decrease in share of Region 2). However, this only holds true for the mean values of the cost region shares. Especially for the single-element airfoils (fig. 6.7e), the difference to the minimum and maximum values (indicated by the error bars) are significant.

The difficulties of the flow solver to converge multi-element airfoil configurations is clearly visible in figs. 6.7e and 6.7f. For single-element airfoils the share of converged calls to MSES/MSIS is similar to the fraction of unsuccessful calculations. Compared to that, the likelihood of convergence of double-element airfoils is already 14 % lower. For triple-element airfoils the amount of converged calculations even dropped down to zero.

The shares of Region 3 (invalid airfoil geometry) and 4 (boundary violations), both are significantly lower than the shares of the other regions. As expected, the cost function implementations in eqs. 4.17 and 4.30, respectively, guided the CMA-ES algorithm sufficiently. This is also visible in figs. 5.4 and 5.4, where only in the beginning of each optimization Region 3 and 4 are active.

Computational Fluid Dynamic Verification

The airfoil designs which were obtained from the optimization routine were verified using ANSYS software. This chapter gives an overview of the programs used, the steps of the workflow, and information about the settings and models that were utilized. For each optimized airfoil design, a simulation is run to estimate lift and drag. The values of the aerodynamic coefficients are compared to those determined by MSES/MSIS and assessed w.r.t. observations gained from the CFD results.

7.1 Setup

7.1.1 Workflow

The workflow for the CFD post-analysis of the optimized airfoils was implemented using ICEM CFD for the meshing process and ANSYS CFX for the computation of the flow solution as well as its post-processing. This way, full advantage could be taken from the scripting symbiosis of both programs.

Based on findings from [8], ICEM CFD replay files were used for the semi-automated mesh generation. Replay files are written in Tool Command Language (TCL) with the extension toolkit Tk. ICEM-specific commands enable the programmatic translation of graphical user interface (GUI)-based user actions. This way, the meshing process can be accelerated for similar flow cases with slightly different airfoil geometries. After generation, each mesh was reviewed for any discrepancies (e.g. wrong positioned nodes, sec. 7.1.3).

Next, ANSYS CFX-Pre, -Solve, and -Post were used to read in the mesh and define the boundary conditions, calculate the flow solution, and generate the output parameters, respectively. All actions were defined in Workbench journaling files, which represent—similar to ICEM CFD replay files—GUI commands which would otherwise have to be repeated manually for each airfoil configuration.

7.1.2 Turbulence Model

The flow solution was calculated with the $k-\omega$ turbulence model which is based on the RANS-equations. It solves two transport equations, one for the turbulence kinetic energy and one for the turbulence frequency. The stress tensor is calculated by means of the eddy-viscosity concept [65]. Compared to the $k-\epsilon$ model it is able to predict the onset of separation more accurately. Additionally, it is more robust and exact at near wall modeling for low Reynolds while expressing better convergence capabilities [66]. For these reasons and the good applicability to parametric investigations¹ (cf. [8, p. 70]), the model was chosen for the CFD simulations in this work.

¹No interference is necessary during the simulation.

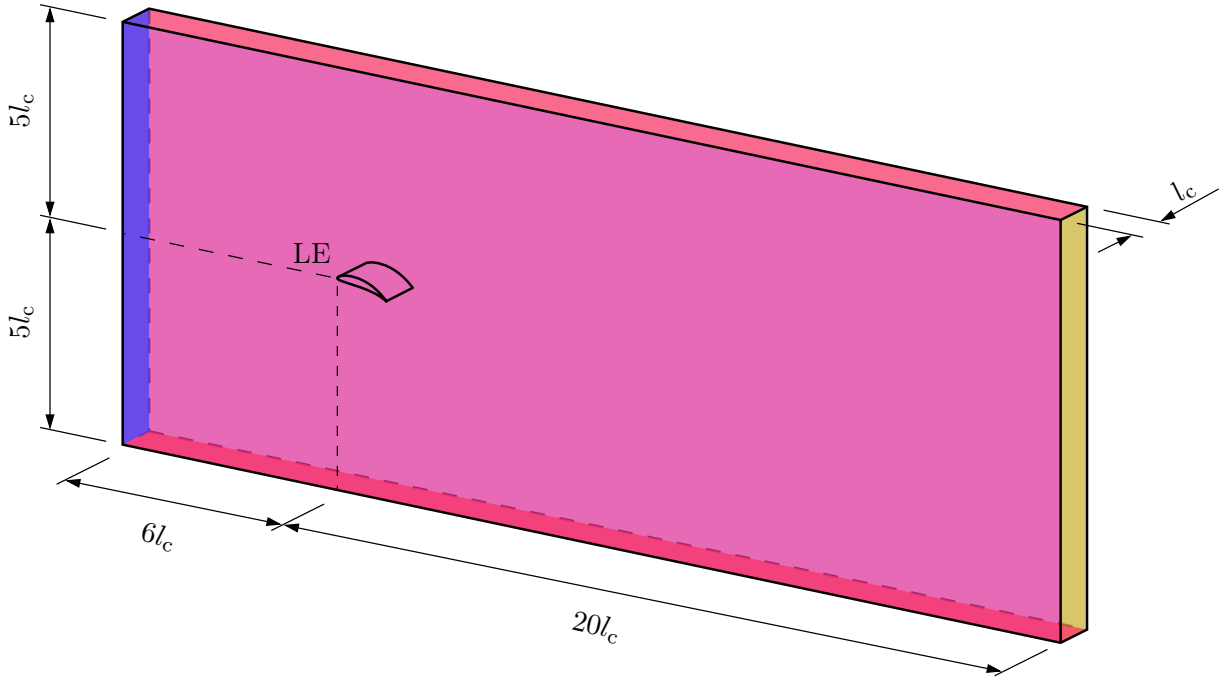


Figure 7.1: The simulated flow domain for the CFD analysis is confined by the inlet ■, the outlet ■, the top and bottom planes ■, and the symmetry planes ■. All of the dimensions were set to values from [8] besides the distance from the LE to the outlet plane which was increased to avoid back-flow.

7.1.3 Mesh

The simulated domain was sized according to the chord length of $l_c = 0.167$ m and conclusions from [8]. Fig. 7.1 visualizes how far the confining inlet, outlet, top and bottom, and front and back planes are positioned from the LE of the airfoil.

The recommended distance of $15l_c$ between outlet plane and LE had to be increased to $20l_c$ after first simulations were aborted by the solver due to reverse flow errors. Low pressure regions towards the domain outlet can cause a the fluid to flow back into the domain. The ANSYS flow solver tries to counteract this, by closing off the corresponding sections of the outlet plane, which can deteriorate the simulation results.

To fully resolve the turbulent wake behind the airfoil, the span-wise domain width was set to $1l_c$. This way, turbulence effects can be captured correctly [8, p. 58, 70]. The inflow was set to velocities according to the four OP (cf. . sec. 4.2.1), normal to the inlet surface in direction of the x -axis. The air was set to standard conditions (cf. . tab. 4.2). The turbulence intensity was set to 5% with an Eddy Viscosity Ratio of 10. These settings represent the conditions at the wind tunnel at the TUM.

A symmetry boundary condition was implemented at the front and back planes. In ANSYS, fluids adjacent to symmetry planes are restricted to flow parallel to the plane. Fluid particles which are moving towards the symmetry plane are reflected back into the domain by inverting the normal velocity component v_{\perp} . This effectively leads to mirrored deflection of the fluid at the symmetry planes. Additionally, the gradients of all scalar variables (e.g. pressure p) perpendicular to the surfaces are set to zero as well [67]. The top and bottom boundaries were modeled with free-slip, the airfoil surface with no-slip conditions.

Not the whole flow domain could be meshed with a high density of nodes due to limitations of the ANSYS student license (cf. sec. 1.3), which only allows a maximum number of 512k nodes. The highest density of the unstructured mesh was set on the surface of the airfoils. The surrounding volume was discretized by with medium mesh resolution. The size of the elements

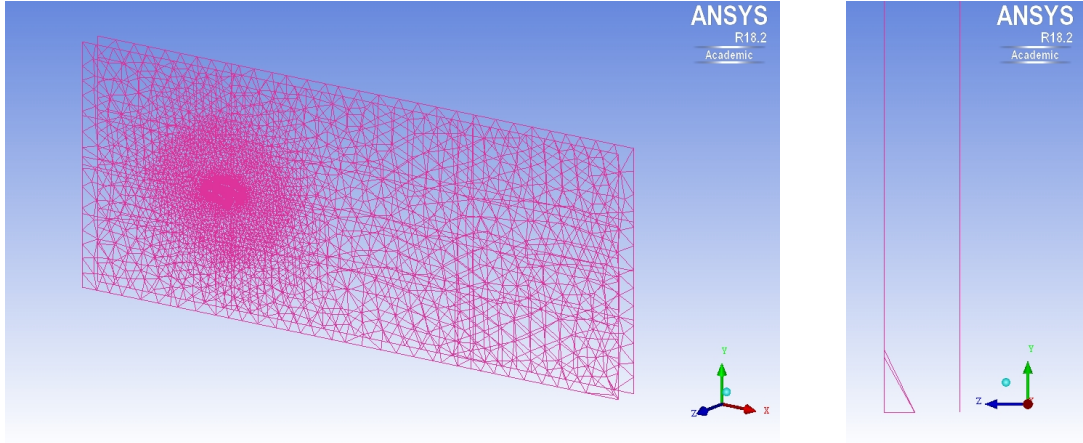


Figure 7.2: Node displacement error during the automated meshing routine. The screenshot on the left shows the symmetry planes of the whole mesh. On the right, a detailed view reveals the outlier node. Posterior manual repositioning of the node is necessary. Images used by courtesy of ANSYS, Inc..

adjacent to the surface was regulated by an exponential growth law according to [68]. The outer flow region—with low turbulence expectations—was discretized with bigger elements.

The $k\text{-}\omega$ model requires meshes with y^+ -values below 2, but above 0.001 [65, 69]. Hence, different initial prism heights were chosen for the different OPs to guarantee appropriate values. Similar investigations by [8] suggested a value below 5, whereas in literature a value of around 1 was found to be the most common [70, 44, 71, 72]. The highest values were found at the LE, strongly diminishing towards the TE. For all simulations, the average mean y^+ -value on the airfoil surfaces was around 0.3317, the maximum value around 1. An overview of all y^+ -values and the corresponding initial prism heights on the airfoil surfaces can be found in the appendix D.1 and D.2.

After generation, each mesh was checked for correctness. A commonly observed error was nodes, which were not in-plane with the front or back symmetry planes they belonged to. Fig. 7.2 shows the flow domain where this is the case. The triangle on the left plane is caused by an outlier node. All nodes of symmetry planes have to be in-plane for the boundary condition to function properly in ANSYS CFX. Therefore, all such nodes were manually repositioned onto their corresponding planes.

7.2 Results

7.2.1 Convergence Criteria

The CFD simulations were canceled if the root mean square (RMS) of the four residuals from the continuity and momentum equations dropped below a value of 10^{-6} . To limit the temporal effort of the investigations, cases where the RMS limit was not reached were canceled after a maximum number of iterations \hat{N}_{iter} of 1 000 or by user interference. In case of the latter, the lift force had either converged to a constant value or oscillated within an acceptable small range. The RMS and the uncertainty of the lift coefficients due to the force oscillations are given in the appendix D.3.

7.2.2 Evaluation of Aerodynamic Coefficients

The values for the lift and drag coefficients which were determined during the optimization process differed a lot from those of the posterior CFD analysis with ANSYS. For the single-

element airfoils, a third value set generated by XFOIL was included in the comparison. The values from MSES/MSIS and XFOIL showed good accordance, while the lift coefficients determined by ANSYS ranged much lower and the drag coefficients much higher. A detailed overview and a description of the encountered effects during the CFD simulation are given in this section.

Fig. 7.3 shows the coefficients which were determined for the single-element airfoils from the 15th-series. The values for all PT are given, from PT₁ in the top row to PT₄ in the bottom row. On average, the drag coefficients which were determined by ANSYS are 3.5 times higher than those from MSES/MSIS. The same accounts for the drag coefficient determined for the 1223-series in fig. 7.4.

Compared to the values from MSES/MSIS, XFOIL generally estimated higher values for the lift coefficients, which is in accordance with literature [73, sec. 4.1, 4.2]. The lift coefficients from ANSYS were on average 30 % lower for all PTs of the 15th-series. This was not the case for the 1223-series, where the lift coefficients determined by ANSYS were only lower for PT₃ and PT₄. For PT₂, all three programs calculated similar lift coefficients. For PT₂, the values determined by ANSYS were the highest.

All drag and lift coefficient values for the double-element airfoils are visualized in fig. 7.5. Similar to the results from the single-airfoil 15th-series, the lift values determined by ANSYS are below and the drag coefficients above those determined by MSES/MSIS, respectively.

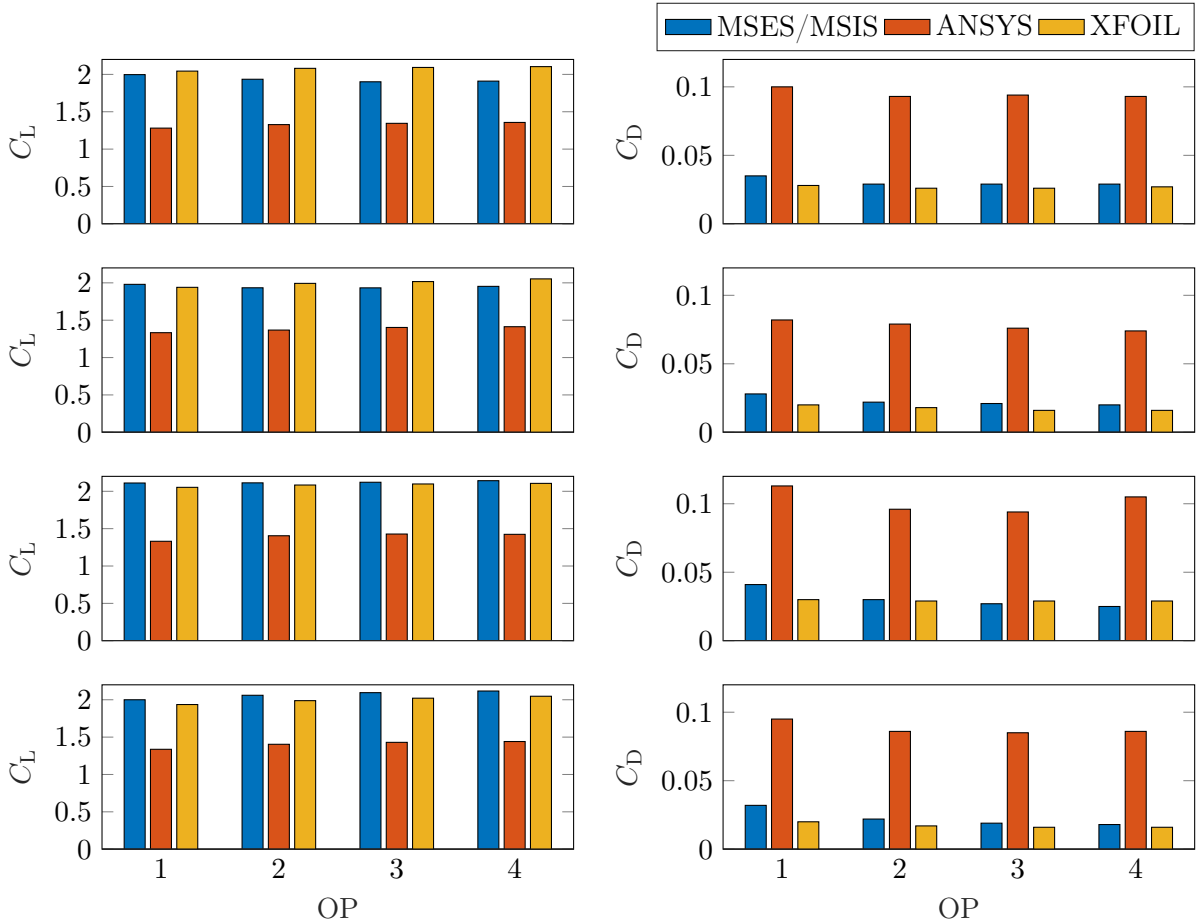


Figure 7.3: Comparison of the lift and drag coefficients of the single-element 15th airfoil configuration determined by MSES/MSIS, ANSYS, and XFOIL. From top to bottom, the figures show PT₁ to PT₄. MSES/MSIS and XFOIL estimate similar values for both coefficients. ANSYS predicts lower values for the lift and higher values for the drag coefficient, respectively.

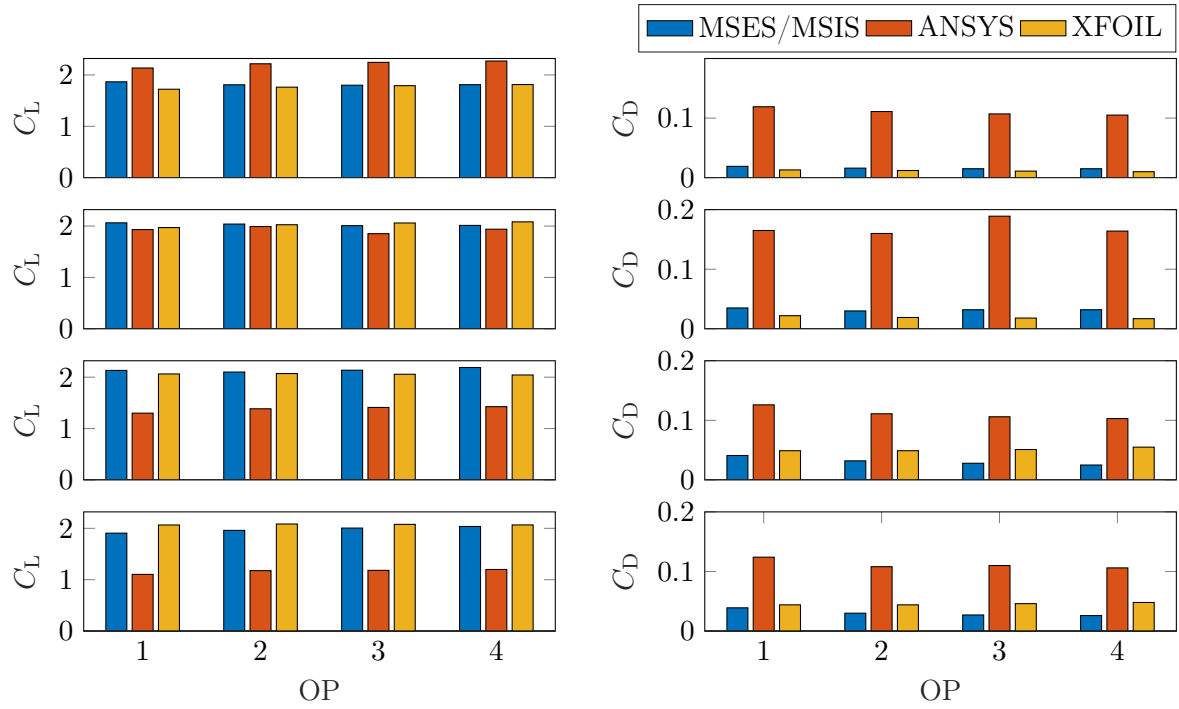
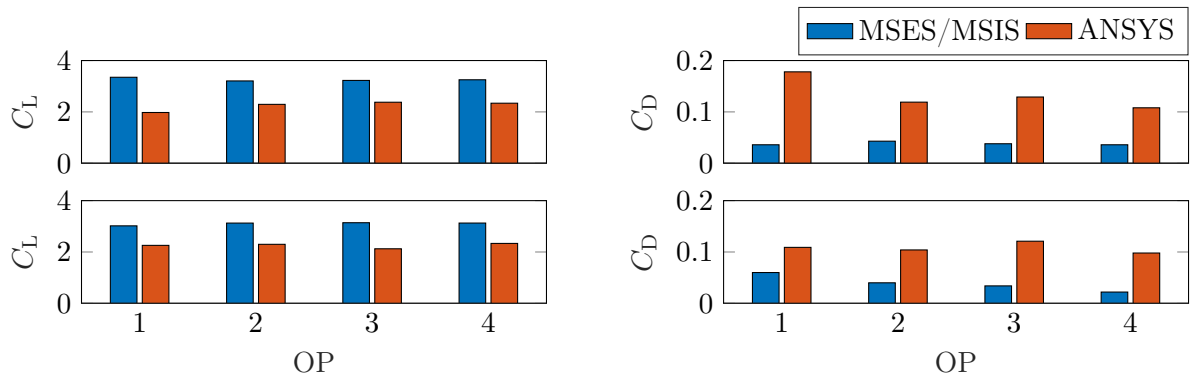
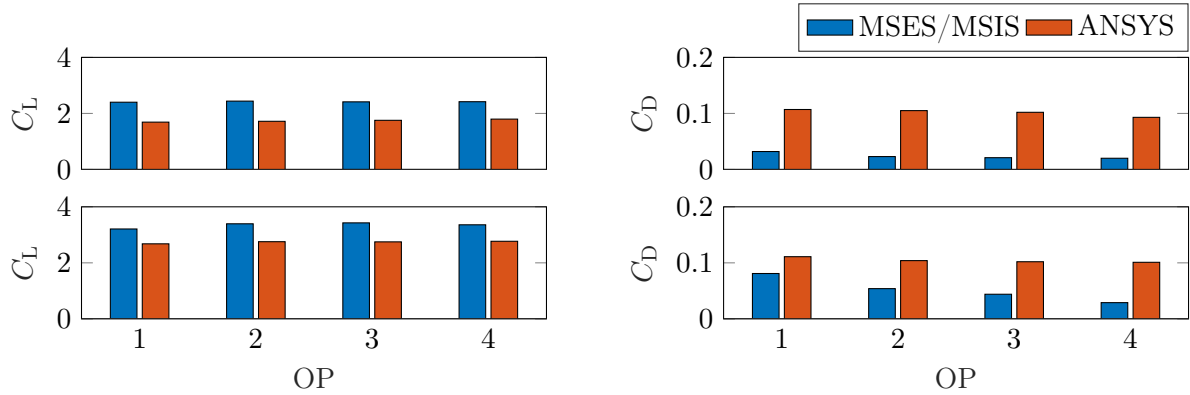


Figure 7.4: Single-element 1223-series. Top to bottom row include bar graphs for PT₁ to PT₄, respectively.



(a) Double-element, 15th base geometry. The top row shows the values for PT₁, the bottom row for PT₂.



(b) Double-element, 1223 base geometry. The top row shows the values for PT₁, the bottom row for PT₂.

Figure 7.5: Comparison of the lift and drag coefficients for the double-element airfoils determined with MSES/MSIS to those calculated by ANSYS CFX.

7.2.3 Flow Separation

The differences in lift and drag coefficient values which are shown in figs. 7.3, 7.4, and 7.5 are correlated to flow separation on the upper side of the airfoils. In almost all cases, the flow separation seemed to be linked to vortices with horizontal rotation, which originated at regions close to the front and back symmetry planes and decreased towards the middle of the flow domain. Thus, besides assessing the global flow state, each airfoil configuration was additionally evaluated at a mid-plane, positioned half-way between the two symmetry planes.

As an example, fig. 7.6 shows the flow field at OP_3 of the single-element airfoil configuration 15th, PT_4 . The streamlines at the mid-plane in fig. 7.6a describe attached flow around the airfoil. However, the global streamlines in fig. 7.6b show severe separation. Two big vortices adjacent to the front and back symmetry plane are visible, with decreasing amplitude towards the mid-plane. The distance between the separation point and the LE is around $0.6l_c$. This phenomenon was present—more or less severely—at all airfoil designs which were evaluated in this work. The separation onset positions of all configurations are given in the appendix D.3. Needless to say, the closer to the LE the flow separated, the smaller the lift coefficient (figs. 7.3, 7.4, 7.5) was, which ANSYS estimated.

The latest onset of turbulence was present at the single-airfoil configuration 1223, PT_1 . Depending on the OP, the distance between the LE and the separation point was between 0.6 and $0.8l_c$. This corresponds to the highest ANSYS lift coefficients of all runs (fig. 7.4). As the distance between the separation point and the LE steadily decreased for all subsequent runs with higher parameterization, the lift coefficients determined by the CFD simulation dropped as well.

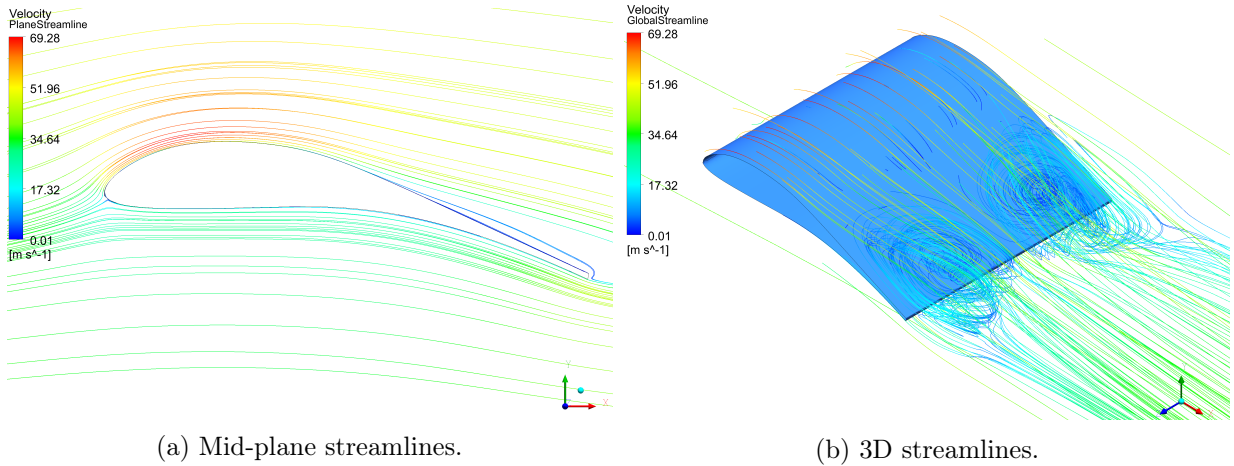


Figure 7.6: Streamlines of single-element configuration 15th, PT_4 at OP_3 . Images used by courtesy of ANSYS, Inc..

Conclusion and Outlook

In the presented thesis, an approach for multi-element airfoil optimization for drag power kites was developed based on existing research. The evolutionary optimization algorithm CMA-ES was implemented in a Matlab routine to explore the solution space of possible airfoil parameters. Within user-defined boundaries, system calls to the underlying Linux operating system were executed to calculate the flow solution with MSES. The investigation was performed at four OPs which covered a range of apparent airspeeds specific for the drag power kite system in development at the TUM. The optimization was conducted for single- and double-element airfoils. The aerodynamic coefficients C_L and C_D of the optimized airfoils were verified with a posterior CFD simulation in ANSYS CFX. For all single-element airfoils, XFOIL parameter values were utilized for the comparison as well.

An investigation of the influence of different kinematic viscosity values prior to the optimizations showed that no significant impact on convergence behavior was present for values within the temperature range of the system. A second sensitivity analysis was conducted for maximum newton iterations in MSES. For single-element airfoils, convergence probability increased if more than 250 Newton iterations were allowed during each call to MSES/MSIS.

It was shown, that an increase in geometric DOF for the airfoil parameterization correlated with an improved behavior in terms of maximum achievable lift. However, different optimization run-times and early abortion by the CMA-ES algorithm had a significant influence on the aerodynamic performance.

The developed cost function with four different regions covering (i) solution convergence, (ii) divergence, (iii) invalid airfoil geometries, and (iv) boundary violations showed a good capability to guide the optimizer towards convergence.

An adaptation of the cost function in Region 2 had a beneficial effect on the success rate of the optimizations. The analysis of the MSES/MSIS calculation residuals was utilized to lower the amount of unsuccessful calls to the flow solver and increased the share of converged solutions. Premature cancellation by the optimization algorithm (e.g. due to stagnation) was reduced. The amount of parameter evaluations in cost Regions 3 (invalid airfoil geometry) and 4 (boundary violations) were low, which indicates that the guidance of the optimization algorithm towards Regions 1 and 2 is sufficient.

Nonetheless, the amount of unconverged calls to the flow solver remained comparatively high. Further improvement is thought to be achieved by the following approaches:

1. Nifty use of the mdat-files of converged OPs. If some of the OPs did converge and some did not, the calculated solution (which is stored in the mdat-file) of a converged OP can be used to converge another OP. In the same manner in which MSES already uses prior solutions (e.g. at slightly different AOA in MPOLAR) to converge a new configuration, the solution at another OP can be used.
2. Similarly, the Re and Ma Numbers of any unconverged OP can be adapted slightly to generate a first solution. If one is found, the parameter can be driven towards the actual value to generate the final solution.

3. During the implementation of the refined cost function for Region 2, some cases were observed in which the flow converged towards a solution, i.e. the residuals introduced in sec. 4.5.2 decreased steadily, but did not manage to fall below the critical threshold within the amount of allowed Newton iterations. In such cases, this behavior could be detected and \hat{N}_{Newton} increased dynamically to converge the flow.

The CFD analysis and verification of the aerodynamic coefficients showed a huge difference in estimated values for C_L and C_D between ANSYS and MSES/MSIS, while the values from XFOIL showed better accordance to the values from MSES/MSIS. At almost all airfoil configurations separation was present in ANSYS, which explains the lower lift and drag coefficient values. Two investigations could generate a better understanding of those differences.

The first might be based on the presumption that the big differences arose from an insufficient resolution of laminar separation bubbles on the suction side of the airfoils. It is mentioned in [60], that a mesh refinement in stream-wise direction can be used to resolve such problems. Even though an initial investigation (sec. 6.2.3) did not improve the results as expected, a mesh refinement perpendicular to the stream direction might improve detection thereof as well and generate coefficient values which are closer to the more reliable values generated with ANSYS.

A second approach could focus on the CFD analysis. For most cases in which severe separation was present, it was stronger towards the symmetry planes of the simulated domain. One run, which was simulated with an increased domain width of $1.25l_c$ resulted in huge differences in lift and drag coefficients. Both values were 20 % lower than the values from the same simulation with a domain width of l_c . The symmetry boundary condition might influence the CFD solution: Fluid partial deflection at the planes might result in the vortices, as explained in sec. 7.2.3. This possible plane-induced separation might be resolved by using translational periodic boundary conditions instead of symmetry planes.

The optimization strategy presented in this work (figs. 1.2, 4.3) consisted of an optimization routine implemented in Matlab which accessed the low fidelity, fast flow solver MSES, and a posterior validation of the results in ANSYS CFX. This approach was believed deliver results of good accordance. However, the contrary was the case. By including the CFD results into the iterative optimization process, more consistent results might be achieved. To find a compromise between the greater computational efforts, a CFD validation could only be performed every other iteration.

Another approach could be the separation of DOF during the individual optimizations. Instead of generating an initial good solution with less airfoil parameters as is done in this work, the different parameters could e.g. be split up into shape and positioning parameters which are then optimized separately in an iterative manner (cf. [43]). Such an approach might improve the convergence capabilities for multi-element airfoils, which was found to be low with the current setup.

Work Plan

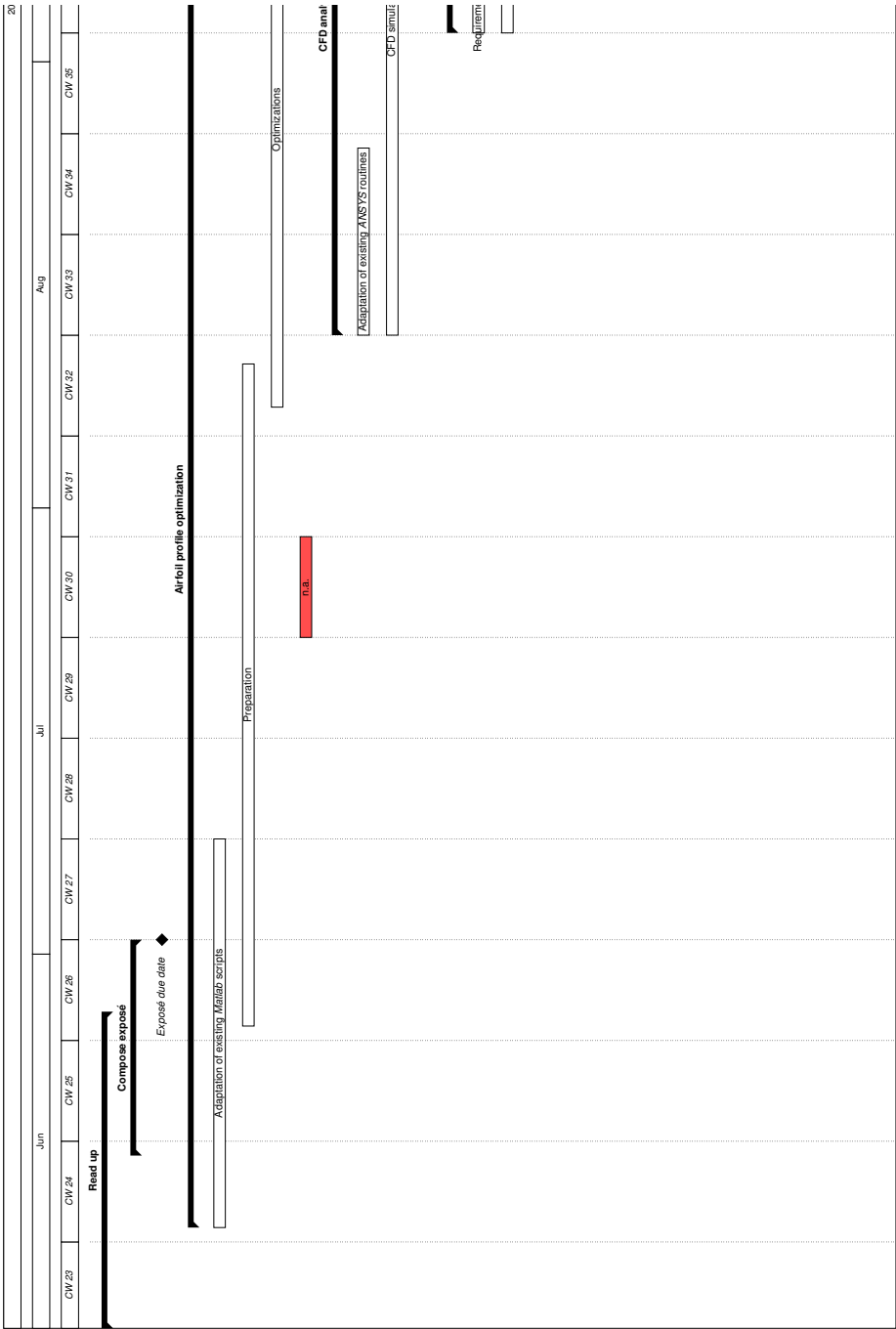


Figure A.1: Gantt chart of the initially planned schedule for the master's thesis (part 1/2).

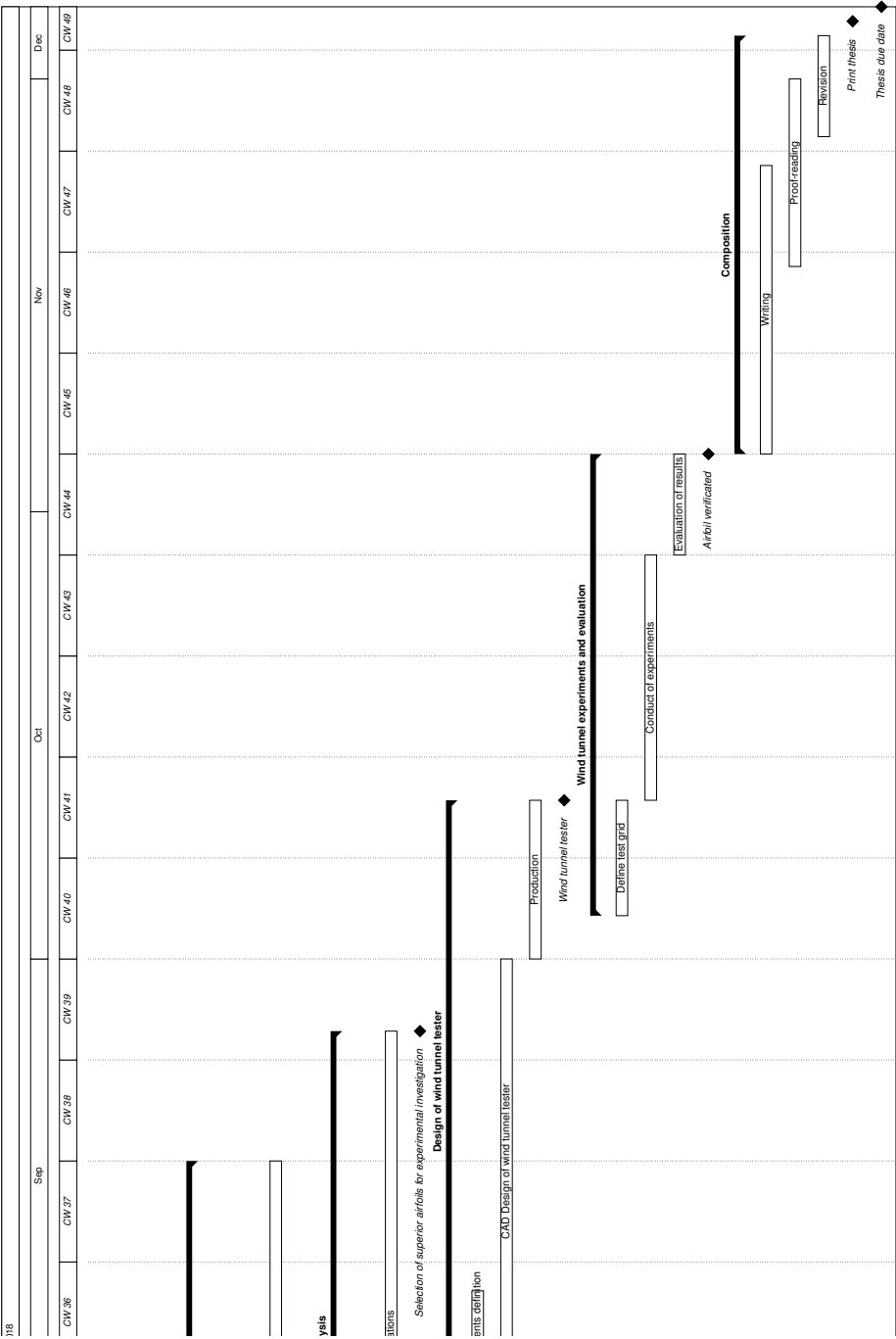


Figure A.1: Gantt chart of the planned schedule for the master's thesis (part 2/2).

Base Airfoils

B.1 Base Geometries

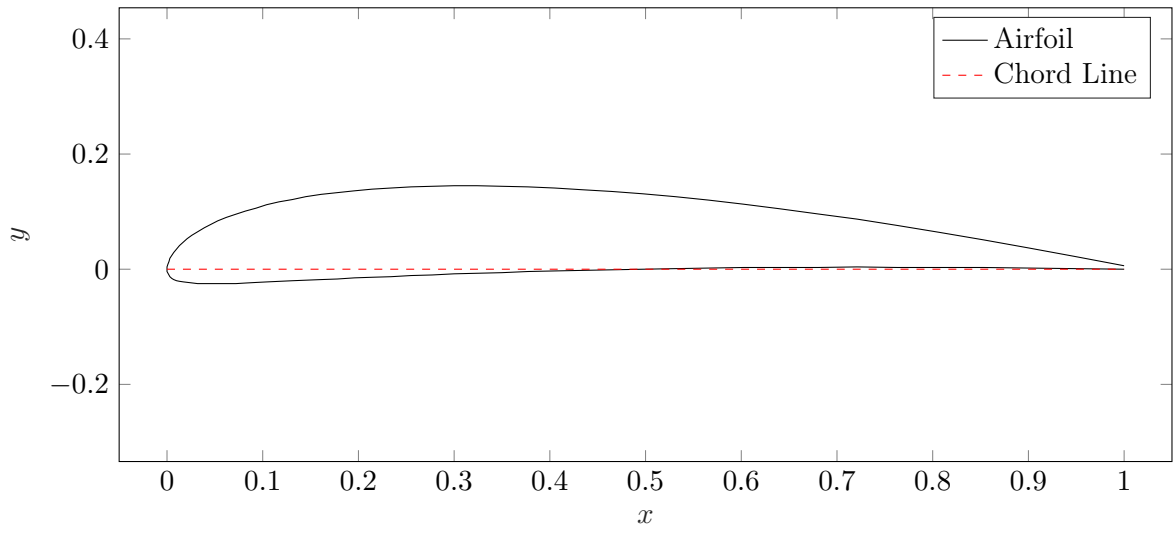


Figure B.1: 15th base geometry, PT_1 . Normalized coordinates.

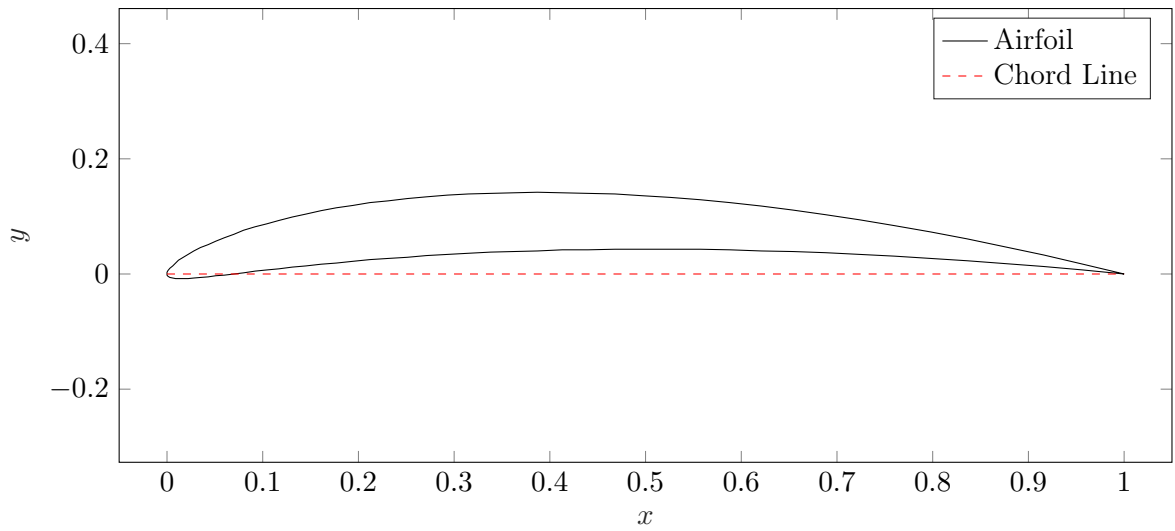
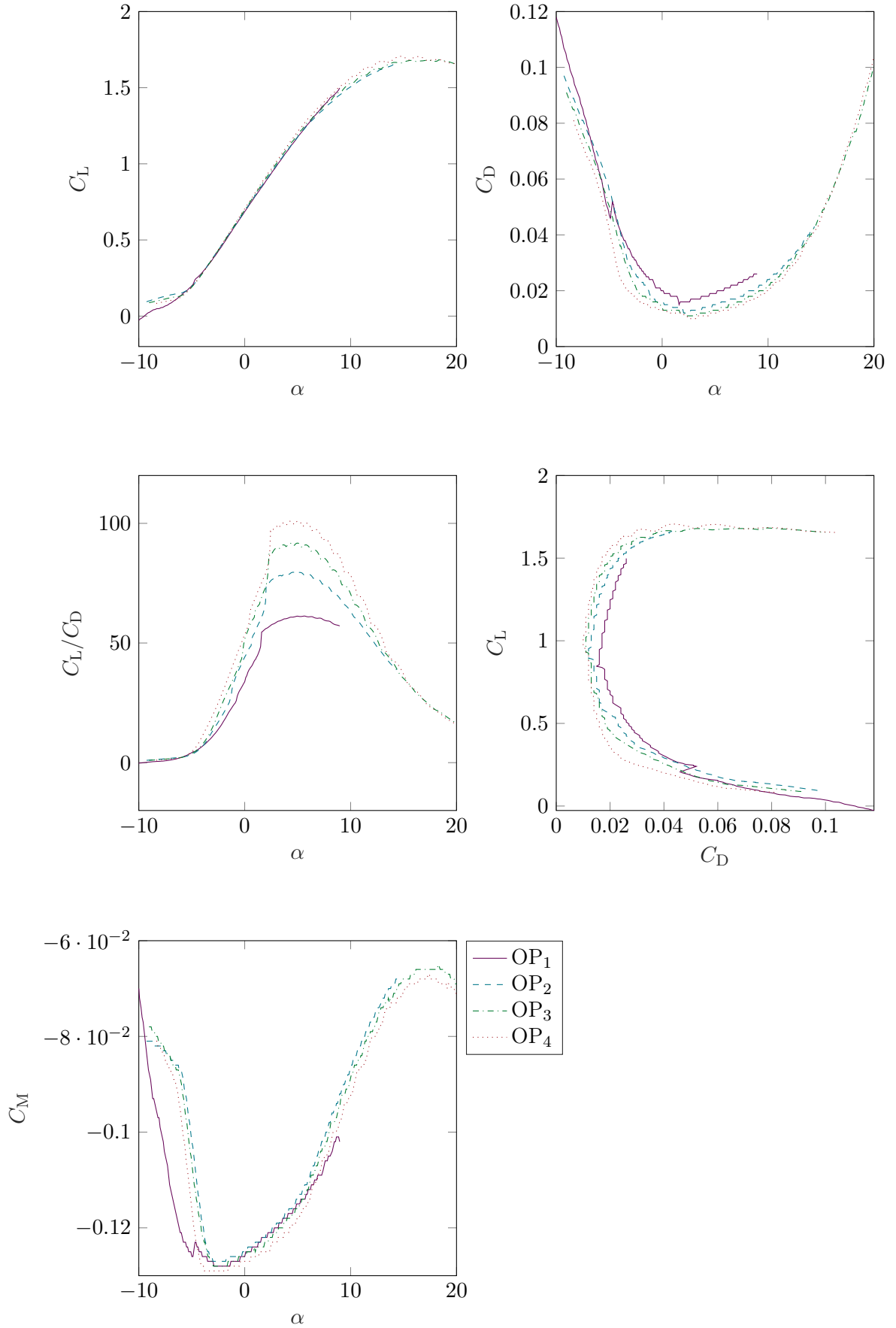
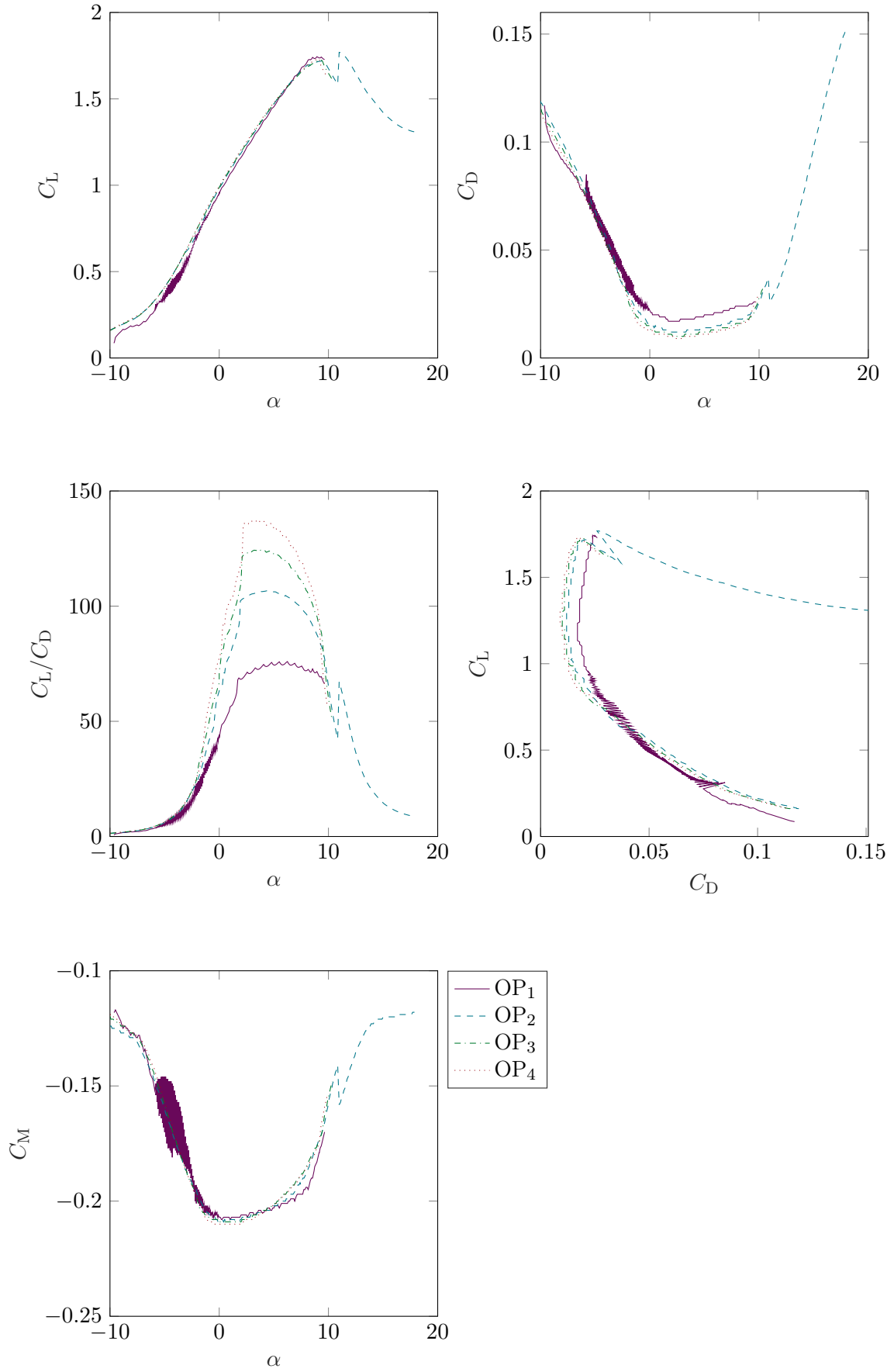


Figure B.2: 1223 base geometry, PT_1 . Normalized coordinates.

B.2 Polars

Figure B.3: 15th base geometry, PT_1 .

Figure B.4: 1223 base geometry, PT₁.

Polar Data

On the following pages, the polar plots of the optimized airfoil designs are listed. For each configuration, the polar data is given for every OP. If no line is plotted, the flow solution with MSES/MSIS did not converge at the corresponding angles. The vertical, dashed lines mark the optimum angle. For a detailed explanation, refer to sec. [6.2](#).

C.1 Single-Element Airfoils

C.1.1 15th-Series

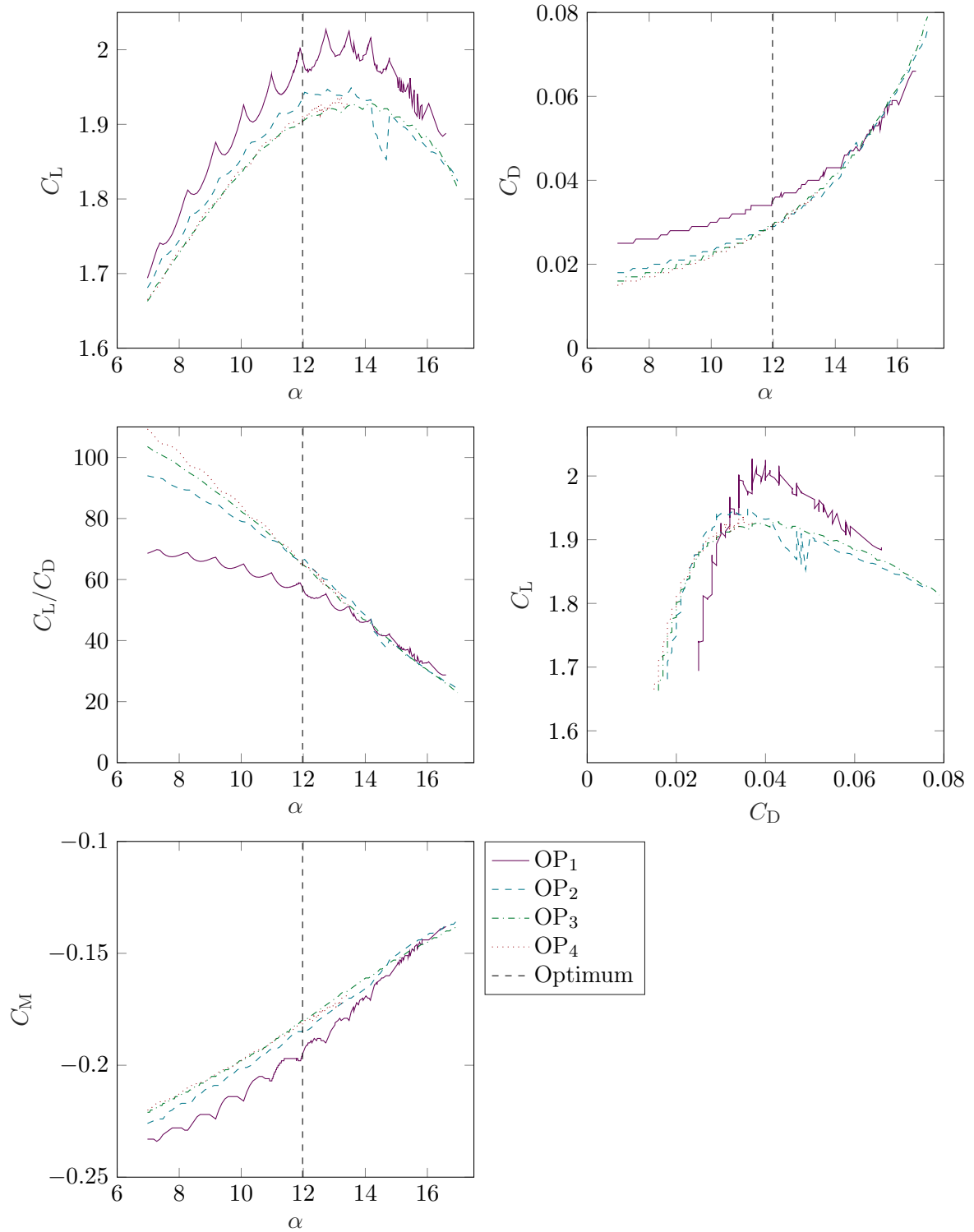
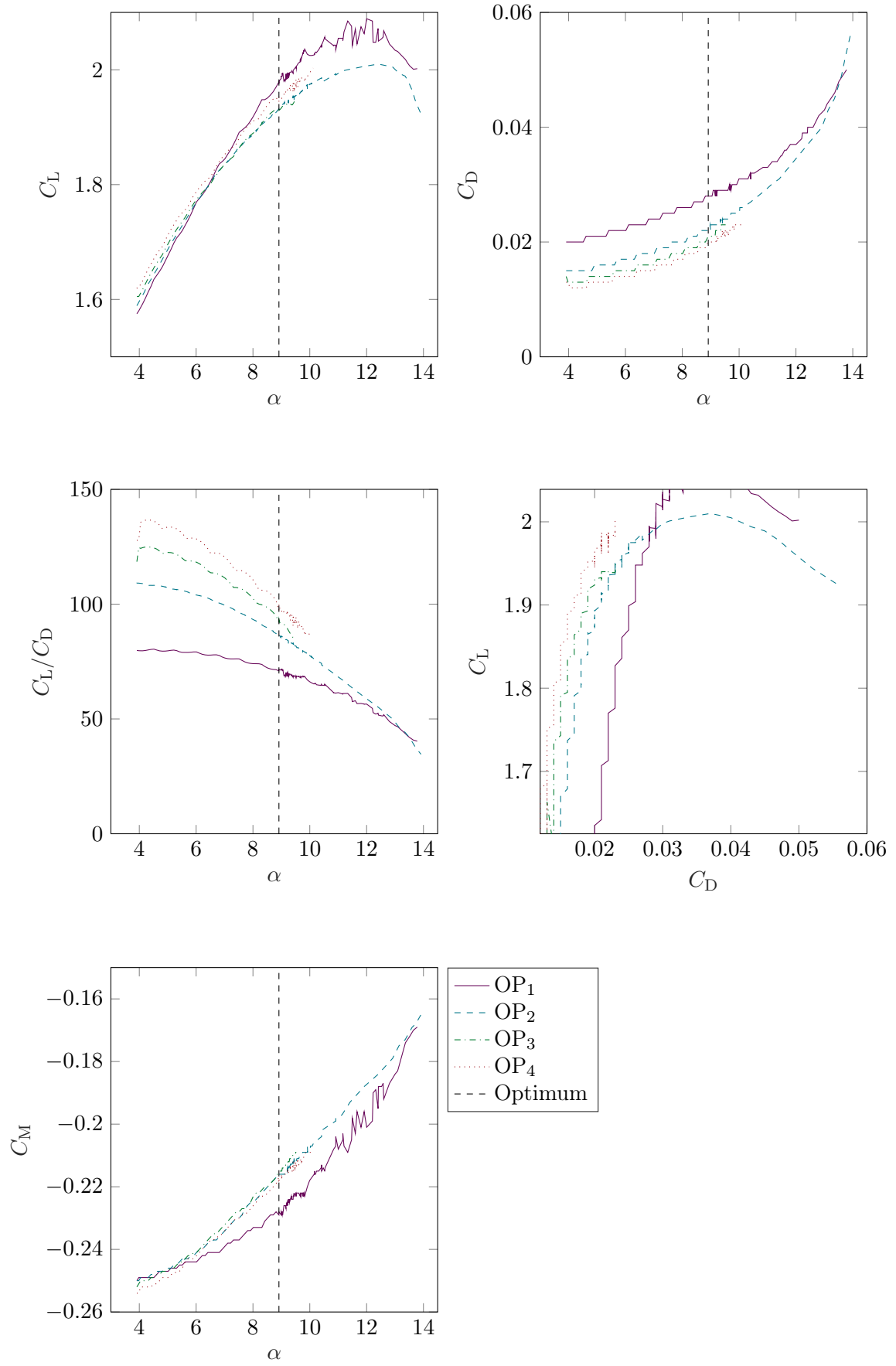
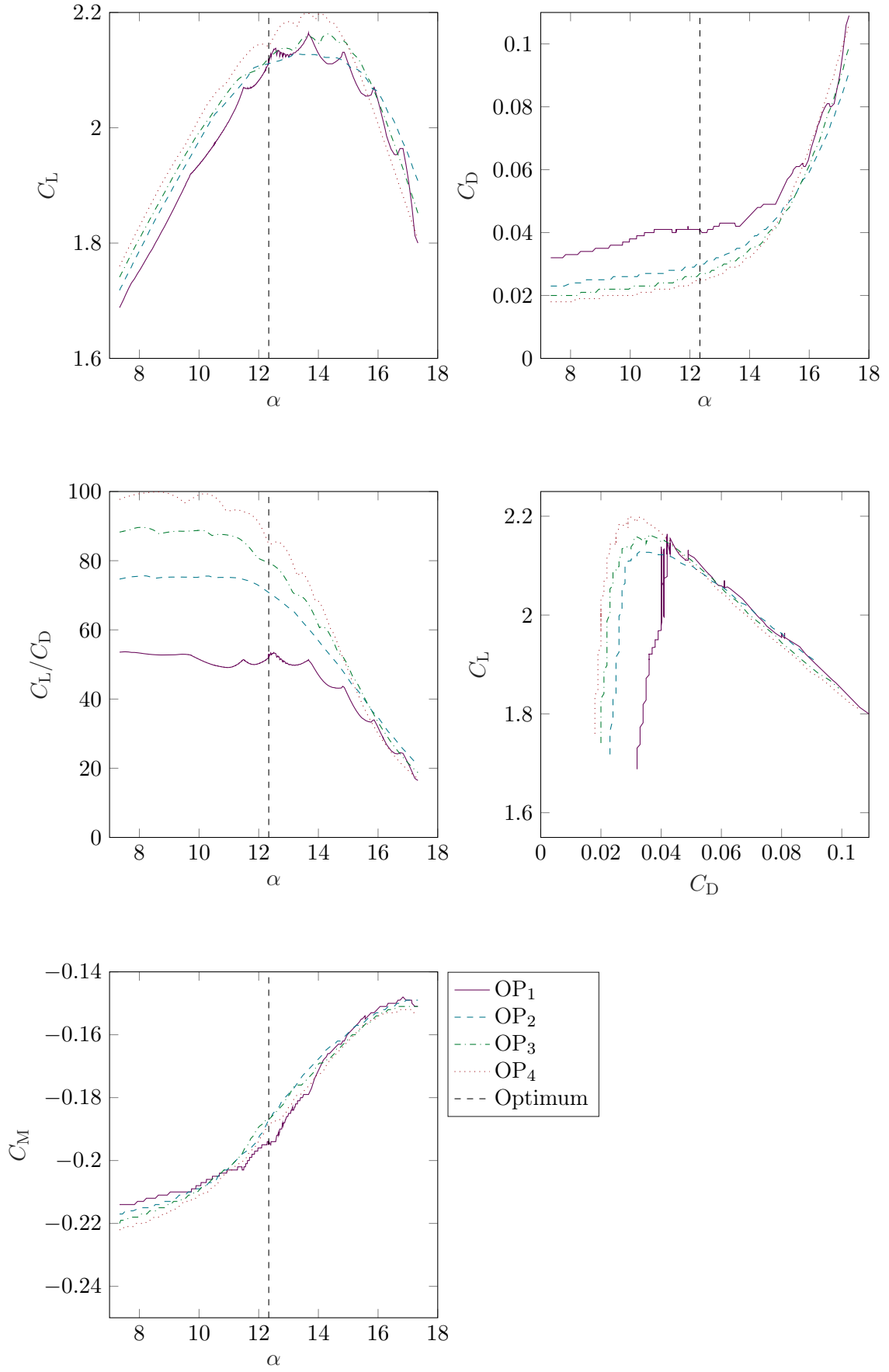
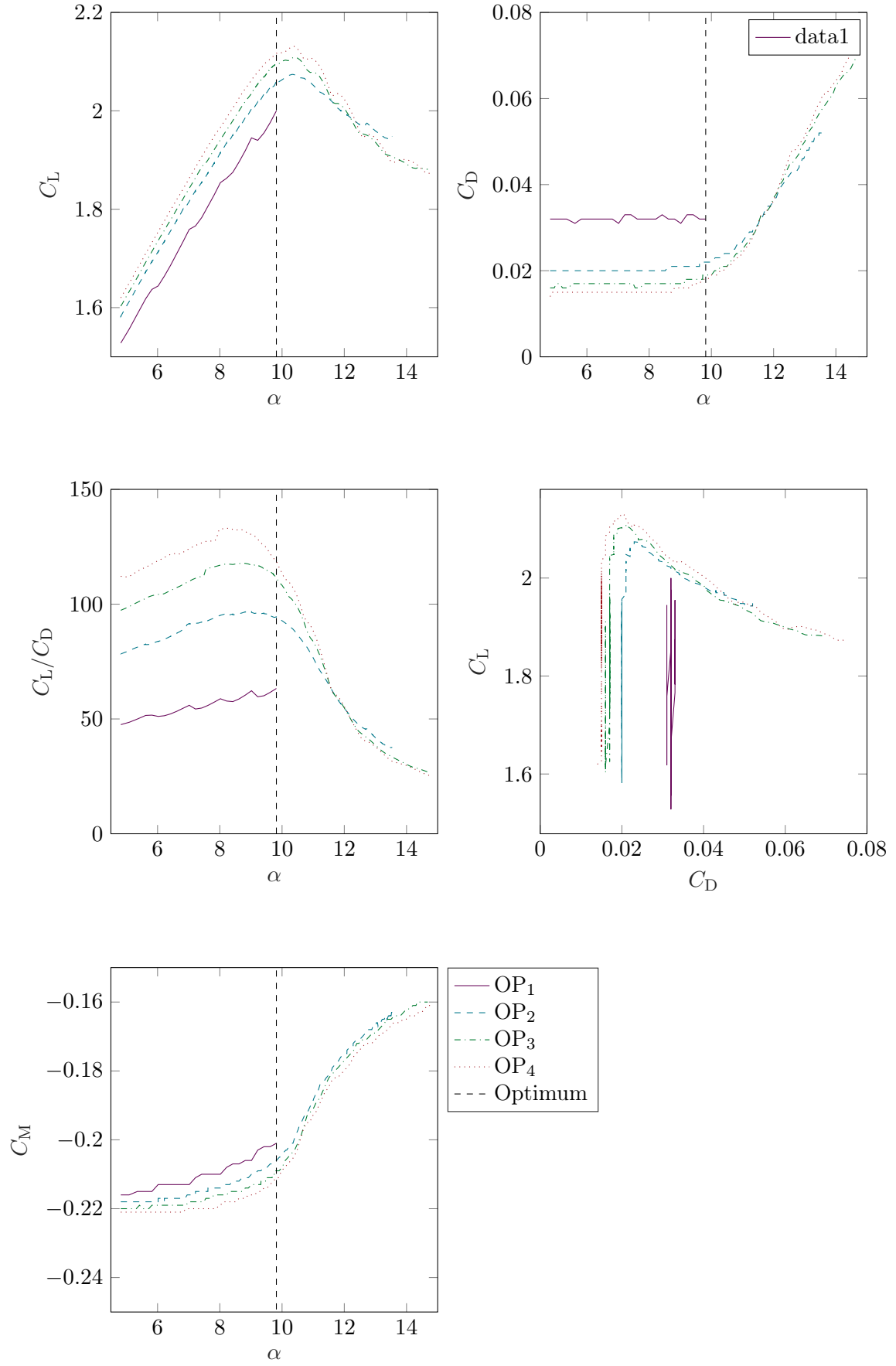


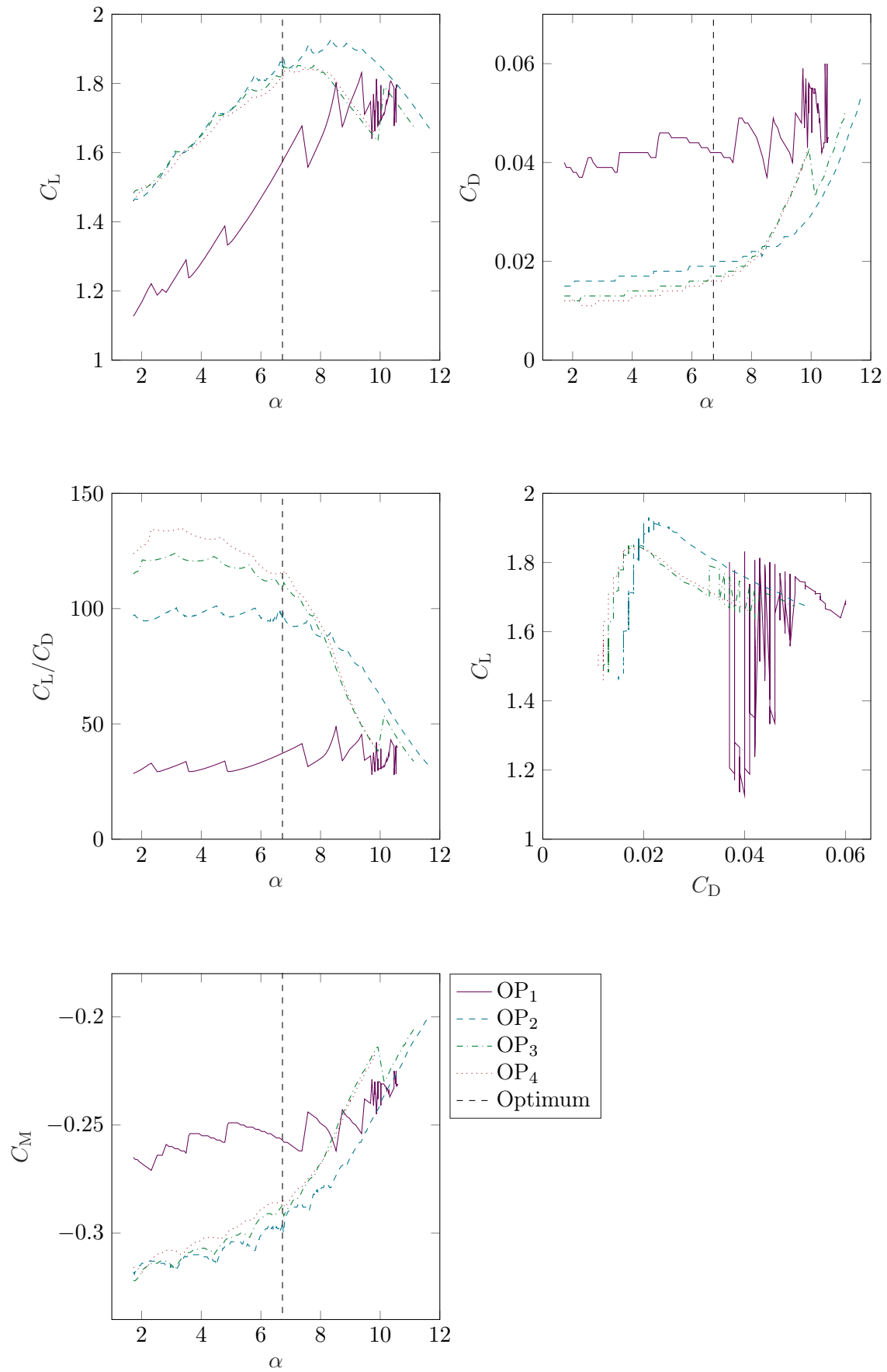
Figure C.1: 15th base geometry, PT₁.

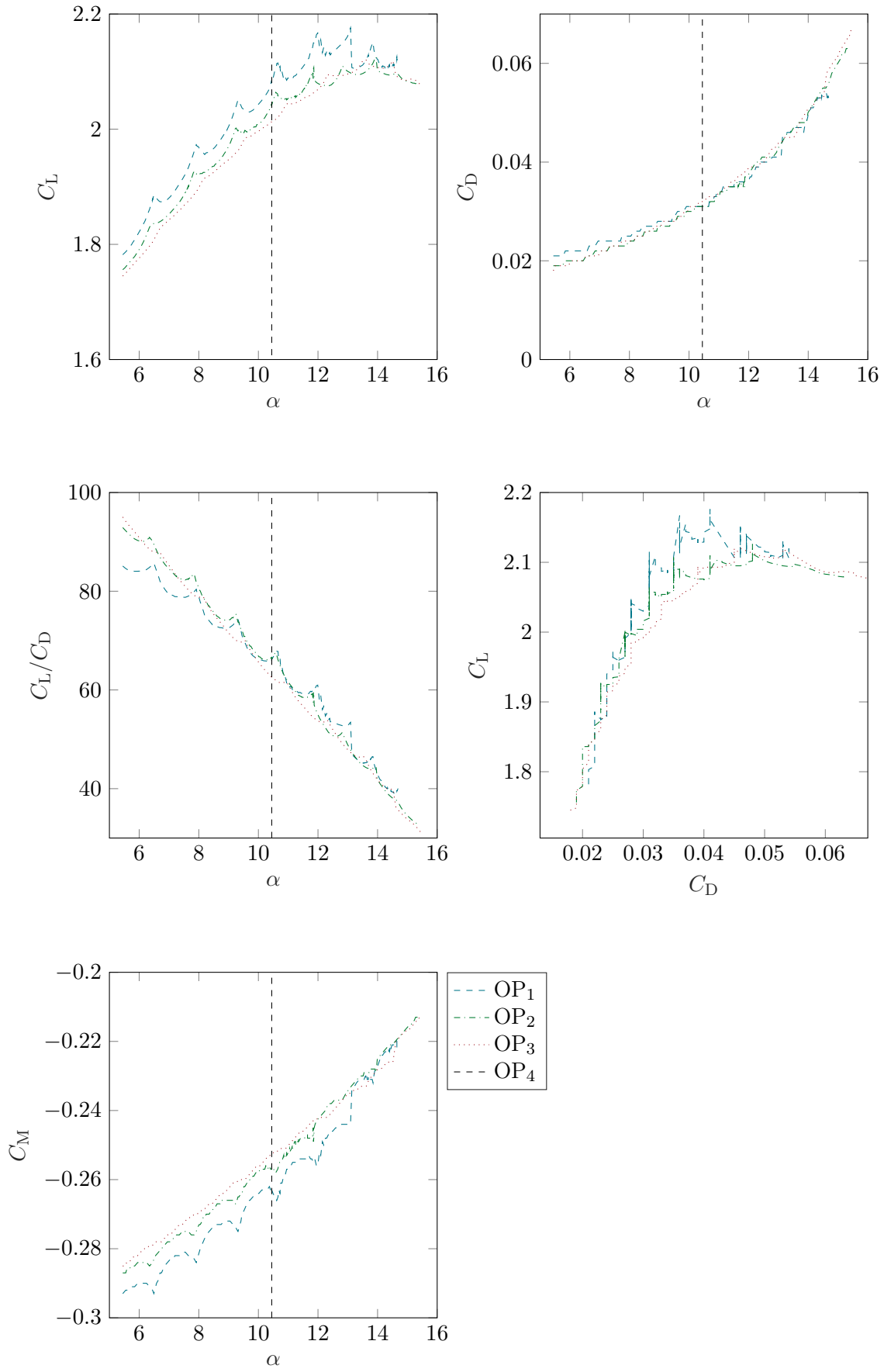
Figure C.2: 15th base geometry, PT₂.

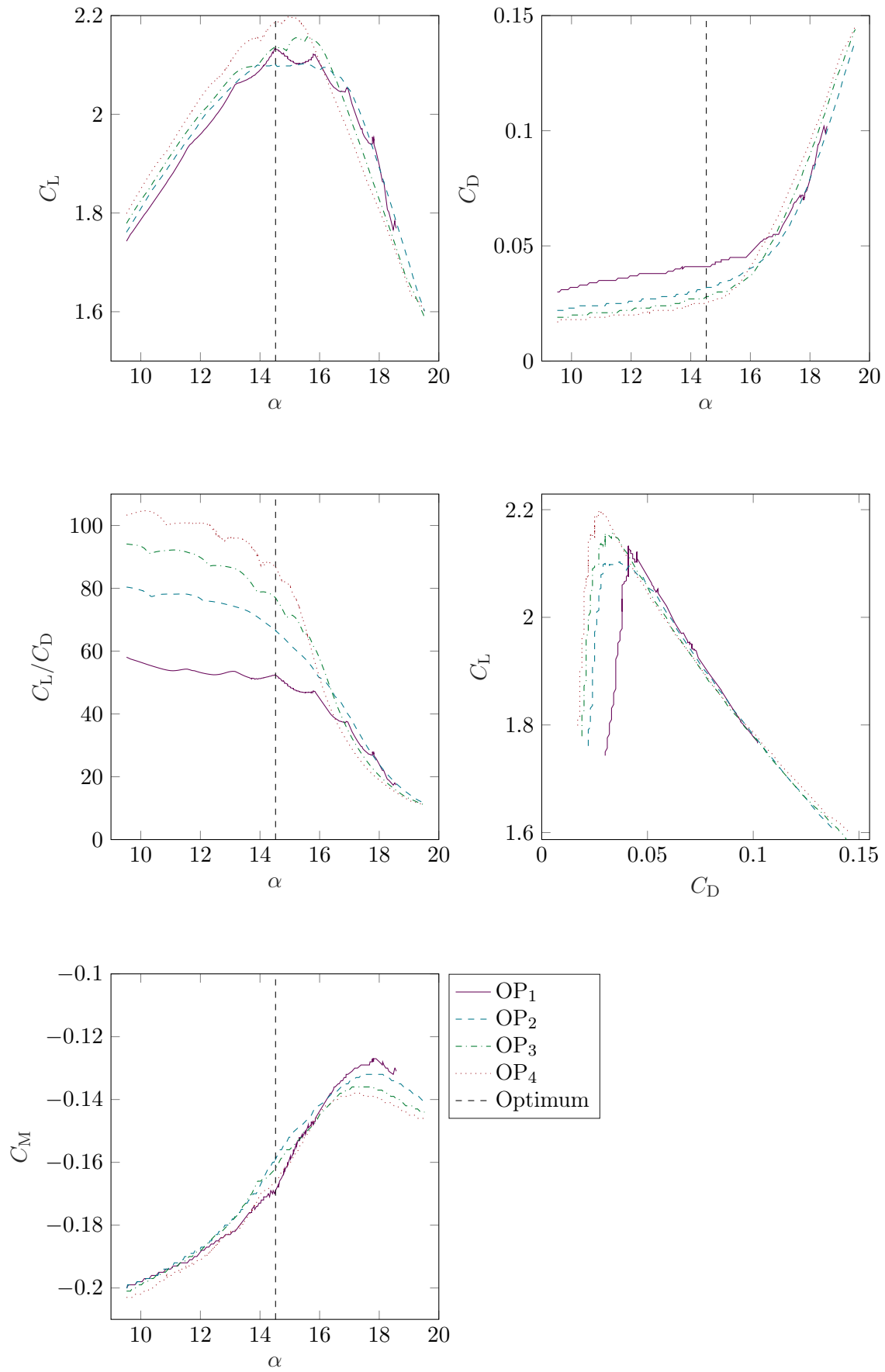
Figure C.3: 15th base geometry, PT₃.

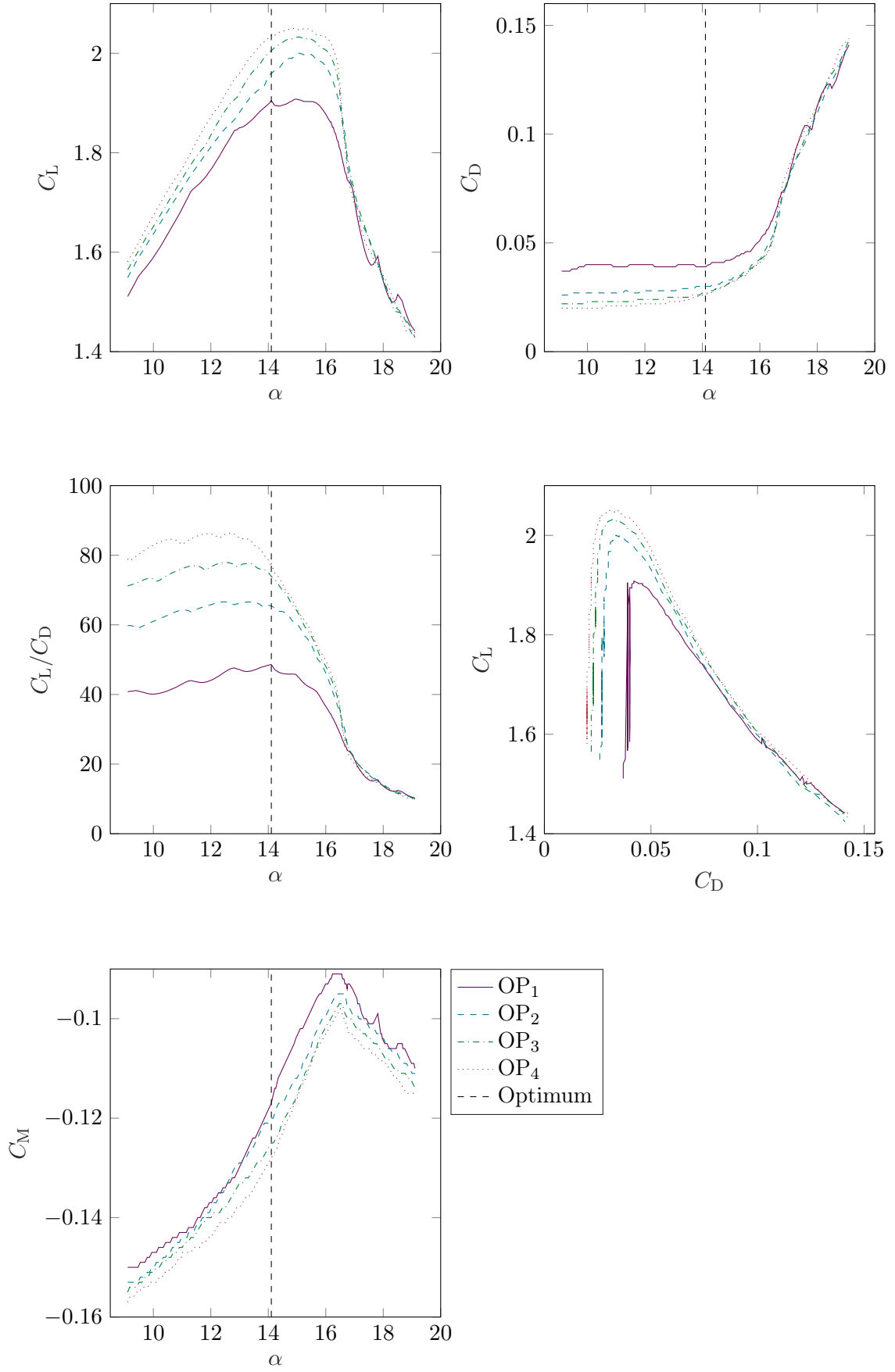
Figure C.4: 15th base geometry, PT₄.

C.1.2 1223-Series

Figure C.5: 1223 base geometry, PT₁.

Figure C.6: 1223 base geometry, PT₂.

Figure C.7: 1223 base geometry, PT₃.

Figure C.8: 1223 base geometry, PT₄.

C.2 Double-Element Airfoils

C.2.1 15th-Series

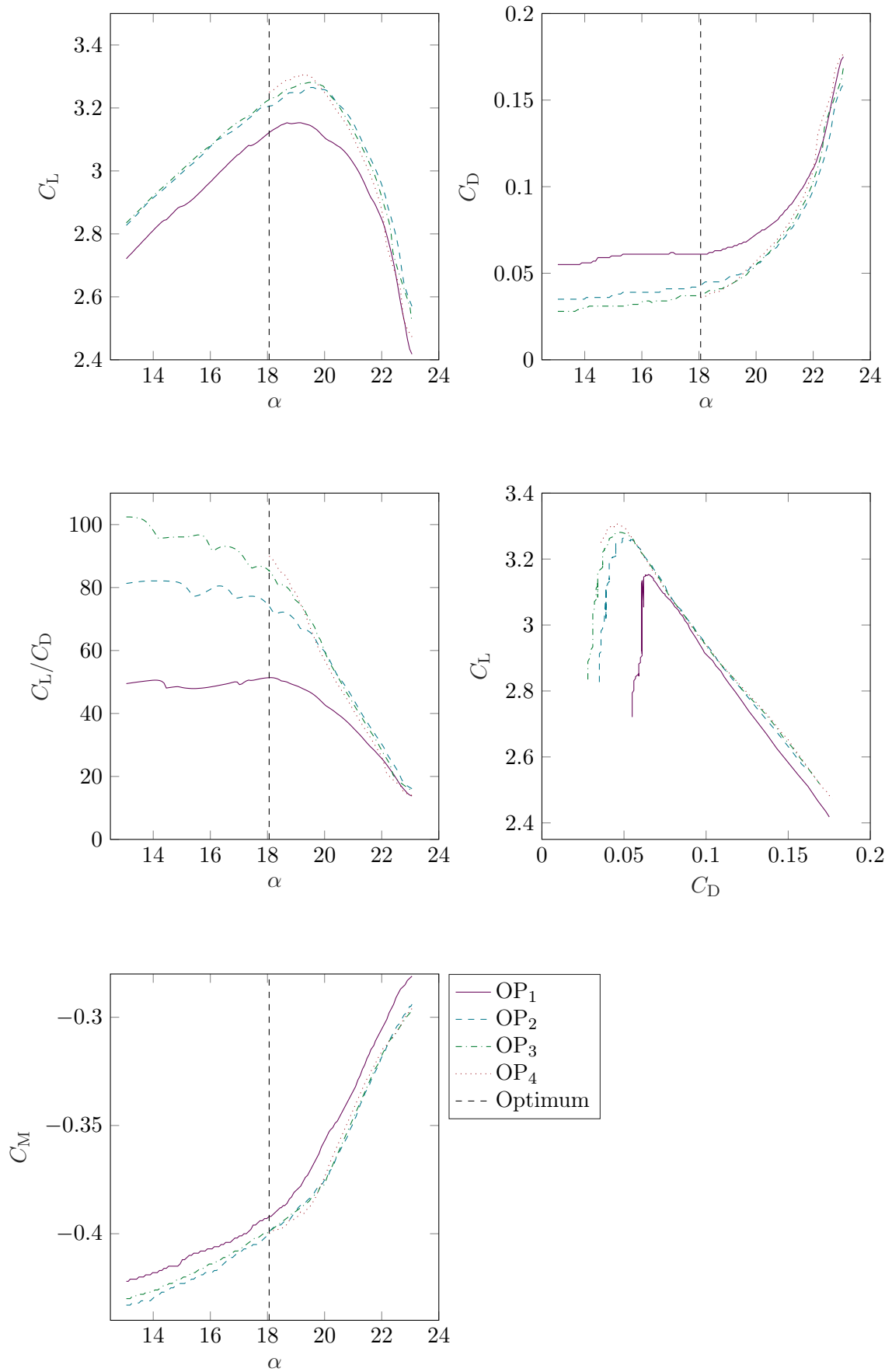
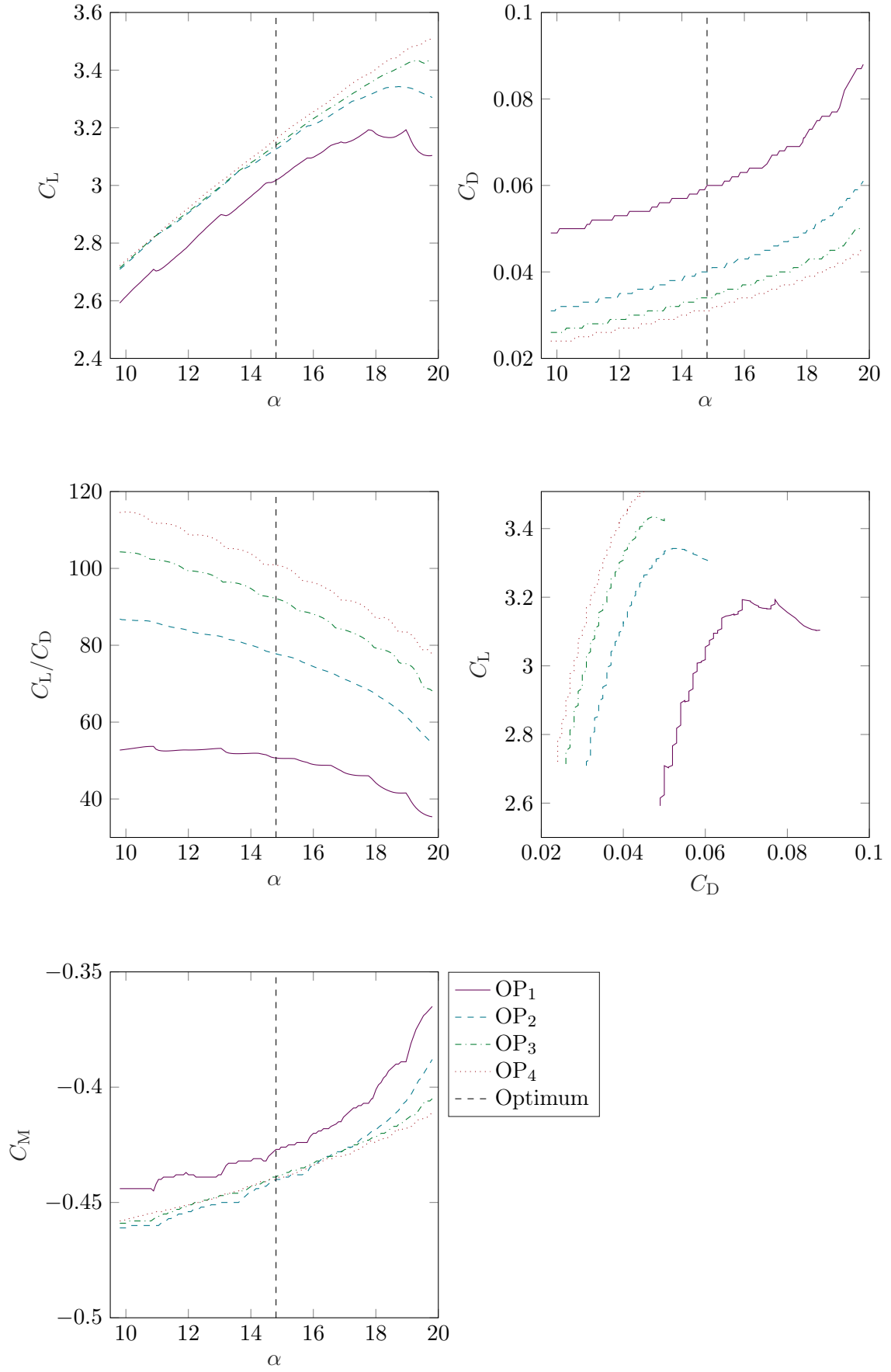
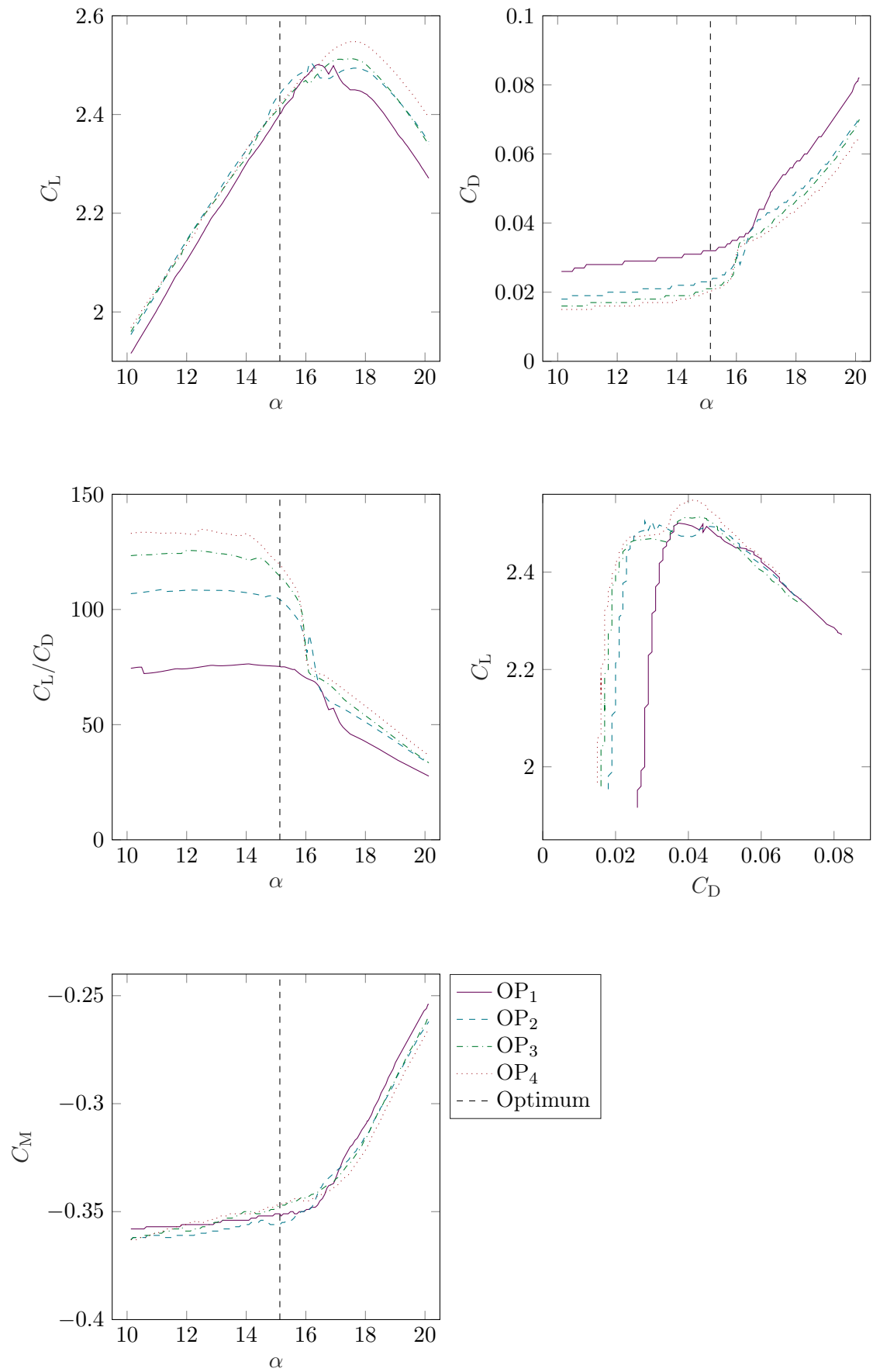
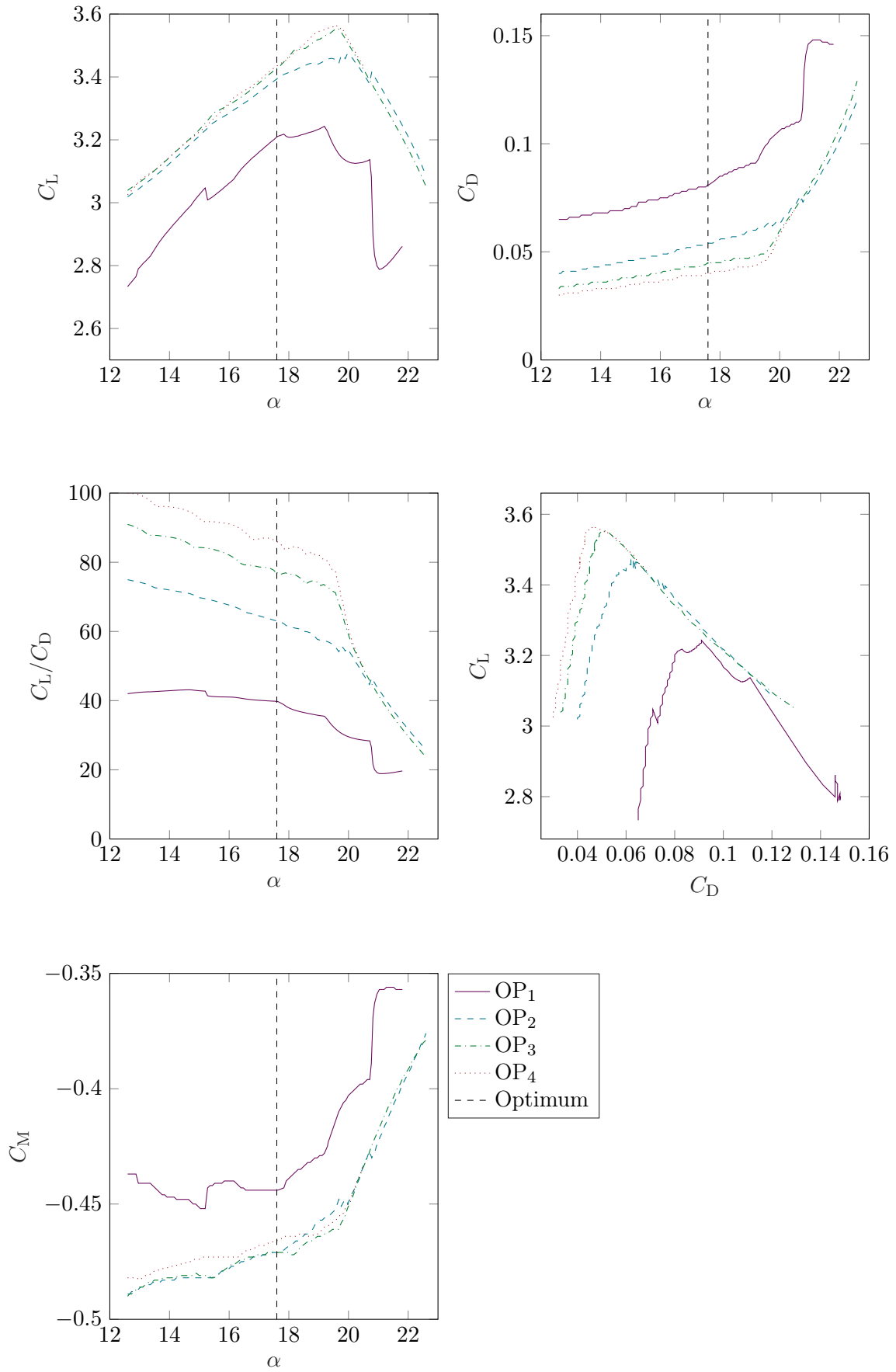


Figure C.9: 15th base geometry, PT₁.

Figure C.10: 15th base geometry, PT₂.

C.2.2 1223-Series

Figure C.11: 1223 base geometry, PT₁.

Figure C.12: 1223 base geometry, PT₂.

Computational Fluid Dynamics Analysis

D.1 Mesh Characteristics Single-Element Airfoils

Base Geometry	PT	OP	Init. Prism Height	Number of Nodes	\hat{y}^+	\bar{y}^+
15th	PT ₁	1	$6.40 \cdot 10^{-6}$	334 482	0.995	0.335
		2	$4.27 \cdot 10^{-6}$	335 011	1.113	0.390
		3	$2.85 \cdot 10^{-6}$	335 075	1.020	0.379
		4	$2.28 \cdot 10^{-6}$	335 076	1.044	0.393
	PT ₂	1	$6.40 \cdot 10^{-6}$	327 728	0.944	0.328
		2	$3.88 \cdot 10^{-6}$	328 009	0.965	0.335
		3	$2.85 \cdot 10^{-6}$	328 062	0.987	0.373
		4	$2.28 \cdot 10^{-6}$	328 114	1.006	0.387
	PT ₃	1	$6.40 \cdot 10^{-6}$	353 778	1.048	0.301
		2	$3.88 \cdot 10^{-6}$	354 995	1.070	0.312
		3	$2.85 \cdot 10^{-6}$	355 116	1.103	0.336
		4	$2.28 \cdot 10^{-6}$	335 138	1.116	0.363
	PT ₄	1	$6.40 \cdot 10^{-6}$	347 111	0.905	0.322
		2	$3.88 \cdot 10^{-6}$	347 711	0.926	0.346
		3	$2.85 \cdot 10^{-6}$	347 748	0.942	0.366
		4	$2.28 \cdot 10^{-6}$	347 762	0.954	0.382
1223	PT ₁	1	$9.01 \cdot 10^{-6}$	552 814	0.998	0.405
		2	$6.01 \cdot 10^{-6}$	554 276	1.098	0.476
		3	$4.01 \cdot 10^{-6}$	554 988	1.067	0.459
		4	$3.20 \cdot 10^{-6}$	555 096	1.064	0.477
	PT ₂	1	$7.37 \cdot 10^{-6}$	474 332	1.102	0.343
		2	$4.62 \cdot 10^{-6}$	475 143	1.233	0.389
		3	$1.78 \cdot 10^{-6}$	475 551	0.796	0.255
		4	$1.52 \cdot 10^{-6}$	475 546	0.871	0.270
	PT ₃	1	$4.92 \cdot 10^{-6}$	350 594	0.815	0.253
		2	$3.28 \cdot 10^{-6}$	350 913	0.916	0.291
		3	$2.19 \cdot 10^{-6}$	350 992	0.855	0.282
		4	$1.75 \cdot 10^{-6}$	351 009	0.877	0.291
	PT ₄	1	$4.92 \cdot 10^{-6}$	343 787	1.071	0.239
		2	$3.28 \cdot 10^{-6}$	344 068	1.250	0.268
		3	$2.19 \cdot 10^{-6}$	344 120	1.173	0.270
		4	$1.75 \cdot 10^{-6}$	344 125	1.217	0.277

D.2 Mesh Characteristics Double-Element Airfoils

Base Geometry	PT	OP	Init. Prism Height	Number of Nodes	\hat{y}^+	\bar{y}^+
15th	PT ₁	1	$6.40 \cdot 10^{-6}$	361 431	1.217	0.360
		2	$6.40 \cdot 10^{-6}$	362 256	1.264	0.357
		3	$1.90 \cdot 10^{-6}$	362 494	0.972	0.297
		4	$1.52 \cdot 10^{-6}$	362 527	1.006	0.308
	PT ₂	1	$4.57 \cdot 10^{-6}$	377 543	0.914	0.290
		2	$2.67 \cdot 10^{-6}$	377 888	0.931	0.304
		3	$1.90 \cdot 10^{-6}$	163 150	0.820	0.320
		4	$1.52 \cdot 10^{-6}$	377 959	0.952	0.325
1223	PT ₁	1	$4.57 \cdot 10^{-6}$	357 985	0.940	0.260
		2	$2.67 \cdot 10^{-6}$	358 265	0.932	0.272
		3	$1.90 \cdot 10^{-6}$	358 324	0.943	0.278
		4	$1.52 \cdot 10^{-6}$	358 265	1.632	0.439
	PT ₂	1	$4.57 \cdot 10^{-6}$	402 708	0.748	0.299
		2	$1.90 \cdot 10^{-6}$	403 541	0.802	0.314
		3	$1.52 \cdot 10^{-6}$	403 601	0.818	0.321
		4	$1.52 \cdot 10^{-6}$	403 601	0.856	0.333

D.3 Simulation Results

This chapter includes tables with the results from the CFD post-analysis and the values from MSES/MSIS. For all single-element configurations the XFOIL values are included as well. For runs in which the force did not converge completely, but oscillated between two values, the upper and lower values of the lift coefficient are provided as well. If not all convergence criteria fell below the threshold value 10^{-6} , the maximum RMS is listed. The separation onset is given in percentages w.r.t. to the chord length (of each element itself) along the suction side of the element, 0 % being at the LE, 100 % at the TE.

D.3.1 15th-Series, Single-Element

PT	OP	ANSYS		Separation Onset	max. RMS	MSES/MSIS		XFOIL	
		C_L	C_D			C_L	C_D	C_L	C_D
PT ₁	1	1.281	0.100	50%	10^{-6}	1.997	0.035	2.044	0.028
	2	1.328	0.093	60%	10^{-6}	1.935	0.029	2.081	0.026
	3	1.345	0.094	60%	10^{-6}	1.901	0.029	2.093	0.026
	4	1.357	0.093	60%	10^{-6}	1.910	0.029	2.104	0.027
PT ₂	1	1.333	0.082	60%	10^{-6}	1.980	0.028	1.940	0.020
	2	$1.368^{+0.008}_{-0.000}$	0.079	60%	$4 \cdot 10^{-4}$	1.934	0.022	1.993	0.018
	3	$1.403^{+0.003}_{-0.001}$	0.076	70%	$3 \cdot 10^{-4}$	1.933	0.021	2.017	0.016
	4	$1.413^{+0.003}_{-0.001}$	0.074	70%	$4 \cdot 10^{-4}$	1.953	0.020	2.053	0.016
PT ₃	1	1.331	0.113	40%	10^{-6}	2.111	0.041	2.053	0.030
	2	$1.405^{+0.002}_{-0.002}$	0.096	50%	$2 \cdot 10^{-4}$	2.113	0.030	2.084	0.029
	3	$1.428^{+0.001}_{-0.011}$	0.094	50%	$3 \cdot 10^{-4}$	2.121	0.027	2.098	0.029
	4	1.424	0.105	50%	10^{-6}	2.142	0.025	2.106	0.029
PT ₄	1	$1.337^{+0.006}_{-0.004}$	0.095	50%	$2 \cdot 10^{-4}$	2.000	0.032	1.936	0.020
	2	1.404	0.086	60%	10^{-5}	2.060	0.022	1.988	0.017
	3	1.430	0.085	60%	$1 \cdot 10^{-4}$	2.095	0.019	2.021	0.016
	4	1.441	0.086	50%	10^{-6}	2.117	0.018	2.047	0.016

D.3.2 1223-Series, Single-Element

PT	OP	ANSYS		Separation Onset	max. RMS	MSES/MSIS		XFOIL	
		C _L	C _D			C _L	C _D	C _L	C _D
PT ₁	1	2.135	0.119	65%	$5 \cdot 10^{-6}$	1.866	0.019	1.722	0.013
	2	2.217	0.111	70%	10^{-6}	1.808	0.016	1.762	0.012
	3	2.245	0.107	60%	10^{-6}	1.800	0.015	1.791	0.011
	4	2.271	0.105	60%	$3 \cdot 10^{-6}$	1.810	0.015	1.813	0.010
PT ₂	1	1.932	0.165	60%	10^{-6}	2.063	0.035	1.971	0.022
	2	$1.991^{+0.020}_{-0.027}$	0.160	70%	$2 \cdot 10^{-4}$	2.039	0.030	2.026	0.019
	3	$1.852^{+0.000}_{-0.002}$	0.189	60%	$5 \cdot 10^{-5}$	2.008	0.032	2.060	0.018
	4	$1.939^{+0.060}_{-0.026}$	0.164	60%	$2 \cdot 10^{-4}$	2.013	0.032	2.082	0.017
PT ₃	1	1.300	0.126	40%	$4 \cdot 10^{-5}$	2.132	0.041	2.063	0.049
	2	$1.385^{+0.007}_{-0.005}$	0.111	50%	$2 \cdot 10^{-4}$	2.100	0.032	2.071	0.049
	3	$1.411^{+0.000}_{-0.002}$	0.106	50%	$1 \cdot 10^{-5}$	2.136	0.028	2.057	0.051
	4	$1.426^{+0.001}_{-0.010}$	0.103	40%	$3 \cdot 10^{-4}$	2.188	0.025	2.043	0.055
PT ₄	1	1.103	0.124	30%	$3 \cdot 10^{-5}$	1.906	0.039	2.065	0.044
	2	1.176	0.108	30%	$3 \cdot 10^{-5}$	1.960	0.030	2.084	0.039
	3	$1.182^{+0.018}_{-0.001}$	0.110	50%	$3 \cdot 10^{-4}$	2.005	0.027	2.077	0.046
	4	$1.199^{+0.013}_{-0.004}$	0.106	30%	10^{-4}	2.036	0.026	2.066	0.048

D.3.3 15th-Series, Double-Element

PT	OP	ANSYS		Sep. 1 st El.	Onset 2 nd El.	max. RMS	MSES/MSIS	
		C _L	C _D				C _L	C _D
PT ₁	1	1.977 ^{+0.042} _{-0.093}	0.178	100%	0%	4 · 10 ⁻⁴	3.349	0.036
	2	2.294 ^{+0.068} _{-0.011}	0.119	100%	40%	10 ⁻⁶	3.206	0.043
	3	2.377 ^{+0.022} _{-0.128}	0.129	100%	50%	10 ⁻³	3.226	0.038
	4	2.339 ^{+0.052} _{-0.948}	0.108	100%	50%	4 · 10 ⁻⁴	3.251	0.036
PT ₂	1	2.258 ^{+0.031} _{-0.077}	0.109	100%	60%	10 ⁻³	3.018	0.060
	2	2.299 ^{+0.007} _{-0.073}	0.104	100%	70%	10 ⁻³	3.126	0.040
	3	2.125 ^{+0.012} _{-0.053}	0.121	100%	70%	3 · 10 ⁻⁴	3.140	0.034
	4	2.334 ^{+0.012} _{-0.053}	0.098	100%	60%	1 · 10 ⁻³	3.127	0.022

D.3.4 1223-Series, Double-Element

PT	OP	ANSYS		Sep. 1 st El.	Onset 2 nd El.	max. RMS	MSES/MSIS	
		C _L	C _D				C _L	C _D
PT ₁	1	1.689 ^{+0.048} _{-0.020}	0.107	80%	50%	4 · 10 ⁻⁴	2.405	0.045
	2	1.719 ^{+0.031} _{-0.001}	0.105	80%	60%	4 · 10 ⁻⁴	2.495	0.029
	3	1.754 ^{+0.015} _{-0.045}	0.102	80%	60%	4 · 10 ⁻⁴	2.512	0.024
	4	1.797 ^{+0.032} _{-0.011}	0.093	90%	50%	3 · 10 ⁻⁴	2.518	0.023
PT ₂	1	2.679 ^{+0.000} _{-0.005}	0.111	100%	60%	2 · 10 ⁻⁴	3.209	0.081
	2	2.755	0.104	100%	60%	3 · 10 ⁻⁴	3.394	0.054
	3	2.749 ^{+0.002} _{-0.005}	0.102	100%	80%	3 · 10 ⁻⁴	3.427	0.044
	4	2.770 ^{+0.028} _{-0.002}	0.101	100%	80%	3 · 10 ⁻⁴	3.358	0.029

BIBLIOGRAPHY

- [1] M. L. Loyd, “Crosswind kite power,” *Journal of Energy*, vol. 4, no. 3, pp. 106–111, 1980. [Online]. Available: <http://arc.aiaa.org/doi/10.2514/3.48021>
- [2] F. Bauer, R. M. Kennel, C. M. Hackl, F. Campagnolo, C. L. Bottasso, M. Patt, and R. Schmehl, “Power Curve and Design Optimization of a Drag Power Kite,” in *Airborne Wind Energy Conference 2017 (AWEC 2017)*, Freiburg, 2017, pp. 1–84.
- [3] J. D. Anderson, *Fundamentals of Aerodynamics*, 3rd ed., M. Lange, Ed. New York: McGraw-Hill Higher Education, 2001.
- [4] B. R. Munson, D. F. Zoung, T. H. Okiishi, and W. W. Huebsch, *Fundamentals of Fluid Dynamics*, 6th ed. Don Fowley, 2009.
- [5] H. Schlichting and K. Gersten, *Boundary-Layer Theory*. Berlin, Heidelberg: Springer Berlin Heidelberg, 2017. [Online]. Available: <http://link.springer.com/10.1007/978-3-662-52919-5>
- [6] H. Schlichting and E. Truckenbrodt, *Aerodynamics of the Airplane*, L. Lackenbach and J. B. Gandy, Eds. McGraw-Hill International Book Company, 1979.
- [7] X. Yu and M. Gen, *Introduction to Evolutionary Algorithms*, ser. Decision Engineering. London: Springer London, 2010. [Online]. Available: <http://link.springer.com/10.1007/978-1-84996-129-5>
- [8] C. L. Bottasso, F. Campagnolo, F. Bauer, and M. Zhao, “CFD Investigation and Experimental Validation of a High-Lift Multi-Element Airfoil for a Drag Power Kite,” Ph.D. dissertation, Technical University of Munich, 2017.
- [9] Cambridge University Press, “Definition of “the Anthropocene” - English Dictionary,” 2018.
- [10] IPCC, “Climate Change 2014 Synthesis Report Summary Chapter for Policymakers,” *Ipcc*, p. 31, 2014.
- [11] Council of the EU, “International agreements on climate action,” 2018. [Online]. Available: <https://www.consilium.europa.eu/en/policies/climate-change/international-agreements-climate-action/>
- [12] European Environment Agency, “Policies and measures,” 2018. [Online]. Available: <https://www.eea.europa.eu/themes/climate/national-policies-and-measures>
- [13] Umwelt Bundesamt, “Indikator: Emission von Treibhausgasen,” 2018. [Online]. Available: <https://www.umweltbundesamt.de/indikator-emission-von-treibhausgasen{#}textpart-1>
- [14] —, “Erneuerbare Energien in Zahlen,” 2018. [Online]. Available: <https://www.umweltbundesamt.de/themen/klima-energie/erneuerbare-energien/erneuerbare-energien-in-zahlen>

- [15] ———, “Erneuerbare Energien,” 2018. [Online]. Available: <https://www.umweltbundesamt.de/themen/klima-energie/erneuerbare-energien/erneuerbare-energien-in-zahlen{#}statusquo>
- [16] H.-J. Wagner, M. Koch, J. Burkhardt, T. Böckmann, N. Feck, and P. Kruse, “CO₂-Emissionen der Stromerzeugung,” *Bwk*, vol. 59, no. 10, pp. 44–52, 2007.
- [17] R. Tryfonidou, *Energetische Analyse eines Offshore-Windparks unter Berücksichtigung der Netzintegration*. Fakultät für Maschinenbau der Ruhr-Universität Bochum, 2006.
- [18] L. Fagiano and M. Milanese, “Airborne Wind Energy: An overview,” in *2012 American Control Conference (ACC)*, vol. 22, no. 3. IEEE, jun 2012, pp. 3132–3143. [Online]. Available: <http://ieeexplore.ieee.org/xpls/abs{ }all.jsp?arnumber=6314801><http://ieeexplore.ieee.org/document/6555854><http://ieeexplore.ieee.org/document/6314801/>
- [19] U. Ahrens, M. Diehl, and R. Schmehl, “Airborne Wind Energy,” *Green Energy and Technology*, no. February, 2013.
- [20] F. Bauer, R. M. Kennel, C. M. Hackl, F. Campagnolo, M. Patt, and R. Schmehl, “Drag power kite with very high lift coefficient,” *Renewable Energy*, vol. 118, pp. 290–305, apr 2018. [Online]. Available: <https://doi.org/10.1016/j.renene.2017.10.073><http://linkinghub.elsevier.com/retrieve/pii/S0960148117310285>
- [21] F. Bauer, “Multidisciplinary Optimization of Drag Power Kites,” Unpublished Work, Technical University of Munich, 2018.
- [22] B. Pruenster, “Optimisation of a Multi-Element Airfoil for Kite Power Systems using MSES and CMA-ES,” Technical University of Munich, Tech. Rep., 2018.
- [23] ANSYS Inc., “Limitations to Student License?” 2018. [Online]. Available: <https://studentcommunity.ansys.com/thread/limitations-to-student-license/>
- [24] C. Grete, “The economic potential of kite power,” *Leonardo Times*, 2014.
- [25] F. Bauer and R. M. Kennel, “Fault Tolerant Power Electronic System for Drag Power Kites,” Technical University of Munich, Tech. Rep., 2018.
- [26] F. H. Page, “The handley page wing,” *Aeronaut Journal*, vol. 25, pp. 263—289, 1921.
- [27] J. Katz and A. Plotkin, *Low-Speed Aerodynamics*. Cambridge: Cambridge University Press, 2001, vol. 11, no. 3. [Online]. Available: <http://ebooks.cambridge.org/ref/id/CBO9780511810329>
- [28] H. Oertel, *Prandtl - Führer durch die Strömungslehre*, 2012. [Online]. Available: <http://link.springer.com/10.1007/978-3-8348-2315-1>
- [29] H. Schlichting and E. Truckenbrodt, *Aerodynamik des Flugzeuges II*. Berlin, Heidelberg: Springer Berlin Heidelberg, 2001, no. Teil II. [Online]. Available: <http://link.springer.com/10.1007/978-3-642-56910-4>
- [30] M. Hepperle, “Turbulators,” 2018. [Online]. Available: <https://www.mh-aerotools.de/airfoils/turbulat.htm>
- [31] A. M. O. Smith, “High-Lift Aerodynamics,” *Journal of Aircraft*, vol. 12, no. 6, pp. 501–530, jun 1975. [Online]. Available: <http://arc.aiaa.org/doi/10.2514/3.59830>
- [32] R. M. Hicks, E. M. Murman, and G. N. Vanderplaats, “An assessment of airfoil design by numerical optimization,” *Nasa-Tm-X_3092*, no. April, 1974.

- [33] J. Hruska, "Moore's Law is dead, long live Moore's Law," 2015. [Online]. Available: <https://www.extremetech.com/extreme/203490-moores-law-is-dead-long-live-moores-law>
- [34] P. Iannelli, F. Moens, M. Minervino, R. Ponza, and E. Benini, "Comparison of Optimization Strategies for High-Lift Design," *Journal of Aircraft*, vol. 54, no. 2, pp. 642–658, mar 2017. [Online]. Available: <https://arc.aiaa.org/doi/10.2514/1.C033648>
- [35] P. Iannelli and D. Quagliarella, "High-Lift System Optimization By Means of Genetic," *Baseline*, no. September, pp. 52–69, 2011.
- [36] R. Berry and M. D. Maughmer, "Multipoint inverse airfoil design method based on conformal mapping," *AIAA Journal*, vol. 14, no. 1, pp. 1–2, 1992.
- [37] K. Lane and D. Marshall, "Inverse Airfoil Design Utilizing CST Parameterization," in *48th AIAA Aerospace Sciences Meeting Including the New Horizons Forum and Aerospace Exposition*, no. January. Reston, Virginia: American Institute of Aeronautics and Astronautics, jan 2010. [Online]. Available: <http://arc.aiaa.org/doi/10.2514/6.2010-1228>
- [38] M. Drela, "Pros and Cons of Airfoil Optimization," in *Frontiers of Computational Fluid Dynamics*, D. A. Caughey and M. M. Hafez, Eds. World Scientific, 1998, pp. 1–19.
- [39] M. Drela and M. Giles, "ISES : A Two-Dimensional Viscous Aerodynamic Design and Analysis Code," *AIAA 25th Aerospace Sciences Meeting*, 1987.
- [40] S. Kim, J. J. Alonso, and A. Jameson, "Lift Configurations Using a Viscous Continuous Adjoint Method Design Optimization of High – Lift Configurations Using a Viscous Continuous Adjoint Method," in *40th AIAA*, 2002, pp. 1–20.
- [41] S. Chen, F. Zhang, and M. Khalid, "Aerodynamic Optimization for a High-Lift Airfoil/wing Configuration," in *22nd Applied Aerodynamics Conference and Exhibit*, no. August. Reston, Virginia: American Institute of Aeronautics and Astronautics, aug 2004, pp. 1–8. [Online]. Available: <http://arc.aiaa.org/doi/10.2514/6.2004-5078>
- [42] J. Wild, J. Brezillon, O. Amoignon, F. Moens, D. Quagliarella, and C. Aerodynamicist, "Advanced High-Lift Design by Numerical Methods and Wind Tunnel Verification within the European Project EUROLIFT II," *Aiaa*, no. June, pp. 1–18, 2007.
- [43] C. L. Rumsey and S. X. Ying, "Prediction of high lift: review of present CFD capability," *Progress in Aerospace Sciences*, vol. 38, no. 2, pp. 145–180, feb 2002. [Online]. Available: <http://linkinghub.elsevier.com/retrieve/pii/S0376042102000039>
- [44] M. MURAYAMA, Z. LEI, J. MUKAI, and K. YAMAMOTO, "CFD Validation for High-Lift Devices: Three-Element Airfoil," *TRANSACTIONS OF THE JAPAN SOCIETY FOR AERONAUTICAL AND SPACE SCIENCES*, vol. 49, no. 163, pp. 40–48, 2006. [Online]. Available: <http://joi.jlc.jst.go.jp/JST.JSTAGE/tjsass/49.40?from=CrossRef>
- [45] E. Benini, R. Ponza, and A. Massaro, "High-Lift Multi-Element Airfoil Shape and Setting Optimization Using Multi-Objective Evolutionary Algorithms," *Journal of Aircraft*, vol. 48, no. 2, pp. 683–696, mar 2011. [Online]. Available: <http://arc.aiaa.org/doi/10.2514/1.C031233>
- [46] L. Fagianò, A. U. Zraggen, M. Morari, and M. Khammash, "Automatic crosswind flight of tethered wings for airborne wind energy: Modeling, control design, and experimental results," *IEEE Transactions on Control Systems Technology*, vol. 22, no. 4, pp. 1433–1447, 2014.

- [47] M. Canale, L. Fagiano, M. Ippolito, and M. Milanese, "Control of tethered airfoils for a new class of wind energy generator," *Proceedings of the 45th IEEE Conference on Decision and Control*, pp. 4020–4026, 2006. [Online]. Available: <http://ieeexplore.ieee.org/document/4177614/>
- [48] P. Williams, B. Lansdorp, and W. Ockesl, "Optimal Crosswind Towing and Power Generation with Tethered Kites," *Journal of Guidance, Control, and Dynamics*, vol. 31, no. 1, pp. 81–93, jan 2008. [Online]. Available: <http://arc.aiaa.org/doi/10.2514/1.30089>
- [49] M. Erhard and H. Strauch, "Flight control of tethered kites in autonomous pumping cycles for airborne wind energy," *Control Engineering Practice*, vol. 40, pp. 13–26, jul 2015. [Online]. Available: <http://linkinghub.elsevier.com/retrieve/pii/S0967066115000490>
- [50] M. Erhard, G. Horn, and M. Diehl, "A quaternion-based model for optimal control of an airborne wind energy system," *ZAMM - Journal of Applied Mathematics and Mechanics / Zeitschrift für Angewandte Mathematik und Mechanik*, vol. 97, no. 1, pp. 7–24, jan 2017. [Online]. Available: <http://doi.wiley.com/10.1002/zamm.201500180>
- [51] M. Zanon, S. Gros, J. Andersson, and M. Diehl, "Airborne Wind Energy Based on Dual Airfoils," *IEEE Transactions on Control Systems Technology*, vol. 21, no. 4, pp. 1215–1222, 2013. [Online]. Available: <http://ieeexplore.ieee.org/xpl/articleDetails.jsp?arnumber=6514616>
- [52] J. W. Kolar, T. Friedli, F. Krismer, A. Looser, M. Schweizer, R. A. Friedemann, P. K. Steimer, and J. B. Bevirt, "Conceptualization and Multiobjective Optimization of the Electric System of an Airborne Wind Turbine," *IEEE Journal of Emerging and Selected Topics in Power Electronics*, vol. 1, no. 2, pp. 73–103, 2013. [Online]. Available: <http://ieeexplore.ieee.org/ielx7/6245517/6572818/06542652.pdf?tp=&arnumber=6542652&isnumber=6572818>
- [53] R. A. Friedemann, F. Krismer, and J. W. Kolar, "Design of a minimum weight dual active bridge converter for an Airborne Wind Turbine system," in *2012 Twenty-Seventh Annual IEEE Applied Power Electronics Conference and Exposition (APEC)*. IEEE, feb 2012, pp. 509–516. [Online]. Available: <http://ieeexplore.ieee.org/document/6165868/>
- [54] D. V. Lind, "Kite configuration and flight strategy for flight in high wind speeds," 2010. [Online]. Available: <https://patents.google.com/patent/US8922046B2/en>
- [55] —, "Airfoil for a flying wind turbine," 2013. [Online]. Available: <https://patents.google.com/patent/US9709026B2/en?q=+9%2C709%2C026>
- [56] B. W. Pomeroy, G. A. Williamson, and M. S. Selig, "Experimental Study of a Multielement Airfoil for Large Wind Turbines," *30th AIAA Applied Aerodynamics Conference*, no. June, pp. 1–14, 2012.
- [57] Aerocheck, "Die relative Luftfeuchtigkeit in Deutschland (mit Tabelle)," 2018. [Online]. Available: <http://aero-check.de/luftfeuchtigkeit/deutschland/>
- [58] Airfoil Tools, "S1223 (s1223-il)," 2018. [Online]. Available: <http://airfoiltools.com/airfoil/details?airfoil=s1223-il>
- [59] Yarpiz, "CMA-ES in MATLAB," 2015. [Online]. Available: <https://de.mathworks.com/matlabcentral/fileexchange/52898-cma-es-in-matlab>
- [60] M. Drela, "A User 's Guide to MSES 3 . 05," no. July, 2007.
- [61] —, "A User's Guide to MSES 3.05," 2007.

-
- [62] MathWorks, “digits,” 2018. [Online]. Available: <https://www.mathworks.com/help/symbolic/digits.html>
- [63] P. T. Tsilingiris, “Thermophysical and transport properties of humid air at temperature range between 0 and 100 degree Celsius,” *Energy Conversion and Management*, vol. 49, no. 5, pp. 1098–1110, 2008.
- [64] R. B. Montgomery, “Viscosity and Thermal Conductivity of Air and Diffusivity of Water Vaport in Air,” Woods Hole Oceanographic Institution, Tech. Rep., 1947.
- [65] SAS IP, “Two Equation Turbulence Models.” [Online]. Available: <https://www.sharcnet.ca/Software/Ansys/16.2.3/en-us/help/cfx{ }thry/i1302321.html{#}i1302479>
- [66] —, “The k-omega and SST Models.” [Online]. Available: <https://www.sharcnet.ca/Software/Ansys/16.2.3/en-us/help/cfx{ }mod/i1345900.html>
- [67] —, “Symmetry Plane.” [Online]. Available: <https://www.sharcnet.ca/Software/Ansys/16.2.3/en-us/help/cfx{ }thry/i1300716.html>
- [68] —, “Global Prism Settings.” [Online]. Available: <https://www.sharcnet.ca/Software/Ansys/17.0/en-us/help/icm{ }help/imesh{ }globalprism.html>
- [69] —, “Mesh Requirements.” [Online]. Available: <https://www.sharcnet.ca/Software/Ansys/16.2.3/en-us/help/flu{ }th/flu{ }th{ }sec{ }turb{ }sst{ }grid.html>
- [70] J. Morgado, R. Vizinho, M. A. Silvestre, and J. C. Páscoa, “XFOIL vs CFD performance predictions for high lift low Reynolds number airfoils,” *Aerospace Science and Technology*, vol. 52, pp. 207–214, 2016. [Online]. Available: <http://dx.doi.org/10.1016/j.ast.2016.02.031>
- [71] P. Chougule and S. R. Nielsen, “Simulation of flow over double-element airfoil and wind tunnel test for use in vertical axis wind turbine,” *Journal of Physics: Conference Series*, vol. 524, no. 1, 2014.
- [72] F. R. Menter, M. Kuntz, and R. Langtry, “Ten Years of Industrial Experience with the SST Turbulence Model,” *Turbulence, Heat and Mass Transfer*, vol. 4, 2003.
- [73] S. M. Aftab, A. S. Rafie, N. A. Razak, and K. A. Ahmad, “Turbulence model selection for low reynolds number flows,” *PLoS ONE*, vol. 11, no. 4, pp. 1–15, 2016.